Cellular imaging in regenerative medicine, cancer and osteoarthritis

Sandra T. van Tiel

Cellular Imaging in Regenerative Medicine, Cancer and Osteoarthritis

Sandra Theresia van Tiel

Cellular Imaging in Regenerative Medicine, Cancer and Osteoarthritis

Cellulaire beeldvorming in regeneratieve geneeskunde, kanker en artrose

Proefschrift

ter verkrijging van de graad van doctor aan de
Erasmus Universiteit Rotterdam
op gezag van de
rector magnificus

Prof.dr. R.C.M.E. Engels

en volgens besluit van het College voor Promoties.
De openbare verdediging zal plaatsvinden op

vrijdag 16 oktober 2020 om 9.30 uur

door

Sandra Theresia van Tiel
geboren te Rotterdam.

Erasmus University Rotterdam

Promotiecommissie:

Promotor: prof. dr. ir. M. Hendriks - De Jong

Overige leden: prof. dr. G.J.V.M. van Osch
                   dr. ir. A.G. Denkova
                   prof. dr. M. Smits

Copromotor: dr. M.R. Bernsen

Table of contents

1

INTRODUCTION

Introduction

Non-invasive imaging of cells *in vivo* plays a major role during diagnosis and therapy of various diseases. So, to understand the composition of a tissue or organ, or to visualize processes within a certain body area disease-related and labelled cells can be visualized. Such labels must first reach the cell, efficiently incorporate in the cell or attach to the cell and give a detectable signal (1) and next to that they should not affect the functionality of the cell (2). Cell labelling can be performed in a non-targeted manner; the label can be taken up in a cell, e.g. through endocytosis. Also targeted cell labelling is being applied; the label specifically binds a target, e.g. receptor or enzyme, on or in the cell. After labelling of the cells, they can be visualized using an imaging device. Depending on the imaging device the molecular, (patho)physiological and/ or anatomical changes of the cells/tissue/organ can be imaged using different methods:

- In case of the use of (super) paramagnetic labels magnetic resonance imaging (MRI) can be applied
- When the labels are radioactive, single photon emission computed tomography (SPECT) and positron emission tomography (PET) might be used
- With fluorescent/bioluminescent labels optical imaging (OI) is the technique of choice
- Bubbles filled with gas are used in ultrasound (US) imaging.

Within the focus of this thesis we will explain MRI, SPECT, CT and US technologies in more detail below. For detailed descriptions of these and other technologies the reader is referred to review papers (3, 4) and books (5-7) on this topic.

In this thesis we describe **cellular imaging in regenerative medicine** where damaged or aged tissue needs to be substituted with healthy cells to regain a proper function of the tissue. We also address **cancer cell imaging**, it is of importance to detect tumour cells to establish the location and spread of the tumour to decide on/or to investigate options for therapy, and to detect any changes in tumour growth. Finally, we also focused on imaging of specifically

activated macrophages during inflammatory disease in a mouse model for **osteoarthritis (OA)**. Different phenotypes of macrophages are present overtime during inflammatory disease processes such as in OA. Knowing which phenotype is present at a certain moment can help determining the stage of disease, but also give directions how to interfere in the disease development. So, for cellular imaging in regenerative medicine, cancer and inflammatory processes such as in osteoarthritis it is important to label the cells involved in the disease, so they can be non-invasively detected with an imaging device. This to be able to stage the disease and to be able to interfere in the disease development.

Imaging cells in regenerative medicine
Regenerative medicine deals with the restoration of damaged or ageing tissues. Stem cells have infinite cell division potential and can differentiate into other types of cells and have an important role in regenerative medicine research. Earlier, evaluations of the effectiveness of regenerative approaches were limited by the inability to monitor response to treatment over time, but nowadays we are able to incorporate a label into the cells by which the transplanted cells can be distinguished from their surrounding using imaging technologies (8-10). This way it is possible to determine their fate as well as their functional capabilities and the biological role they fulfill (11). We searched for the best iron labelling protocol for cells *in vitro* and *in vivo*, and we tried to quantify the iron labelled cells.

Cancer cell imaging for diagnosis and therapy
In preclinical tumour imaging studies nuclear imaging markers can be applied and are widely being used (12). Glucose metabolism is a key cellular function in cells, which is high in tumour cells, and can be imaged with a radioactive glucose derivative: ^{18}F[F]-FDG (13, 14). Receptors on or in tumour cells can be imaged with the use of e.g. peptide receptor radionuclide imaging. In the paragraph on targeted radiolabelled peptides, their structure and receptor-mediated uptake mechanisms are described.

For the last 20 years peptide receptor radionuclide therapy (PRRT) has been used to treat patients suffering from neuroendocrine tumours (NETs). These NETs are rare cancers, they are often already metastasized at time of diagnosis

(15) and typically express high levels of somatostatin receptor subtype 2 (SST2). This makes the somatostatin receptor an excellent target for diagnosis and treatment of the disease using high affinity radiolabelled peptide ligands with high affinity for the SST2. In the course of time different modifications to the original radiolabelled peptide have been made. For diagnosis and staging of the NETs [^{68}Ga]Ga-DOTA-Tyr[3]-octreotate PET imaging is very often applied (16). With the same peptide sequence, it is also possible to treat the tumour cells, but instead of the radionuclide Gallium-68 a therapeutic radionuclide, such as Lutetium-177, will be applied. This represents a good example of a so-called theragnostic peptide. Upon receptor binding Lutetium-177 can eradicate tumour cells via beta decay. At Erasmus MC, NETS are being treated with [^{177}Lu]Lu-DOTA-Tyr[3]-octreotate (17, 18). This treatment has a positive effect on life expectancy and improves quality of life (19). There is ongoing research conducted to even further improve this treatment by, for example, use of alpha-emitting radionuclides (20). Alpha emitters are increasingly applied because of their emission of high linear energy transfer particles with a relative short path length, causing double-strand breaks in DNA. Therefore, the cytotoxic property in cells is much greater for α-emitters than for β-emitters (21). Other improvements of PRRT can be achieved by combination therapies with e.g. chemotherapeutics to reach a synergistic effect or by adjustment of radiopeptide administration routes to be able to enhance uptake of radiopeptides in the tumour cells (22-24). The blood clearance of [^{177}Lu]Lu-DOTA-Tyr[3]-octreotate in humans is rapid (<10%ID in blood at 3 h post injection) (25) and may be decreased by using a radiopeptide combined with an albumin binding strategy. In this way the tracer circulation time will be prolonged, resulting in higher tumour uptake.

NETs express the SST2 receptor, but many other receptors can be used for imaging, staging and treatment of other types of cancers. In this thesis we also investigated the gastrin-releasing peptide receptor (GRPR) as target. GRPRs are e.g. expressed at high density on the cell membranes of prostatic intraepithelial neoplasia (PIN), primary prostate cancers and invasive prostatic carcinomas (26). For diagnosis, the GRPR antagonist Sarabesin 3 (SB3) has recently been developed (27). Pre-clinically, in mice, a high tumour receptor affinity was found together with good *in vivo* stability and excellent targeting efficacy. In clinical PET imaging studies [^{68}Ga]Ga-SB3 was used with success as

well. The first clinical data showed encouraging results: in fifty percent of the patients the lesions were visualized (28, 29). During surgical excision of such tumours the surgeon may prefer to visualise the tumour pre-operatively with SPECT and also detect the tumour intra-operatively (30). This can be achieved when a radionuclide is coupled to the tracer which emits gamma photons, like Indium-111 (31). Here we investigated the potential of $[^{111}In]In$-SB3 as a radiotracer for pre-operative SPECT/MRI and sub sequentially improved tumour targeting.

Macrophage imaging

Macrophages are abundantly present immune cells characterized by phagocytic activity. When macrophages become activated, upon receiving signals from their microenvironment, they secrete cytokines that influence matrix remodelling and other cells in close proximity. Macrophages are then polarized towards different phenotypes (M1=pro-inflammatory, M2=anti-inflammatory) expressing a characteristic repertoire of surface markers. M1 macrophages constitute the first line of defence against intracellular pathogens and occur in an inflammatory environment. They are able to produce pro-inflammatory cytokines (e.g. TNF-α, type I IFN) and several chemokines. M2 macrophages are particularly involved during parasitic, helminthic and fungal infections. They down regulate pro-inflammatory cytokines and induce production of anti-inflammatory mediators (32, 33). The original polarization can be reversed upon environmental changes (34).

To emphasise the importance of *in vivo* macrophage visualisation, one should realize that macrophages play a role in many diseases. Activated macrophages are e.g. found in the brain of patients with schizophrenia (35, 36) and pulmonary macrophages are associated with tissue fibrosis (37). In the vasculature macrophages contribute to the formation of atherosclerotic plaques (38, 39). Macrophages also play a role in inflammatory diseases such as inflammatory bowel disease (40) and rheumatoid arthritis (41). Depending on the type of activation, macrophages can facilitate or prevent disease. So, knowing which kind of macrophage is present during the development of a disease is important for interference in disease development. In collaboration with the Orthopaedics Department we focused on macrophage involvement in the development of osteoarthritis (OA). OA affects many persons worldwide

leading to major societal impact (42). The presence of inflammation in the joint is a cause or an exacerbating factor for OA, for which there is no effective treatment currently. The focus is now primarily on pain reduction, so knowledge on how to delay or stop inflammatory damage may be crucial for the development of more curative treatment strategies. A possible treatment could be the modulation of the functional state of the inflammatory cells. The aims of our study described in this thesis were 1) to determine how macrophage phenotypes and monocyte subsets vary with time after destabilization of the medial meniscus; 2) to investigate associations between monocyte subsets or macrophage phenotypes and OA features 3) *in vivo* macrophage visualisation during the course of OA (43).

Labels for cell imaging

There are many types of imaging labels with different size, shape, composition and functionality (44), including liposomes, polymers, dextran coated particles, antibodies and peptides. When injected in the bloodstream these carriers travel throughout the body and can end up in extravascular spaces, followed by binding to and/or uptake in the targeted cells. The fact that carriers can bind and or be taken up by cells has enabled new ways of imaging of organs, tumours and other tissues in the body (45, 46).

Non targeted iron oxide particles

The most commonly applied and easiest way to achieve spontaneous uptake of an imaging particle is by exposing the cells to the labelling agent in culture. This may require additional use of a transfection agent (47). The cells then actively incorporate the particles through endocytotic pathways; the particles generally end up in endosomal compartments (Fig. 1). The now cell-associated labelling agent serves as the signaling beacon by which transplanted cells can be identified in imaging studies (48-51).

Particulate label types used in this thesis are two types of iron oxide particles: super paramagnetic iron oxide particles (SPIO) and micro particles of iron oxide (MPIO) which provide high detection sensitivity. SPIO particles have a particle diameter between 80 and 150nm, consisting of an iron oxide core of 4 nm with a low-molecular-weight dextran coating (52-54). MPIO particles are composed of polystyrene–divinyl benzene polymer micro spheres containing
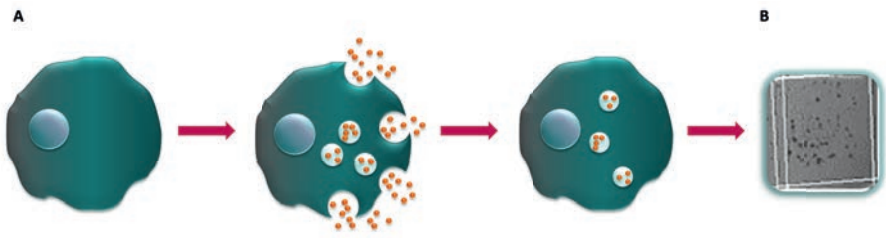
Figure 1 A Non targeted uptake of nanoparticles (brown dots) through endocytosis **B** MR image of single cells labelled *in vitro* with iron particles (black dots).

a magnetite core and are tagged with the fluorescent dye Dragon green (480/520 nm). The iron oxide crystals have a strong magnetic moment, causing a disturbance of the local magnetic field resulting in local signal loss in MR images. MPIO have an average size of 1630 nm and have been shown to be functionally inert and they create a larger and stronger effect in MRI than SPIO (55, 56). Both SPIO and MPIO are efficiently endocytosed by many cell types (Fig. 2) and are passed along to daughter cells during mitosis (57-59).

CD31 targeted microbubbles
In cell imaging there is always the challenge to get enough label in the cell for efficient imaging during a longer period of time. *In vitro* one can increase the dose of the label, but *in vivo* this is much more difficult to achieve. Therefore, targeting solutions are needed to achieve more efficient uptake.

In this thesis we used gas-filled microbubbles to target (CD31 (60)) cells. These microbubbles are between 1 and 10 micrometres in diameter and often coated with lipids. They are excellent ultrasound scatters due to their high compressibility. High-frequency sound waves make the gas in the microbubble vibrate as a response to the pressure change (61). The oscillation of microbubbles has been shown to increase cell membrane- and capillary permeability (62). We used this capability to introduce iron nanoparticles into the cell.

Targeted radiolabelled peptides
Cells express receptor proteins on their plasma membranes. Receptors can have high affinity for regulatory peptides allowing cellular communication with the outer environment. If certain receptors are overexpressed during disease, they can be used for imaging and therapy applications. The radioactive

peptides attach to the receptors upon which they can be internalised or stay at the cell surface (Fig. 3) (63, 64). Radiolabelled peptides hold great promise for imaging and treatment of cancer cells, but also for imaging of other cells, e.g. macrophages.
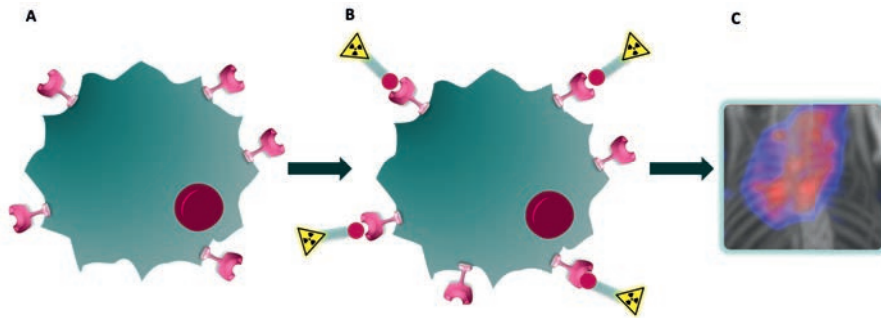

Figure 2 Schematic drawing of receptor-mediated uptake of a radiolabelled peptide A Cell with receptors on cell surface **B** Radioactive tracer attached to receptor **C** Representative SPECT image of the chest of a mouse showing radioactive tumour cells (in red) after receptor-specific radiolabelled peptide injection.

Radiolabelled peptides, also called tracers, can be used in diagnostic imaging of (tumour) cells or can be used in radionuclide therapy of tumours. This all depends on the radionuclide attached to the peptide. A radiolabelled peptide consists of different components. One component is the peptide; this peptide is the part that binds to the receptor present in or on the surface of the cell. Another possible component is attached to the peptide and called a linker; this creates space between the chelator and the binding site to prevent loss of binding affinity. On the other site of the linker a third component can be coupled; a chelator containing the radionuclide (Fig. 4) (65).
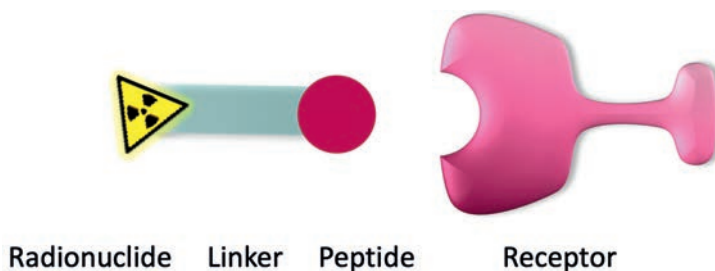

Figure 3 General representation of a radiolabelled peptide consisting of a radionuclide in a chelator, a linker and a peptide, which recognises the receptor on the cell.

Radionuclides

A radionuclide is a radioactive form of an element. Some of them exist in nature, while others are man-made. Radioactivity can be used for many different purposes, i.e. to study living organisms, to diagnose and treat diseases, to produce energy for heat and electric power and it can be used to sterilize medical instruments and food, etc. Half-life is the time required for half of the radioactive atoms present to decay. The radiation that is emitted by a radionuclide does this at its own specific rate (https://www.epa.gov/radiation/radionucliceswww.epa.gov/radiation/radionuclides). The half-life can range from milliseconds to millions of years, but clinically a half-life between 20 minutes and 10 days is most often used.

Two radionuclides have been applied in this thesis work. The first one is Indium-111, which is being applied for diagnostic imaging. It decays with a half-life of 67,9 h, emitting gamma-rays of 171 and 245 keV. Lutetium-177 is the second one and is being used for radiotherapeutic applications; it decays with a half-life of 161 h, emitting β– particles with a maximum energy of 498 keV. Also, low energy γ-rays of 113 and 210 keV are emitted, making this radionuclide suitable for theragnostic applications. Other radionuclides applied in nuclear medicine are presented in Table 1 (66) (https://www.nndc.bnl.gov/nudat2).

Table 1 Specifics and applications of some radionuclides frequently used in nuclear medicine.

Radionuclide	Half-life (h)	Type of decay (%)	Production mode	Used for
Bismuth-213	0,76	α (2), β– (98)	$^{225}Ac/^{213}Bi$ generator	Therapy
Copper-64	12,7	β+ (19), β– (40), Ɛ (41)	Cyclotron	PET imaging
Copper-67	61,9	β– (100), γ	Accelerator	Therapy
Fluor-18	1,83	β+ (97), Ɛ (3)	Cyclotron	PET imaging
Gallium-68	1,13	β+ (89), Ɛ (11)	$^{68}Ge/^{68}Ga$ generator	PET imaging
Indium-111	67,9	Ɛ (100), Auger,γ	Cyclotron	SPECT imaging
Lutetium-177	161	β– (100), γ	Reactor	Therapy + SPECT imaging
Technetium-99m	6,02	IT (99.99), γ (0,01)	$^{99}Mo/^{99m}Tc$ generator	SPECT imaging
Yttrium-90	64,1	β– (100)	$^{90}Sr/^{90}Y$ generator	Therapy
Zirkonium-89	78,4	Ɛ (77), β+ (23)	Cyclotron	PET Imaging

Ɛ = electron capture, IT= isomeric transition

Imaging modalities

The various medical *in vivo* imaging techniques each have their own advantages and disadvantages regarding their use in cellular imaging. Optical imaging techniques have been widely used in pre-clinical studies. The limited tissue penetration capability of light, however, to a large extent limits the use of these techniques to small laboratory animals (67). Studies aimed at clinical translatability, have therefore largely focused on US, MRI, PET or SPECT, where the latter three are not limited by signal penetration depths in tissue (68, 69). An overview of different imaging modalities used in preclinical research was recently given by de Jong et.al. (70), the modalities used in this thesis are explained below.

MRI

Magnetic resonance imaging (MRI) offers several advantages for *in vivo* cell tracking. Through the use of a strong homogenous magnetic field, gradients and radio waves, an image is generated. MRI has high temporal and spatial resolution, excellent tissue contrast and tissue penetration, does not apply ionizing radiation, is non-invasive for serial studies, and simultaneous acquisition of anatomical structure and physiological function can be obtained (71). In this high magnetic field, hydrogen atoms can be manipulated. Our body contains up to 70% of water, which provides an abundant amount of hydrogen atoms. The spin of hydrogen atoms is affected by the radiofrequency (RF) pulse. When the RF pulse is turned off, the hydrogen atoms can return to the original state. This entire process is known as "relaxation." After positional measurement of the relaxation by receiver coils, the relaxations can be transformed into a MRI image (72). Contrast agents can enhance the relaxation rates (73). Longitudinal and transverse relaxation time (resp. T1 and T2) is being used to characterize different tissues. T1 is the time constant which determines the rate at which excited hydrogen atoms return to equilibrium. T2 is the time constant which measures the time taken for spinning hydrogen atoms to lose phase coherence among the nuclei spinning perpendicular to the main field.

US

Ultrasound imaging, like MRI and CT, is used for diagnostic imaging, but also as a therapeutic tool. Sound frequencies of 1 MHz and higher are used and are also referred to as ultrasound. The human body consists of different structures,

which all scatter and reflect high-frequency sound waves differently resulting in intensity differences in an ultrasound image. Compared to MRI, SPECT, PET and CT imaging ultrasound imaging has some advantages such as price, convenience, and fast real-time imaging, but it has poor penetration through bone or air (74, 75). The sound waves can also be used for site-specific cell labelling. This can be achieved with the use of ultrasound contrast agents like microbubbles. The microbubbles change their size under influence of the generated waves. The vibration of the microbubbles that arises can change the structure of cell membrane and enhance its permeation. Through sonoporation reversible or non-reversible cell membrane pores are generated upon microbubble oscillations (76, 77).

SPECT

Single-photon emission computed tomography (SPECT) is a nuclear imaging technique just like positron emission tomography (PET). SPECT is widely used in (pre)clinical studies and is an advanced radionuclide molecular imaging technique that is able to evaluate biochemical changes and levels of molecular targets *in vivo* (78). It enables whole body imaging of molecular targets/processes with high sensitivity. Since biochemical changes often occur before anatomical changes in disease, SPECT has clear diagnostic strength (79). However SPECT has a key weakness, which is, showing poor anatomical information. This weakness may be eliminated through the combination of instruments with either CT or MRI, producing a single scanner capable of accurately identifying molecular events with precise correlation to anatomical findings (80, 81).

SPECT can measure the biodistribution of extremely small ($<10^{-10}$ molar) concentrations of radiolabelled biomolecules/nanoparticles *in vivo* with, when using a pre-clinical system, sub-millimetre resolution and quantify the molecular kinetic processes in which they participate. Its capabilities include:

(i)   the ability to image radiolabelled biomolecules/nanoparticles

(ii)   compared to PET, SPECT has the ability to measure relatively slow kinetic processes due to the relatively long half-life of the commonly used radionuclides

(iii)   the ability to probe two or more molecular pathways simultaneously by detecting radionuclides with different emission energies (82).

In SPECT, collimator design is always a compromise between spatial resolution and sensitivity. Parallel hole collimators can be used in clinical SPECT imaging and in the preclinical setting (multi)pinhole collimators are used. Preclinical multi pinhole collimators are used to obtain a much better spatial resolution compared to conventional parallel-hole collimator (83). In comparison to a parallel-hole collimator, pinhole collimators provide a smaller field of view (FOV). These collimators are suited to image focal uptake or organs in the body or the whole body, because they generate magnified images. So, smaller pinhole diameter leads to an improvement the spatial resolution, but also a loss in sensitivity (84-86). A drawback of SPECT use is that the subject is exposed to radioactivity.

CT

In computed tomography (CT) images are obtained thanks to different levels of X-ray attenuation by tissues within the body (87). Pre-clinical devices are very fast and offer ultra-high-resolution scanning at low x-ray doses. A detector rotates around the animal or patient, acquiring volumetric data (88). When associated with other imaging modalities, CT can give an anatomical reference frame for the biochemical and physiological findings that are provided by other imaging instruments. A CT is also of importance with quantification of SPECT/PET data as it is used for accurate scatter and attenuation correction (89). One of the drawbacks of the use of a CT is that it has little soft tissue in small animals, so there is a need for contrast agents. Next to that the subject is exposed to radiation.

Aim and thesis outline

This thesis describes several methods for imaging of cells in regenerative medicine, cancer and osteoarthritis. The overall aim of the studies was to label cells involved in disease, so they can be detected non-invasively with an imaging device as a means to stage the disease and to potentially interfere in the disease development. In **Chapter 1,** a general introduction to molecular imaging is given. We describe the imaging devices used in molecular imaging and cell labelling strategies that can be employed. In regenerative medicine the aim is to substitute damaged or aged tissue with healthy cells to regain a proper function of the tissue. To be able to visualize this process with MRI, cells can be labelled with iron particles. In **Chapter 2** the efficacy of iron particles

1

for cell labelling and MR imaging studies was investigated by studying the effect of variations in labelling protocols regarding incorporation, distribution and retention of iron oxide nanoparticles. By mimicking the effects of various distribution patterns through labelling of cells with small (SPIO) and larger (MPIO) iron particles we studied the effect of various inter- and intra-cellular distributions profiles on quantifiability of iron oxide-labelled cells, as described in **Chapter 3**. To label the cells with iron oxide particles different strategies can be followed. So, in Chapter 2 and 3 we added a transfection agent to enhance entrance of iron particles into the cells. The aim of our *in vitro* study described in **Chapter 4** was to find the optimal parameters for non-invasive, microbubble-mediated SPIO labelling of endothelial cells to eventually enable iron particle endothelial cell labelling in the body. In **Chapter 5** our research aimed to increase *in vivo* stability of an Indium-111 labelled radiopeptide targeting the gastrin-releasing peptide receptor (GRPR). In **Chapter 6** we investigated how to further improve the biodistribution of another peptide, targeting somatostatin receptor subtype 2, by prolonging the tracer circulation time upon adding an albumin-binding domain to the radiopeptide structure. In **Chapter 7** we investigated the value of the somatostatin receptor subtype 2 as a novel imaging marker for pro-inflammatory macrophages also using the DMM osteoarthritic mouse model.

References

1. Bernsen MR, Kooiman K, Segbers M, van Leeuwen FW, de Jong M. Biomarkers in preclinical cancer imaging. Eur J Nucl Med Mol Imaging. 2015;42(4):579-96.

2. Meng Q, Li Z. Molecular imaging probes for diagnosis and therapy evaluation of breast cancer. Int J Biomed Imaging. 2013;2013:230487.

3. Pysz MA, Gambhir SS, Willmann JK. Molecular imaging: current status and emerging strategies. Clinical Radiology. 2010;65(7):500-16.

4. Chen Z-Y, Wang Y-X, Lin Y, Zhang J-S, Yang F, Zhou Q-L, et al. Advance of Molecular Imaging Technology and Targeted Imaging Agent in Imaging and Therapy. 2014;2014:1-12.

5. Weissleder R. Molecular Imaging: Principles and Practice: People's Medical Publishing House; 2010.

6. Semmler W, Schwaiger M. Molecular Imaging I: Springer Berlin Heidelberg; 2008.

7. Semmler W, Schwaiger M. Molecular Imaging II: Springer Berlin Heidelberg; 2008.

8. Accomasso L, Gallina C, Turinetto V, Giachino C. Stem Cell Tracking with Nanoparticles for Regenerative Medicine Purposes: An Overview. Stem Cells International. 2016;2016:1-23.

9. Ruggiero A, Guenoun J, Smit H, Doeswijk GN, Klein S, Krestin GP, et al. In vivo MRI mapping of iron oxide-labeled stem cells transplanted in the heart. Contrast Media Mol Imaging. 2013;8(6):487-94.

10. Stacy MR, Sinusas AJ. Emerging Imaging Modalities in Regenerative Medicine. 2015;3(1):27-36.

11. Ruggiero A, Thorek DL, Guenoun J, Krestin GP, Bernsen MR. Cell tracking in cardiac repair: what to image and how to image. Eur Radiol. 2012;22(1):189-204.

12. Bernsen MR, Kooiman K, Segbers M, Van Leeuwen FWB, De Jong M. Biomarkers in preclinical cancer imaging. Eur J Nucl Med Mol I. 2015;42(4):579-96.

13. Buerkle A, Weber WA. Imaging of tumor glucose utilization with positron emission tomography. 2008;27(4):545-54.

14. Momcilovic M, Bailey ST, Lee JT, Zamilpa C, Jones A, Abdelhady G, et al. Utilizing 18F-FDG PET/CT Imaging and Quantitative Histology to Measure Dynamic Changes in the Glucose Metabolism in Mouse Models of Lung Cancer. J Vis Exp. 2018(137).

15. Korse CM, Taal BG, van Velthuysen ML, Visser O. Incidence and survival of neuroendocrine tumours in the Netherlands according to histological grade: experience of two decades of cancer registry. Eur J Cancer. 2013;49(8):1975-83.

16. Bodei L, Ambrosini V, Herrmann K, Modlin I. Current Concepts in68Ga-DOTATATE Imaging of Neuroendocrine Neoplasms: Interpretation, Biodistribution, Dosimetry, and Molecular Strategies. Journal of Nuclear Medicine. 2017;58(11):1718-26.

17. Zandee WT, Brabander T, Blazevic A, Kam BLR, Teunissen JJM, Feelders RA, et al. Symptomatic and radiological response to 177Lu-DOTATATE for the treatment of functioning pancreatic neuroendocrine tumors. J Clin Endocrinol Metab. 2018.

18. Van Der Zwan WA, Brabander T, Kam BLR, Teunissen JJM, Feelders RA, Hofland J, et al. Salvage peptide receptor radionuclide therapy with [177Lu-DOTA,Tyr3]octreotate in patients with bronchial and gastroenteropancreatic neuroendocrine tumours. Eur J Nucl Med Mol I. 2018.

19. van der Zwan WA, Bodei L, Mueller-Brand J, de Herder WW, Kvols LK, Kwekkeboom DJ. GEPNETs update: Radionuclide therapy in neuroendocrine tumors. Eur J Endocrinol. 2015;172(1):R1-8.

20. Chan HS, de Blois E, Morgenstern A, Bruchertseifer F, de Jong M, Breeman W, et al. In Vitro comparison of 213Bi- and 177Lu-radiation for peptide receptor radionuclide therapy. PLoS One. 2017;12(7):e0181473.

21. Chan HS, Konijnenberg MW, De Blois E, Koelewijn S, Baum RP, Morgenstern A, et al. Influence of tumour size on the efficacy of targeted alpha therapy with 213Bi-[DOTA0,Tyr3]-octreotate. 2016;6(1).

22. Bison SM, Konijnenberg MW, Melis M, Pool SE, Bernsen MR, Teunissen JJ, et al. Peptide receptor radionuclide therapy using radiolabeled somatostatin analogs: focus on future developments. Clin Transl Imaging. 2014;2:55-66.

23. Chatalic KL, Kwekkeboom DJ, de Jong M. Radiopeptides for Imaging and Therapy: A Radiant Future. J Nucl Med. 2015;56(12):1809-12.

24. Pool SE, Kam BL, Koning GA, Konijnenberg M, Ten Hagen TL, Breeman WA, et al. [(111)In-DTPA]oc-treotide tumor uptake in GEPNET liver metastases after intra-arterial administration: an overview of preclinical and clinical observations and implications for tumor radiation dose after peptide radionuclide therapy. Cancer Biother Radiopharm. 2014;29(4):179-87.

25. Esser JP, Krenning EP, Teunissen JJM, Kooij PPM, Van Gameren ALH, Bakker WH, et al. Comparison of [177Lu-DOTA0,Tyr3]octreotate and [177Lu-DOTA0,Tyr3]octreotide: which peptide is preferable for PRRT? 2006;33(11):1346-51.

26. Markwalder R, Reubi JC. Gastrin-releasing peptide receptors in the human prostate: relation to neoplastic transformation. Cancer Res. 1999;59(5):1152-9.

27. Maina T dJM, Charalambidis D, et al. [67/68Ga]Sarabesin 3: Preclinical evaluation in GRPR-expressing models - First successful clinical PET/CT imaging of prostate cancer metastases. j Nucl Med. 2013;54.

28. Maina T, Bergsma H, Kulkarni HR, Mueller D, Charalambidis D, Krenning EP, et al. Preclinical and first clinical experience with the gastrin-releasing peptide receptor-antagonist [68Ga]SB3 and PET/CT. 2015.

29. Bakker I FA, Busstra MB et al. PET imaging of prostate cancer using the GRPr-targeting ligand Sarabesin 3 prior to radical prostatectomy [abstract]. Eur J Nucl Med. 2016;43.

30. Bugby SL, Lees JE, Perkins AC. Hybrid intraoperative imaging techniques in radioguided surgery: present clinical applications and future outlook. Clin Transl Imaging. 2017;5(4):323-41.

31. Maina T, Bergsma H, Kulkarni HR, Mueller D, Charalambidis D, Krenning EP, et al. Preclinical and first clinical experience with the gastrin-releasing peptide receptor-antagonist [(6)(8)Ga]SB3 and PET/CT. Eur J Nucl Med Mol Imaging. 2016;43(5):964-73.

32. Martinez FO, Gordon S, Locati M, Mantovani A. Transcriptional Profiling of the Human Monocyte-to-Macrophage Differentiation and Polarization: New Molecules and Patterns of Gene Expression. The Journal of Immunology. 2006;177(10):7303-11.

33. Italiani P, Mazza EMC, Lucchesi D, Cifola I, Gemelli C, Grande A, et al. Transcriptomic Profiling of the Development of the Inflammatory Response in Human Monocytes In Vitro. 2014;9(2):e87680.

34. Xu W, Zhao X, Daha MR, Van Kooten C. Reversible differentiation of pro- and anti-inflammatory macrophages. 2013;53(3):179-86.

35. Drexhage RC, Knijff EM, Padmos RC, Heul-Nieuwenhuijzen LVD, Beumer W, Versnel MA, et al. The mononuclear phagocyte system and its cytokine inflammatory networks in schizophrenia and bipolar disorder. 2010;10(1):59-76.

36. Smith RS. A comprehensive macrophage-T-lymphocyte theory of schizophrenia. 1992;39(3):248-57.

37. Byrne AJ, Maher TM, Lloyd CM. Pulmonary Macrophages: A New Therapeutic Pathway in Fibrosing Lung Disease? Trends in Molecular Medicine. 2016;22(4):303-16.

38. Bobryshev YV, Ivanova EA, Chistiakov DA, Nikiforov NG, Orekhov AN. Macrophages and Their Role in Atherosclerosis: Pathophysiology and Transcriptome Analysis. 2016;2016:1-13.

39. Moore KJ, Sheedy FJ, Fisher EA. Macrophages in atherosclerosis: a dynamic balance. Nature Reviews Immunology. 2013;13(10):709-21.

40. Bain CC, Mowat AM. Macrophages in intestinal homeostasis and inflammation. Immunological Reviews. 2014;260(1):102-17.

41. Udalova IA, Mantovani A, Feldmann M. Macrophage heterogeneity in the context of rheumatoid arthritis. 2016;12(8):472-85.

42. O'Neill TW, McCabe PS, McBeth J. Update on the epidemiology, risk factors and disease outcomes of osteoarthritis. Best Practice & Research Clinical Rheumatology. 2018;32(2):312-26.

43. Blom AB, van Lent PL, Holthuysen AE, van der Kraan PM, Roth J, van Rooijen N, et al. Synovial lining macrophages mediate osteophyte formation during experimental osteoarthritis. Osteoarthritis Cartilage. 2004;12(8):627-35.

44. Khan I, Saeed K, Khan I. Nanoparticles: Properties, applications and toxicities. Arabian Journal of Chemistry. 2017.

45. Wang EC, Wang AZ. Nanoparticles and their applications in cell and molecular biology. Integr Biol (Camb). 2014;6(1):9-26.

46. Hernot S, Klibanov AL. Microbubbles in ultrasound-triggered drug and gene delivery. Advanced Drug Delivery Reviews. 2008;60(10):1153-66.

47. van Buul GM, Farrell E, Kops N, van Tiel ST, Bos PK, Weinans H, et al. Ferumoxides-protamine sulfate is more effective than ferucarbotran for cell labeling: implications for clinically applicable cell tracking using MRI. Contrast Media Mol Imaging. 2009;4(5):230-6.

48. Bernsen MR, Moelker AD, Wielopolski PA, van Tiel ST, Krestin GP. Labelling of mammalian cells for visualisation by MRI. European Radiology. 2010;20(2):255-74.

49. Farrell E, Wielopolski P, Pavljasevic P, van Tiel S, Jahr H, Verhaar J, et al. Effects of iron oxide incorporation for long term cell tracking on MSC differentiation in vitro and in vivo. Biochem Biophys Res Commun. 2008;369(4):1076-81.

50. Duinhouwer LE, van Rossum BJ, van Tiel ST, van der Werf RM, Doeswijk GN, Haeck JC, et al. Magnetic Resonance Detection of CD34+ Cells from Umbilical Cord Blood Using a 19F Label. PLoS One. 2015;10(9):e0138572.

51. van Buul GM, Kotek G, Wielopolski PA, Farrell E, Bos PK, Weinans H, et al. Clinically translatable cell tracking and quantification by MRI in cartilage repair using superparamagnetic iron oxides. PLoS One. 2011;6(2):e17001.

52. Arbab AS, Yocum GT, Kalish H, Jordan EK, Anderson SA, Khakoo AY, et al. Efficient magnetic cell labeling with protamine sulfate complexed to ferumoxides for cellular MRI. Blood. 2004;104(4):1217-23.

53. Neri M, Maderna C, Cavazzin C, Deidda-Vigoriti V, Politi LS, Scotti G, et al. Efficient in vitro labeling of human neural precursor cells with superparamagnetic iron oxide particles: Relevance for in vivo cell tracking. Stem Cells. 2008;26(2):505-16.

54. Zhang Z, van den Bos EJ, Wielopolski PA, de Jong-Popijus M, Bernsen MR, Duncker DJ, et al. In vitro imaging of single living human umbilical vein endothelial cells with a clinical 3.0-T MRI scanner. Magn Reson Mater Phy. 2005;18(4):175-85.

55. Rodriguez O, Fricke S, Chien C, Dettin L, VanMeter J, Shapiro E, et al. Contrast-enhanced in vivo imaging of breast and prostate cancer cells by MRI. Cell Cycle. 2006;5(1):113-9.

56. Shapiro EM, Sharer K, Skrtic S, Koretsky AP. In vivo detection of single cells by MRI. Magnetic Resonance in Medicine. 2006;55(2):242-9.

57. Slotkin JR, Cahill KS, Tharin SA, Shapiro EM. Cellular magnetic resonance imaging: nanometer and micrometer size particles for noninvasive cell localization. Neurotherapeutics. 2007;4(3):428-33.

58. Zhang Z, van den Bos EJ, Wielopolski PA, de Jong-Popijus M, Bernsen MR, Duncker DJ, et al. In vitro imaging of single living human umbilical vein endothelial cells with a clinical 3.0-T MRI scanner. MAGMA. 2005;18(4):175-85.

59. Farrell E, Wielopolski P, Pavljasevic P, Kops N, Weinans H, Bernsen MR, et al. Cell labelling with superparamagnetic iron oxide has no effect on chondrocyte behaviour. Osteoarthritis Cartilage. 2009;17(7):961-7.

60. Skachkov I, Luan Y, van der Steen AF, de Jong N, Kooiman K. Targeted microbubble mediated sonoporation of endothelial cells in vivo. IEEE Trans Ultrason Ferroelectr Freq Control. 2014;61(10):1661-7.

61. De Jong N, Emmer M, Van Wamel A, Versluis M. Ultrasonic characterization of ultrasound contrast agents. 2009;47(8):861-73.

62. Prentice P, Cuschieri A, Dholakia K, Prausnitz M, Campbell P. Membrane disruption by optically controlled microbubble cavitation. Nature Physics. 2005;1(2):107-10.

63. de Jong M, Kwekkeboom D, Valkema R, Krenning EP. Radiolabelled peptides for tumour therapy: current status and future directions. Plenary lecture at the EANM 2002. Eur J Nucl Med Mol Imaging. 2003;30(3):463-9.

64. Krenning EP, Kwekkeboom DJ, Valkema R, Pauwels S, Kvols LK, De Jong M. Peptide receptor radionuclide therapy. Ann N Y Acad Sci. 2004;1014:234-45.

65. De Leon-Rodriguez LM, Kovacs Z. The synthesis and chelation chemistry of DOTA-peptide conjugates. Bioconjug Chem. 2008;19(2):391-402.

66. Fani M, Maecke HR. Radiopharmaceutical development of radiolabelled peptides. Eur J Nucl Med Mol Imaging. 2012;39 Suppl 1:S11-30.

67. Sutton EJ, Henning TD, Pichler BJ, Bremer C, Daldrup-Link HE. Cell tracking with optical imaging. European Radiology. 2008;18(10):2021-32.

68. Srivastava AK, Bulte JWM. Seeing Stem Cells at Work In Vivo. Stem Cell Rev Rep. 2014;10(1):127-44.

69. Aarntzen EHJG, Srinivas M, Radu CG, Punt CJA, Boerman OC, Figdor CG, et al. In vivo imaging of therapy-induced anti-cancer immune responses in humans. Cell Mol Life Sci. 2013;70(13):2237-57.

70. de Jong M, Essers J, van Weerden WM. Imaging preclinical tumour models: improving translational power. Nat Rev Cancer. 2014;14(7):481-93.

71. Bernsen MR, Moelker AD, Wielopolski PA, van Tiel ST, Krestin GP. Labelling of mammalian cells for visualisation by MRI. Eur Radiol. 2010;20(2):255-74.

72. Berger A. Magnetic resonance imaging. BMJ. 2002;324(7328):35.

73. Modo M. Molecular and Cellular MR imaging2007.

74. Fenster A, Downey DB. T HREE -D IMENSIONAL U LTRASOUND I MAGING. 2000;2(1):457-75.

75. Wells PN. Ultrasound imaging. Phys Med Biol. 2006;51(13):R83-98.

76. Lentacker I, De Cock I, Deckers R, De Smedt SC, Moonen CT. Understanding ultrasound induced sonoporation: definitions and underlying mechanisms. Adv Drug Deliv Rev. 2014;72:49-64.

77. Kooiman K, Vos HJ, Versluis M, de Jong N. Acoustic behavior of microbubbles and implications for drug delivery. Adv Drug Deliv Rev. 2014;72:28-48.

78. Wirrwar A, Schramm N, Vosberg H, Muller-Gartner HW. High resolution SPECT in small animal research. Rev Neurosci. 2001;12(2):187-93.

79. Wu M, Shu J. Multimodal Molecular Imaging: Current Status and Future Directions. Contrast Media & Molecular Imaging. 2018;2018:1-12.

80. Bernsen MR, Ruggiero A, Van Straten M, Kotek G, Haeck JC, Wielopolski PA, et al. Computed Tomography and Magnetic Resonance Imaging. Springer Berlin Heidelberg; 2013. p. 3-63.

81. Bernsen MR, Vaissier PEB, Van Holen R, Booij J, Beekman FJ, De Jong M. The role of preclinical SPECT in oncological and neurological research in combination with either CT or MRI. 2014;41(S1):36-49.

82. Meikle SR, Kench P, Kassiou M, Banati RB. Small animal SPECT and its place in the matrix of molecular imaging technologies. Phys Med Biol. 2005;50(22):R45-61.

83. Beekman F, Van Der Have F. The pinhole: gateway to ultra-high-resolution three-dimensional radionuclide imaging. 2007;34(2):151-61.

84. Kupinski MA. Small-animal SPECT imaging.

85. Single Photon Emission Computed Tomography. Mathematics and physics of emerging biomedical imaging: National Academies Press (US); 1996. p. 89-104.

86. Islamian JP, Azazrm A, Mahmoudian B, Gharapapagh E. Advances in pinhole and multi-pinhole collimators for single photon emission computed tomography imaging. World J Nucl Med. 2015;14(1):3-9.

87. Dendy PP HB. Physics for diagnostic radiology2011.

88. Massoud TF, Gambhir SS. Molecular imaging in living subjects: seeing fundamental biological processes in a new light. Genes Dev. 2003;17(5):545-80.

89. James ML, Gambhir SS. A molecular imaging primer: modalities, imaging agents, and applications. Physiol Rev. 2012;92(2):897-965.

2

Variations in labeling protocol influence incorporation, distribution and retention of iron oxide nanoparticles into human umbilical vein endothelial cells

Sandra T. van Tiel[a], Piotr A. Wielopolski[a], Gavin C. Houston[b], Gabriel P. Krestin[a] and Monique R. Bernsen[a]

[a] S. T. van Tiel, P. A. Wielopolski, G. P. Krestin, M. R. Bernsen
Department of Radiology, Erasmus MC – University Medical Center, Rotterdam, The Netherlands

[b] G. C. Houston
Applied Science Laboratory, General Electric Healthcare, Den Bosch, The Netherlands

Abstract

Various studies have shown that various cell types can be labeled with iron oxide particles and visualized by magnetic resonance imaging (MRI). However, reported protocols for cell labeling show a large variation in terms of labeling dose and incubation time. It is therefore not clear how different labeling protocols may influence labeling efficiency. Systematic assessment of the effects of various labeling protocols on labeling efficiency of human umbilical vein endothelial cells (HUVEC) using two different types of iron oxide nanoparticles, i.e. super paramagnetic iron oxide particles (SPIOs) and microparticles of iron oxide (MPIOs), demonstrated that probe concentration, incubation time and particle characteristics all influence the efficiency of label incorporation, label distribution, label retention and cell behavior. For SPIO the optimal labeling protocol consisted of a dose of 12.5 mg iron/2 ml/9.5 cm^2 and an incubation time of 24 h, resulting in an average iron load of 12.0 pg iron/per cell (uptake efficiency of 9.6%). At 4 h many SPIOs are seen sticking to the outside of the cell instead of being taken up by the cell. For MPIO optimal labeling was obtained with a dose of 50 mg iron/2 ml/9.5 cm^2. Incubation time was of less importance since most of the particles were already incorporated within 4 h with a 100% labeling efficiency, resulting in an intracellular iron load of 626 pg/cell. MPIO were taken up more efficiently than SPIO and were also better tolerated. HUVEC could be exposed to and contain higher amounts of iron without causing significant cell death, even though MPIO had a much more pronounced effect on cell appearance. Using optimal labeling conditions as found for HUVEC on other cell lines, we observed that different cell types react differently to identical labeling conditions. Consequently, for each cell type separately an optimal protocol has to be established.

Keywords: cell imaging; MRI; iron oxide; SPIO; MPIO

1   Introduction

Cell-based therapy approaches are currently receiving a lot of attention for regenerative medicine purposes (1). In order to assess the clinical value and safety of cell therapy approaches, it is necessary to track the fate of the transplanted cells *in vivo*. For *in vivo* cell tracking it is essential that the cells have incorporated a label in order to distinguish them from their surroundings in MR images (2–5). The easiest way to label a cell is to add the label to the culture medium. To improve uptake efficiency, a transfection agent can be used (5). In labeling of cells some aspects have to be considered:

(1)   the efficiency of the labeling procedure;
(2)   the effect of labeling on cell survival;
(3)   the behavior of the label in the cell;
(4)   the duration of label retention in the cell;
(5)   preservation of cell function and surface marker expression.

For cell tracking by MRI different labels can be used (1,6,7). Iron-oxide nanoparticles are, however, the most commonly used labels, and were even shown to allow for detection of single cells *in vivo* (8). A vast amount of studies have been published dealing with labeling of various cell types with iron oxide nanoparticles (9–11). In these studies a large variety of labeling protocols have been described (12–14). While for every cell type tested efficient labeling and subsequent detection by MRI has been reported, it is not clear how different labeling protocols may influence labeling efficiency. Various studies have shown effects of particle coating, particle size, labeling dose and labeling time on labeling efficiency and the ability to detect labeled cells by MRI (15–18). The purpose of this study was to systematically investigate the effect of variations in dose and duration of labeling on label incorporation, distribution, retention and toxicity using two commonly applied types of iron oxide nanoparticles – the so-called SPIO (super paramagnetic iron oxide particles) and MPIO (micro particles of iron oxide) particles. Of these two, the most widely used are SPIO particles, which have a particle diameter between 80 and 150 nm, consisting of an iron oxide core (Fe_2O_3 and Fe_3O_4 crystals) of 4 nm with a low-molecular-weight dextran coating (19–23). MPIO particles are composed of polystyrene–divinyl benzene polymer micro spheres containing a magnetite core and are tagged with the fluorescent dye Dragon

green (480/520 nm). These particles are highly effective $T_2{}^*$ contrast agents, and can also be imaged by fluorescence microscopy and used in fluorescent activated cell sorting (FACS) studies. MPIO have an average size of 1630 nm and have been shown to be functionally inert (24,25). Both SPIO and MPIO are efficiently endocytosed by many cell types and passed along to daughter cells during mitosis. Cell cycle analysis demonstrates that the labeling process does not have a negative impact on the cell cycle profile in comparison with non-labeled cells (26,27).

2   Results

2.2.   Labeling efficiency

2.1.1.   Iron uptake

Labeling efficiency of human umbilical vein endothelial cells (HUVECs) is dependent on various labeling parameters: the dose of iron that the cells are exposed to, the incubation time used and the type of iron oxide nanoparticle used (Fig. 1A, B). Using an incubation time of 4 h and doses of 6.25 mg iron/ 2 ml/9.5 cm^2, less than 50% of the cells were labeled as assessed by Prussian blue staining. This was also the case for an incubation time of 24 h and a dose of 3.13 iron/2 ml/9.5 cm^2. These conditions were therefore not used to measure the average iron content per cell. High concentrations at long incubation times were also not further analyzed since these conditions led to significant cell death (see further below).

For SPIO a maximal iron load of 1.82 mg per 100 000 cells was obtained, representing an average iron load of 18.2 pg per cell. A much higher iron load was achieved with MPIO particles. With MPIO a maximal iron load of 66.1 mg per 100 000 cells was achieved, corresponding to an average iron load of 661 pg per cell. Note that the conditions under which these maximal iron loads were achieved for the two different iron oxide formulations were not the same. In the case of SPIO, maximal incorporation was achieved when cells were exposed to 25 mg iron/2 ml/9.5 cm^2 for 24 h. In the case of MPIO, maximal incorporation was achieved within 4 h of incubation using an iron oxide dose of 100 mg iron/2 ml/9.5 cm^2. As displayed in Fig. 1(C–E), uptake of MPIO is much more efficient than uptake of SPIO. For MPIO the uptake efficiency

ranged from 60 to 100% in terms of the amount of iron taken up relative to the labeling dose. For SPIO uptake efficiency was maximally 9.6%.
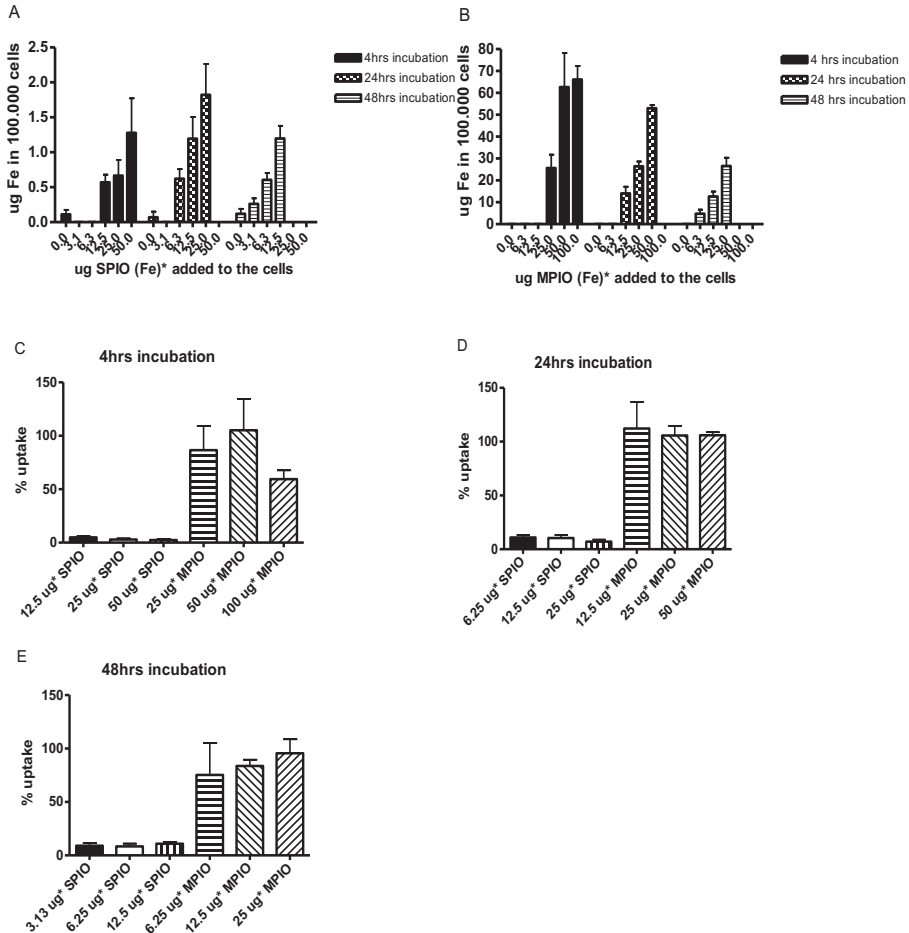

Figure 1 Labeling efficiency: Incorporation of iron (SPIO or MPIO) in the cell. A and **B** Amount of iron taken up by 100,000 cells as measured by ICP-OES. Closed bars represent the iron uptake within 4 hrs. Dotted bars show the uptake within 24hrs and the striped bars represent an incubation time of 48hrs. Note the difference in scale for SPIO **A** and MPIO **B**. **C** percentage of iron which is taken up by the cells relative to the labeling dose with incubation time 4hrs. **D** Similar to **C** with incubation time 24hrs. **E** Similar to **C** with incubation time 48hrs. * Doses listed are in mg of iron/2 ml/9.5cm^2.

2.1.2.   Label distribution

Distribution of label within the cell population and within the cell is also dependent on the labeling protocol used. For MPIO, cell labeling efficiency in terms of the percentage of cells labeled as assessed by Prussian blue staining soon reached a plateau. As shown in Fig. 2(A), >85% of the cells were labeled at doses of 6.25 mg iron/2 ml/9.5 cm . For SPIO a minimum amount of 12.5 mg iron/2 ml/9.5 cm^2 was needed to ensure that all cells were labeled. Differences in labeling efficiency between SPIO and MPIO were also found in terms of distribution of iron oxide complexes per cell. Following an incubation time of 4 h, iron oxide complexes were mostly attached to the outside of the cell, in case of SPIO, while for MPIO, most of the label was found within the cell (Fig. 2B). Differences seen in the location of MPIO particles depending on the incubation time used were also seen. Following 4 h of incubation, MPIO particles were spread throughout the cell as opposed to a more perinuclear clustering of the particles following incubation for 24 or 48 h (Fig. 2C). This latter observation probably reflects intracellular trafficking of the endosomes occurring after internalization of the cells, and most likely also occurs at later time points following a short incubation time.

2.1.3.   Label retention

As shown above, the amount of label incorporated by HUVECs is strongly dependent on both the labeling dose and the incubation time used. This effect was most pronounced for SPIO. For instance at a dose of 12.5 mg iron/2 ml/9.5 cm^2 the average iron load increased from 7.5 to 12.0 mg iron/cell when incubation times were increased from 4 to 24 or 48 h. For MPIO, longer incubation times generally did not result in significantly higher intracellular iron loads. For instance, at a dose of 25 mg MPIO the average intracellular iron load was similar for incubation times of 4, 24 and 48 h. As can be appreciated from in Fig. 1, for SPIO comparable iron loads were obtained when cells were labeled with 50 mg for 4 h, or with 25 mg for 24 h, or with 12.5 mg for 48 h. To assess whether the potentially different kinetics of iron uptake under these conditions may result in differences in label retention we counted the percentage iron-positive cells over time, for cells labeled according to these three protocols. These experiments revealed that, 1 week post-labeling, more cells contained detectable amounts of iron oxide when a short incubation time

with a high dose of SPIO was used, compared with the use of a long incubation time with a lower dose of SPIO (26 vs 16%; $p < 0.05$; Fig. 3).
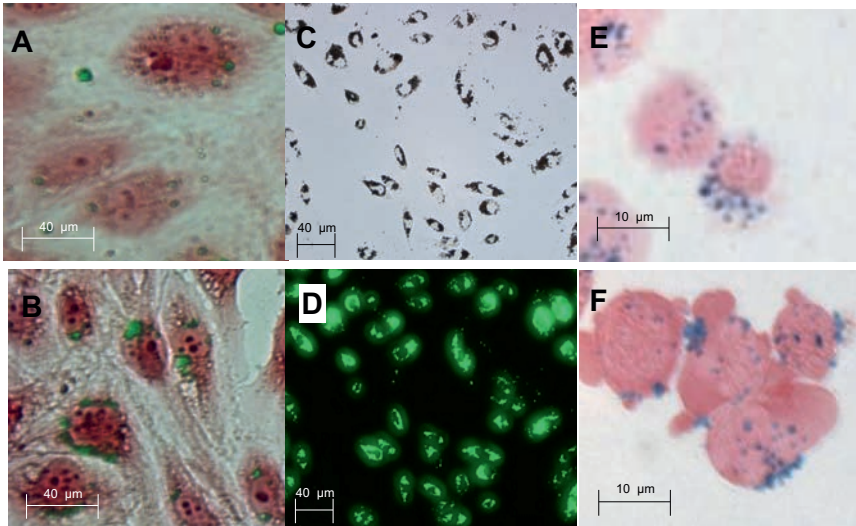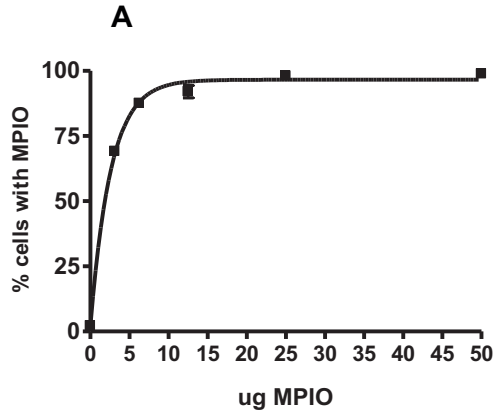

Figure 2 Label distribution A Percentage of cells labeled using different labeling doses and an incubation time of 24 hrs. **B** Label distribution following labeling for 4hrs with 25 mg MPIO. Label (Dragon green) is seen attached to the outside of the cell and also distributed within the cell **C** Label distribution following labeling for 48hrs with 25 mg MPIO. Label (Dragon green) is seen clustered around the cell nucleus **D-E**. Corresponding light and fluorescence microscopy images of HUVEC labeled with 25 mg MPIO for 24 hrs illustrating the high MPIO load inside cells. **F** Label distribution following labeling for 4 hrs with 50 mg SPIO. Label (blue=iron staining) is seen attached to the outside of the cell. **G** Label distribution following labeling for 24 hrs with 25 mg SPIO. Label (blue=iron staining) is seen clustered around the cell nucleus.

For all samples, when iron-positive cells could be visualized by Prussian blue staining, sensitive imaging by MRI at the single cell level *in vitro* was possible as exemplified in Fig. 4.
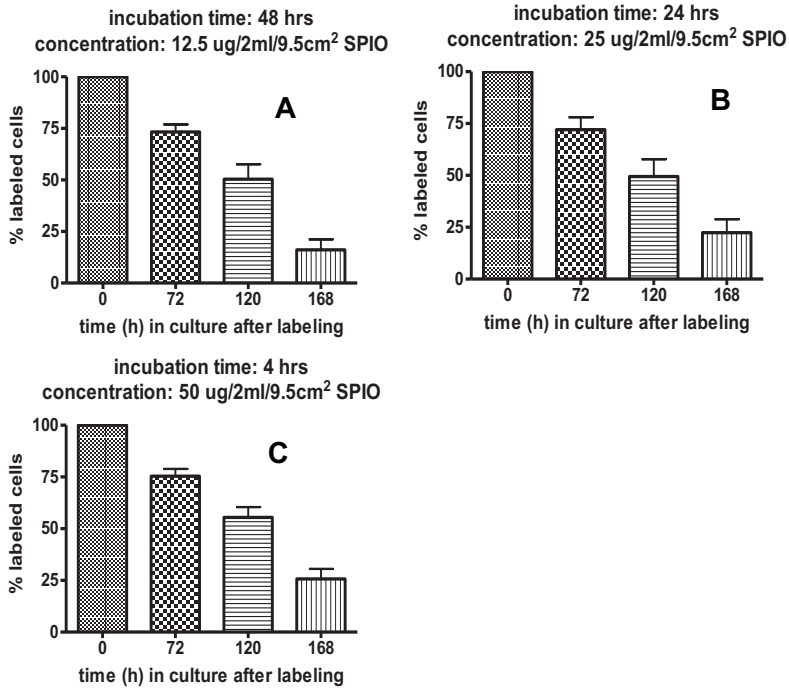
incubation time/labeling dose	% labeled cells
4 hrs 50 ug iron/2ml/9.5cm^2	25.6 ± 4.9
24 hrs 25 ug iron/2ml/9.5cm^2	22.3 ± 6.5
48 hrs 12.5 ug iron/2ml/9.5cm^2	16.1 ± 5.1*

Figure 3 Label retention. HUVECs were labeled with three different labeling protocols that each resulted in an approximate iron load of approximately 1.25 mg iron per 100.000 cells A, i.e. 12.5 mg for 48 hrs **B**, 25 mg for 24 hrs and 50 mg for 4 hrs **C**. The number of Prussian blue positive cells over time was determined. These results show that the label retention is better when incubated for 4hrs with 50 mg SPIO (C) than with a lower dose for a longer time (**A** and **B**). The percentage of Prussian blue positive cells 1 week after labeling is listed in the table. * Significantly different from 4 hrs and 24 hrs.

2.2. Toxicity

2.2.1. Cell survival

Toxicity of the labeling procedure was dependent on both the labeling dose and the incubation times used. At incubation times of 24 and 48 h significant cell death of more than 50% of the cells was seen at doses of 50 and 25 mg, respectively, for SPIO and at doses of 100 and 50 mg, respectively, for MPIO. These conditions were therefore not used in other studies. For the other doses and incubation times tested, cell viability was between 80 and 100% (Fig. 5C). For both MPIO and SPIO higher doses were tolerated at shorter incubation times. At equal incubation times, MPIO was better tolerated than SPIO. For example, at incubation times of 24 h, a dose of SPIO 50 mg resulted in a loss of cell viability of 50% while for MPIO cell viability was 80% at this dose.

2.2.2. Cell morphology

At the highest doses tested for each of the incubation times that did not affect cell survival too severely (cell viability 80%), a change in morphology of the cells was observed. This change involved a more spindle-like appearance of the cells in culture. In FACS studies, clear changes in forward scatter and side scatter plots, corresponding to changes in cell size and cell granularity, respectively, were observed following labeling

(Fig. 5A and B). Both effects were more pronounced after labeling with MPIO than with SPIO. At the highest doses of MPIO tested cell sizes increased 4–7 times in cell volume compared with unlabeled control cells. Cell volumes were calculated from the average measured length and the width of labeled and unlabeled cells and the assumed height of 0.5x the cell width using the formula to calculate the volume of an ellipsoid.

2.2.3. Cell function

Unlabeled (control) HUVECs show tube formation when seeded on matrigel (Fig. 6). This phenomenon is already apparent after 4 h. After 24 h the tubular network is much finer of structure. The effects of SPIO and MPIO labeling on tube forming capacity of HUVECS were tested at all doses that did not significantly affect cell survival. For all these conditions tested, HUVECs still displayed tube forming capacity (Fig. 6).

2.2.4. Labeling efficiency in other cell types

Based on all findings, i.e. labeling efficiency in terms of percentage of cells labeled, label incorporation, label retention and retention of cell viability and cell function, we found the optimal labeling conditions for HUVECs to consist of a labeling dose of 12.5 mg/2 ml/9.5 cm^2 and an incubation time of 24 h in the case of SPIO, and in the case of MPIO to consist of a labeling dose of 50 mg/2 ml/9.5 cm^2 and an incubation time of 4 h.
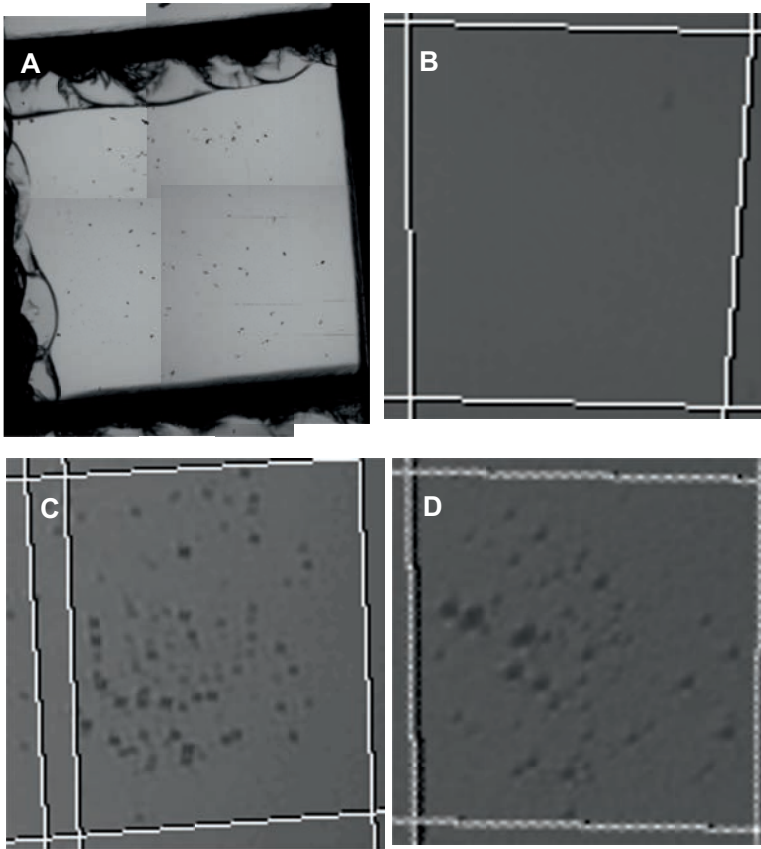

Figure 4 MR visibility of labeled cells. Representative images showing the high imaging sensitivity that can be reached for the various labeling conditions. A Composition of light microscopy images showing a small sample preparation (demarcated region of interest is approximately 1 mm by 1 mm) of (labeled) HUVECs in culture as used from MR imaging. **B** MR Image of a comparable region of interest of a sample containing unlabeled cells. **C** MR Image of a comparable region of interest of a sample containing cells labeled with SPIO at a dose of 12.5 mg/2ml/9.5 m^2 for 24 hrs 5 days after labeling. **D** MR Image of a comparable region of interest of a sample containing cells labeled with MPIO at a dose of 25 mg/2ml/9.5 m^2 for 4 hrs 5 days after labeling.

2

Using these optimal labeling conditions for HUVEC, we also labeled human chondrocytes and murine myoblast cells (C2C12) with SPIO and MPIO particles. In both cell types, labeling efficiency with SPIO particles was similar to that observed in HUVEC. For MPIO, however, labeling efficiency was considerably less in these cell types. For C2C12, labeling of all cells was only achieved at doses of 12.5 mg iron/2 ml/9.5 cm^2 and an incubation time of 24 h. Also different was the reaction of these cells to incorporation of MPIO. Following incorporation of MPIO, morphological changes as observed in HUVEC were far less pronounced in C2C12 cells (Fig. 7). Remarkably, labeling of chondrocytes with MPIO was highly inefficient. No incorporation of label occurred using an incubation time of 4 h. Using a dose of 100 mg iron/2 ml/9.5 cm^2 MPIO and an incubation time of 24 h maximally 70% of the cells showed incorporation of MPIO particles.

3.   Discussion

This study was set up to learn more about the effect labeling conditions have on the incorporation, distribution and retention of iron oxide nanoparticles. In the vast amount of studies dealing with labeling of cells with iron oxide nanoparticles, a large variation of labeling protocols is encountered; labeling doses varying from 1 to 2800 mg/ml and incubation times varying from 1 to 72 h have been described (28–30). Generally, higher doses, longer incubation times, larger particle size and the use of lipofection techniques result in increased labeling efficiency (15,16,18). While in most of these studies labeling in the absence of major adverse effects is reported, it remains unclear what the influence of different labeling protocols is on label incorporation, label distribution and label retention.

As shown in this study, each of these aspects is strongly influenced by the exact labeling protocol used. In terms of intracellular iron load, the optimal labeling protocol for HUVEC using SPIO (Endorem) consisted of a labeling dose of 12.5 mg SPIO/2 ml/surface area of 9.5 cm^2 and an incubation time of 24 h. With this protocol an average iron load of 12.0 pg iron/per cell was obtained. This corresponds to an uptake efficiency of 9.6%. If a significantly shorter labeling time is used (4 h) many SPIOs are seen sticking to the outside of the cell instead of being taken up by the cell. As reported by Metz *et al.*,
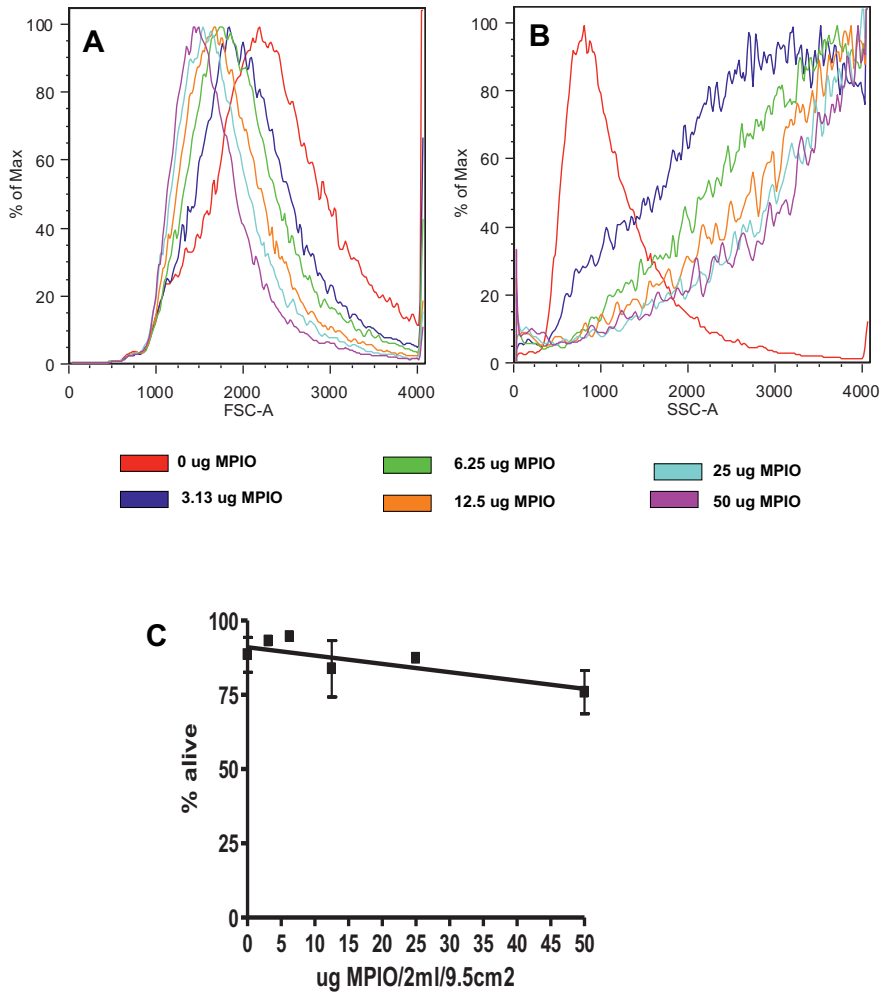
Figure 5 Toxicity. A Forward scatter FACS plots showing increases in cell size with increasing MPIO incorporation. **B** Side scatter FACS plots showing increases in cell granularity with increasing MPIO incorporation. **C** Cell viability of cells labeled for 24 hrs with increasing doses of MPIO.

at some point a plateau of intracellular incorporation of ferumoxides will be achieved when doses and/or labeling times are being increased. They tested doses of up to 2000 mg/ml for labeling of human monocytes and did not find a major increase in intracellular iron content or susceptibility effect in MR images (16). In addition, large amounts of extracellular iron sticking to the cell have been reported to diminish the chondrogenic differentiation capacity of

2

MSC. High intracellular amounts of iron and/or exposure of MSCs to high iron concentrations also inhibited chondrogenic differentiation capacity of MSCs (31,32). Not only the labeling dose but also exposure time were factors in creating this adverse effect.

For MPIO optimal iron incorporation was obtained with a dose of 50 mg iron/2 ml/9.5 cm^2. For MPIO the labeling time was of lesser importance since most of the particles were already taken up within 4 h with a 100% labeling efficiency. Under these conditions, the resulting intracellular iron load is 626 pg/cell. This is significantly higher than reported in other studies using different cell types (9,25). In these studies murine hepatocytes were labeled with MPIOs and they generally contained iron levels of 100 pg. On occasion, some cells had levels as high as 400 pg. Macrophages labeled with 1.63 mm MPIOs had an average cellular iron uptake of 39.1 pg/cell, corresponding to approximately 35 particles per cell.

Because of the high uptake efficiency of MPIO, a relatively low dose of 6.25 mg iron results in the labeling of all cells. However, at this dose an incubation time of 24 h is needed. For a dose of 50 mg MPIO, an incubation time of 4 h suffices to label all cells and uptake of most of the iron particles. This shorter incubation time, however, results in a different intracellular distribution of the iron than longer incubation times. After a 4 h incubation period, MPIO particles are homogenously distributed over the cytoplasm. In contrast, after an incubation time of 24 or 48 h, the MPIO particles are found clustered around the cell nucleus. This latter observation is most likely due to intracellular cell trafficking of the endosomes that occurs in time after uptake of the particles. For HUVEC, increasing labeling doses and consequently increasing intracellular iron loads result in more pronounced changes of morphological features. The cells become more spindle-like, larger in size and more granulated. Such effects were not seen in murine monocytes/macrophages in a study by Valable *et al*. using similar assays (27). As shown in this paper, the labeling efficiency of SPIO is significantly less than for MPIO. Higher doses and longer incubation times are needed to achieve labeling of all the cells. Also, HUVEC displayed a higher tolerance for MPIO than for SPIO. This means that more iron can be brought inside the cell with MPIO in a short period of time. In terms of labeling dose and incubation time the SPIO labeling efficiency was much

more dependent on the exact labeling protocol used. The highest intracellular iron loads without major adverse effects were obtained with incubation times of 24 h and intermediate labeling doses. Alternatively, better retention of label was observed after short incubation times and high labeling doses. This latter observation may be explained by differences in endocytosis kinetics, as depicted in Fig. 8. Labeling with high doses and short incubation times may result in large intracellular vesicles with multiple iron-oxide complexes. Labeling with low doses and long incubation times may result in small intracellular vesicles with just one iron-oxide complex. Following cell division the vesicles will be divided over the daughter cells; however, the vesicles themselves will not divide. Through these dynamics, the high dose and short
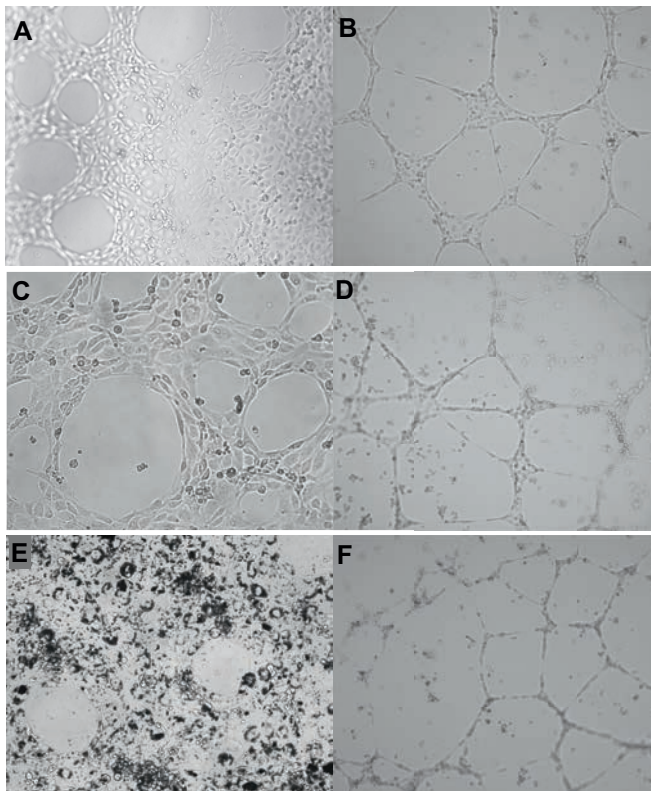
Figure 6 Cell function: tube forming capacity. Unlabeled and labeled HUVECS were seeded on matrigel and tube forming capacity was monitored after 4 hrs (**A**, **C** and **E**) and after 24 hrs (**B**, **D** and **F**). After 4 hrs initial tube formation is apparent for unlabeled cells **A**, SPIO labeled cells (12.5 mg SPIO for 24hrs) and MPIO labeled cells (50 mg MPIO 4hrs). A fine tubular matrix is apparent after 24 hrs for each of the conditions (**B**: unlabeled; **D**: SPIO labeled; **F**: MPIO labeled).

incubation time may result in more cells containing enough iron for detection after multiple cell divisions. For both MPIO and SPIO, no major effect on cell function in terms of tube forming capacity was observed, even at doses that did result in changes in morphological features and some cell death (< 20%).

For tracking of single cells by MR, labeling with MPIO appears to be most suitable. Only one iron particle is sufficient for detection (26). MPIO particles have higher relaxivity than SPIOs, based on equivalent iron content. The labeling protocol is easier for MPIO than for SPIO. No transfection agent is needed, medium with serum can be used and the labeling time is much shorter (4 h compared with 24 h for SPIO). MPIOs also contain a fluorescent tag, so they can be readily used in multi-modality imaging approaches combining MRI with optical imaging. However, MPIOs as used in this and other studies are not intended for clinical use but for experimental use only. SPIOs, however, exist in clinically approved formulations and have been used in clinical settings already (33–35). SPIOs are therefore better suited to clinical applications.

Using optimal labeling conditions as found for HUVEC for both SPIOs and MPIOs on other cell lines, we observed that different cell types react differently to identical labeling conditions. The mouse myoblast cell line C2C12 shows no change in cell size after administrating MPIO as opposed to HUVEC. Also, the high labeling efficiency found for MPIO in HUVEC was much less in C2C12 cells and labeling was absolutely absent in chondrocytes at an incubation time of 4 h. Even at doses of 50–100 mg and incubation times of 24 h, chondrocytes showed limited uptake. In contrast, a 100% labeling efficiency could be obtained with SPIO in these cells (36). In studies by Arbab *et al*. (19,37), significant differences in cell apoptosis and label incorporation were also found between different cell types when identical labeling protocols were used.

4.   Conclusion

HUVECs can be labeled efficiently both with SPIO and MPIO but dose and duration of exposure of cells to these particles strongly influence label incorporation, label distribution and label retention. Optimal label incorporation requires different protocols for SPIO and MPIO. Applying

optimized protocols for HUVECS to different cell lines shows that no standard labeling protocol is useful for all the cell types growing *in vitro*. Consequently, an optimal labeling protocol has to be determined for each cell type in combination with the specific particle separately.

# 5.   Experimental procedures

5.1.   Cell culture

For extensive assessment of the effects of labeling dose and duration primary culture HUVECs were used. HUVECs were grown in endothelial growth medium (EGM-2 bullet kit CC3156 with CC4176; Cambrex, Verviers, Belgium) in a six-well plate (Corning Incorporated, New York, USA) with a surface growth area of 9.5 cm^2. For assessment of the general applicability of our findings, optimal labeling protocols as found for HUVEC were used for labeling of a murine myoblast cell line, C2C12 and human chondrocytes. C2C12 cells were cultured in Dulbecco's modified Eagle medium + 4500 mg/l D-glucose (Invitrogen, Breda, The Netherlands) + 1% (v/v) penicilline/streptomycine [10.000 U penicilline/ml + 10.000 mg streptomycine/ml (Cambrex, Verviers, Belgium)] + 10% (v/v) fetal bovine serum (Cambrex, Verviers, Belgium). Chondrocytes were cultured in chondrocyte expansion medium as described previously (38).

5.2.   SPIO labeling

Labeling of cells with SPIO was performed at 90% confluence using Endorem (Guerbet S.A., Paris, France) and lipofectamine 2000 (Invitrogen, Breda, The Netherlands) (21). A labeling stock solution of 215 mg Fe/ml was prepared as follows: 10 ml Endorem was added to 250 ml Opti-MEM (Invitrogen, Breda, The Netherlands) and 10 ml of lipofectamine was added to 250 ml Opti-MEM. After 5 min the two solutions were mixed together and the resulting suspension was incubated at room temperature for 20 min. After washing the cells with phosphate-buffered saline (PBS) (Invitrogen, Breda, The Netherlands), the culture medium was replaced by 2 ml Opti-MEM and the SPIO–lipofectamine suspension (0, 3.13, 6.25, 12.5, 25, 50 mg) was added drop-wise to the medium such that an equal distribution of SPIO–lipofectamine complexes was obtained in the well. The cells were then incubated for 4, 24 or 48 h at 37°C/ 5% CO$_2$. Before further use of labeled cells, the monolayer cultures were rinsed three times with

PBS, and incubated with 10% fetal calf serum (Cambrex, Heerhugowaard, The Netherlands) for 1 h, to remove loose SPIO-lipofectamine complexes.
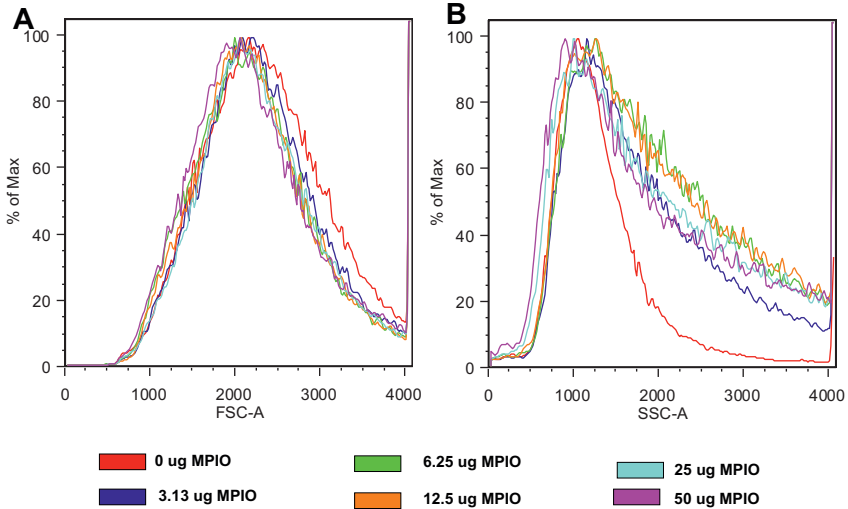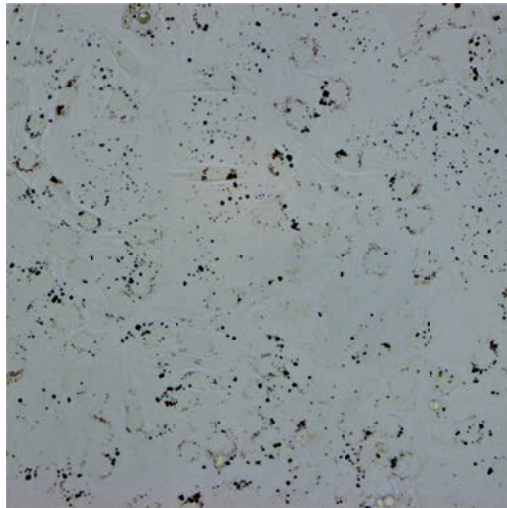
Figure 7 Labeling of C2C12 cells with MPIO. A Forward scatter FACS plots showing no change in cell size following labeling with MPIO in C2C12 cells as opposed to the observation in HUVECs shown in Figure 4. **B** Side scatter FACS plots showing also increases in cell granularity of C2C12 cells with increasing MPIO incorporation. **C** Light microscopy image of C2C12 cells in culture after labeling with MPIO at a dose of 25 mg iron/2ml/9.5cm^2 for 24 hrs. Note the large amount of MPIO still present outside the cells.

5.3. MPIO labeling

Labeling of cells was performed using MPIO (Bangs laboratories, Fisher, IN, USA) at 90% confluence. Different amounts of iron (0, 3.13, 6.25, 12.5, 25, 50 mg which correspond to 0, 2.79 x 10^6, 5.58 x 10^6, 1.12 x 10^7, 2.23 x 10^7 and 4.47 x 10^7 particles) were added drop-wise to the cells, which were grown in complete culture medium. For 4, 24 or 48 h the cells were incubated at 37°C/5% CO_2. Before further use of labeled cells, the monolayer cultures were rinsed three times with PBS (Invitrogen, Breda, The Netherlands).
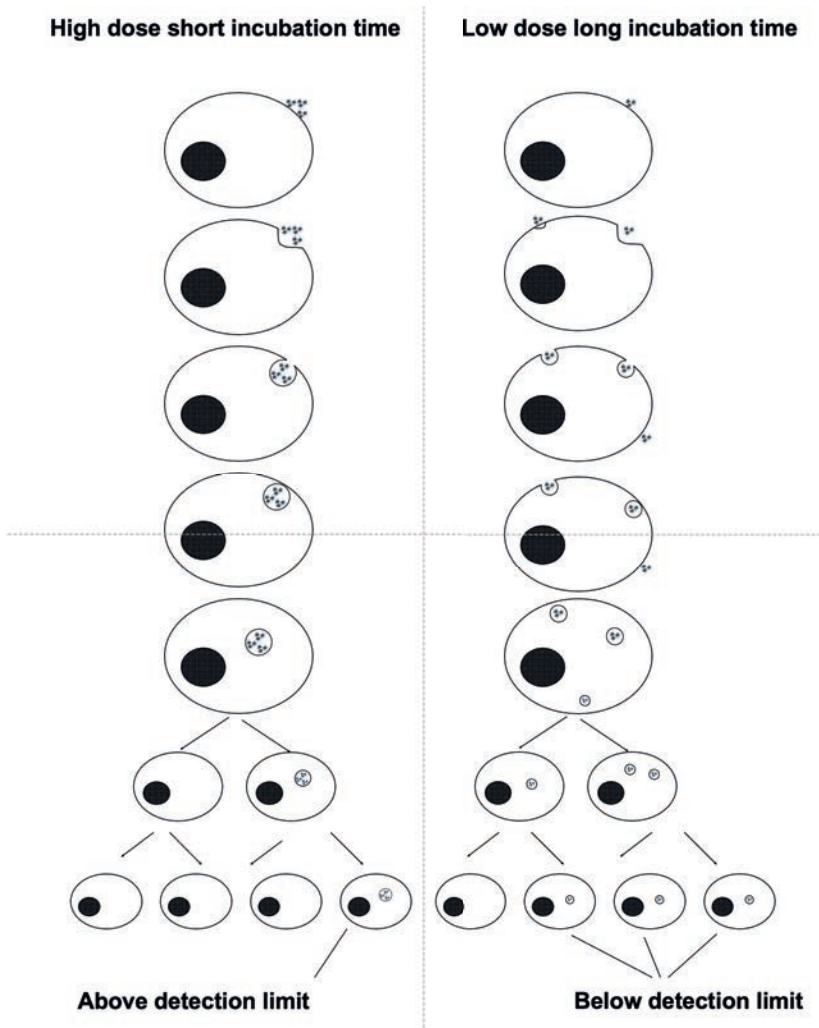

Figure 8 Endocytosis dynamics. Hypothesized difference in endocytosis dynamics using different labeling protocols.

5.4. Incorporation of iron

5.4.1. Inductively coupled plasma–optical emission spectrometry

Cell pellets of unlabeled and labeled cells were dried for 72 h at 60°C. Subsequently they were digested in 40 ml of a 3:1 mixture of ultra-pure perchloric acid (EM Science, Gibbstown, NJ, USA) and ultra-pure nitric acid (JT Baker, Deventer, The Netherlands) at 60°C for 6 h. The standard line with different dilutions of Endorem or MPIO underwent the same procedure as the cells. To the digested substance 4 ml MiliQ was added and the amount of iron was determined with a Perkin Elmer Optical Emission Optima 4300 DV Spectrometer at 259 nm. The experiments were performed three times with triplicate samples. Uptake efficiency was calculated as the amount of iron measured in the labeled cells divided by the total amount of iron added for labeling multiplied by 100%.

5.4.2. Fluorescence activated cell sorting

The MPIO were tagged with Dragon Green, which is fluorescent. To analyze the amount of MPIO taken up by the HUVEC and to assess the effects of MPIO on morphological characteristics of the cell and cell survival, a FACS (FacsCanto, Becton Dickinson, Alphen a/d Rijn, The Netherlands) analysis was performed. After incubation with MPIO all the cells were collected and resuspended in FACS buffer (0.25% BSA, 0.5 m$_M$ EDTA, 0.05% NaN$_3$), and 1% v/v propidium iodide (all from Sigma-Aldrich, Zwijndrecht, The Netherlands) was added to determine the amount of dead cells in the suspension. The wavelength used was 488 nm. Cell size was estimated using the forward scatter parameter and the side scatter parameter was used to determine the cytoplasmic granularity.

5.5. Localization of iron complexes and label retention

For assessing the localization of the iron complexes within the cell, cytospin slides were prepared from labeled cells. A cell suspension of 2 x 10^5 cells/ml was made and 150 ml was loaded in each cuvette. The cells were centrifuged (7 min, 800 rpm; Shandon Inc.) onto the slide. After the slides were dried by air the cells were fixed in methanol absolute (Sigma-Aldrich, Zwijndrecht, The Netherlands) and Prussian blue staining (Sigma-Aldrich, Zwijndrecht, The Netherlands) was performed. The slides were covered with a cover slip and imaged with an Axiovert S100 microscope (Zeiss, Oberkochen, Germany).

The cytospins were also used to study retention of the iron inside the cell over time. The total number of cells was counted and the number of cells stained with Prussian Blue (blue coloration of the iron) was counted in three randomly selected fields of view (objective 40 x) per time point.

5.6.   Cytotoxicity and viability assays

5.6.1.   Distribution of iron and cell morphology: Prussian blue staining

To study the effect of SPIO labeling on cell morphology and label distribution using different labeling protocols, labeled cells were washed with PBS and photographed at a light microscope. The cells were then fixed with 4% formalin. After 10 min of fixation, the samples were washed again and stained for 20 min with a freshly prepared solution containing 0.12 $_M$ $K_4Fe(CN)_6$ and 1 $_M$ HCl (Sigma-Aldrich, Zwijndrecht, The Netherlands). The cells were washed again and the cytoplasm was stained with 1% w/v pararosaniline solution. Samples were washed a final time and examined by light microscopy. The appearance of the cells and the place where the iron was taken up in the cells was qualitatively scored.

5.6.2.   Cell functionality: Matrigel test

SPIO- and MPIO-labeled HUVEC were seeded on Matrigel to study the tube-forming capacity of the labeled cells (Matrigel Basement Membrane Matrix, Becton Dickinson, Alphen aan den Rijn, The Netherlands). After 4 and 24 h the cells were screened with a light microscope and photographed.

5.6.3.   Visualization by MRI

All data acquisition was performed on a GE (HD) 3 T clinical MRI scanner using unmodified gradients and specially designed reception coils, to provide the best signal-to-noise (SNR) performance for the desired field-of-view.

For *in vitro* imaging of labeled cells, cells were harvested by trypsinization and a cell suspension was prepared in appropriate culture medium at a cell concentration of 50 cells/10 ml. On the bottom of a four-well culture plate (VWR international NUNC176740; Amsterdam, the Netherlands), a grid with rectangles of about 1.5 mm^2 was carved (Fig. 4). This grid served as location marker for subsequent MR imaging sessions. A 10 ml aliquot of the cell suspension was seeded into the well, within the surface area of a single

rectangle of the grid. The cells were allowed to sediment and adhere to the bottom of the well before additional medium was added. Directly before each MRI scan, the medium was replaced with fresh medium containing Gd-DTPA (Magnevist, Bayer Schering Pharma AG, Berlin, Germany) at a v/v ratio of 1:200 to provide enhanced SNR and contrast-to-noise (CNR) ratios using T_1-weighted protocols to decrease imaging time. The grid was filled with ultrasound gel, to provide contrast in MR images. Each sample was placed over a single-loop solenoid coil with an inner diameter of 1.0 cm (Flick Engineering Solutions, The Netherlands). The distance between the loop and the cell monolayer was 1.3 mm, which was the thickness of the bottom of the plate. The scan protocol was limited to a three-plane localizer followed by a high-resolution 3DT_1-weighted scan. The following scan parameters were used: 3D-SPGR sequence with *TR/TE* 41.1/10.5 ms, and a flip angle (a) of 508 with a resolution of 38 x 38 mm x 100 mm and a FOV of 2 x 2 cm and an imaging time of 13 min.

5.7. Data analysis and statistics

Data are expressed as mean ± SD from triplicate samples in two or three repeated experiments. Statistical analysis of differences between data sets was performed by ANOVA (Graphpad Prism 4.0, GraphPad Software, La Jolla, CA, USA) followed by a *post hoc* test (Newman-Keuls Multiple Comparison Test). A *p*-value of <0.05 was considered significant.

Acknowledgments

References

1. Bulte JW, Kraitchman DL. Monitoring cell therapy using iron oxide MR contrast agents. Curr Pharm Biotechnol 2004; 5: 567–584.

2. Bulte JW. Intracellular endosomal magnetic labeling of cells. Meth Mol Med 2006; 124: 419–439.

3. Modo M, Hoehn M, Bulte JW. Cellular MR imaging. Mol Imag 2005; 4: 143–164.

4. Hoehn M, Wiedermann D, Justicia C, Ramos-Cabrer P, Kruttwig K, Farr T, Himmelreich U. Cell tracking using magnetic resonance imaging. J Physiol 2007; 584: 25–30.

5. Frank JA, Anderson SA, Kalsih H, Jordan EK, Lewis BK, Yocum GT, Arbab AS. Methods for magnetically labeling stem and other cells for detection by in vivo magnetic resonance imaging. Cytother- apy 2004; 6: 621–625.

6. Aime S, Barge A, Cabella C, Crich SG, Gianolio E. Targeting cells with MR imaging probes based on paramagnetic Gd(III) chelates. Curr Pharm Biotechnol 2004; 5: 509–518.

7. Mulder WJ, Strijkers GJ, Habets JW, Bleeker EJ, van der Schaft DW, Storm G, Koning GA, Griffioen AW, Nicolay K. MR molecular imaging and fluorescence microscopy for identification of acti- vated tumor endothelium using a bimodal lipidic nanoparticle. Faseb J 2005; 19: 2008–2010.

8. Shapiro EM, Sharer K, Skrtic S, Koretsky AP. In vivo detection of single cells by MRI. Magn Reson Med 2006; 55: 242–249.

9. Brekke C, Morgan SC, Lowe AS, Meade TJ, Price J, Williams SC, Modo M. The in vitro effects of a bimodal contrast agent on cellular functions and relaxometry. NMR Biomed 2007; 20: 77–89.

10. Farrell E, Wielopolski P, Pavljasevic P, van Tiel S, Jahr H, Verhaar J, Weinans H, Krestin G, O'Brien FJ, van Osch G, Bernsen M. Effects of iron oxide incorporation for long term cell tracking on MSC differentiation in vitro and in vivo. Biochem Biophys Res Commun 2008; 369: 1076–1081.

11. Hoehn M, Kustermann E, Blunk J, Wiedermann D, Trapp T, Wecker S, Focking M, Arnold H, Hescheler J, Fleischmann BK, Schwindt W, Buhrle C. Monitoring of implanted stem cell migration in vivo: a highly resolved in vivo magnetic resonance imaging investi- gation of experimental stroke in rat. Proc Natl Acad Sci USA 2002; 99: 16267–16272.

12. Rudelius M, Daldrup-Link HE, Heinzmann U, Piontek G, Settles M, Link TM, Schlegel J. Highly efficient paramagnetic labelling of embryonic and neuronal stem cells. Eur J Nucl Med Mol Imag 2003; 30: 1038–1044.

13. Shapiro EM, Skrtic S, Koretsky AP. Sizing it up: cellular MRI using micron-sized iron oxide particles. Magn Reson Med 2005; 53: 329–338.

14. Bulte JW, Duncan ID, Frank JA. In vivo magnetic resonance tracking of magnetically labeled cells after transplantation. J Cereb Blood Flow Metab 2002; 22: 899–907.

15. Matuszewski L, Persigehl T, Wall A, Schwindt W, Tombach B, Fobker M, Poremba C, Ebert W, Heindel W, Bremer C. Cell tagging with clinically approved iron oxides: feasibility and effect of lipofection, particle size, and surface coating on labeling effi- ciency. Radiology 2005; 235: 155–161.

16. Metz S, Bonaterra G, Rudelius M, Settles M, Rummeny EJ, Dal- drup-Link HE. Capacity of human monocytes to phagocytose approved iron oxide MR contrast agents in vitro. Eur Radiol 2004; 14: 1851–1858.

17. van Buul GM, Farrell E, Kops N, van Tiel ST, Bos PK, Weinans H, Krestin GP, van Osch GJ, Bernsen MR. Ferumoxides-protamine sulfate is more effective than ferucarbotran for cell labeling: implications for clinically applicable cell tracking using MRI. Contrast Media Mol Imag 2009; 4: 230–236.

18. Wu YL, Ye Q, Foley LM, Hitchens TK, Sato K, Williams JB, Ho C. In situ labeling of immune cells with iron oxide particles: an approach to detect organ rejection by cellular MRI. Proc Natl Acad Sci USA 2006; 103: 1852–1857.

19. Arbab AS, Yocum GT, Kalish H, Jordan EK, Anderson SA, Khakoo AY, Read EJ, Frank JA. Efficient magnetic cell labeling with protamine sulfate complexed to ferumoxides for cellular MRI. Blood 2004; 104: 1217–1223.

20. Neri M, Maderna C, Cavazzin C, Deidda-Vigoriti V, Politi LS, Scotti G, Marzola P, Sbarbati A, Vescovi AL, Gritti A. Efficient in vitro labeling of human neural precursor cells with superparamagnetic iron oxide particles: relevance for in vivo cell tracking. Stem Cells 2008; 26: 505–516.

2

21.   Zhang Z, van den Bos EJ, Wielopolski PA, de Jong-Popijus M, Bernsen MR, Duncker DJ, Krestin GP. In vitro imaging of single living human umbilical vein endothelial cells with a clinical 3.0-T MRI scanner. Magma 2005; 18: 175–185.

22.   Zhang Z, Jiang Q, Jiang F, Ding G, Zhang R, Wang L, Zhang L, Robin AM, Katakowski M, Chopp M. In vivo magnetic resonance imaging tracks adult neural progenitor cell targeting of brain tumor. Neuroimage 2004; 23: 281–287.

23.   Tallheden T, Nannmark U, Lorentzon M, Rakotonirainy O, Soussi B, Waagstein F, Jeppsson A, Sjogren-Jansson E, Lindahl A, Omerovic E. In vivo MR imaging of magnetically labeled human embryonic stem cells. Life Sci 2006; 79: 999–1006.

24.   Rodriguez O, Fricke S, Chien C, Dettin L, VanMeter J, Shapiro E, Dai HN, Casimiro M, Ileva L, Dagata J, Johnson MD, Lisanti MP, Koretsky A, Albanese C. Contrast-enhanced in vivo imaging of breast and prostate cancer cells by MRI. Cell Cycle 2006; 5: 113–119.

25.   Shapiro EM, Skrtic S, Sharer K, Hill JM, Dunbar CE, Koretsky AP. MRI detection of single particles for cellular imaging. Proc Natl Acad Sci USA 2004; 101: 10901–10906.

26.   Hinds KA, Hill JM, Shapiro EM, Laukkanen MO, Silva AC, Combs CA, Varney TR, Balaban RS, Koretsky AP, Dunbar CE. Highly efficient endosomal labeling of progenitor and stem cells with large magnetic particles allows magnetic resonance imaging of single cells. Blood 2003; 102: 867–872.

27.   Valable S, Barbier EL, Bernaudin M, Roussel S, Segebarth C, Petit E, Remy C. In vivo MRI tracking of exogenous monocytes/macro- phages targeting brain tumors in a rat model of glioma. Neuro-image 2007; 37 (suppl 1): S47–58.

28.   Lewin M, Carlesso N, Tung CH, Tang XW, Cory D, Scadden DT, Weissleder R. Tat peptide-derivatized magnetic nanoparticles allow in vivo tracking and recovery of progenitor cells. Nat Biotechnol 2000; 18: 410–414.

29.   Jendelova P, Herynek V, DeCroos J, Glogarova K, Andersson B, Hajek M, Sykova E. Imaging the fate of implanted bone marrow stromal cells labeled with superparamagnetic nanoparticles. Magn Reson Med 2003; 50: 767–776.

30.   Moore A, Sun PZ, Cory D, Hogemann D, Weissleder R, Lipes MA. MRI of insulitis in autoimmune diabetes. Magn Reson Med 2002; 47: 751–758.

31.   Henning TD, Wendland MF, Golovko D, Sutton EJ, Sennino B, Malek F, Bauer JS, McDonald DM, Daldrup-Link H. Relaxation effects of ferucarbotran-labeled mesenchymal stem cells at 1.5 T and 3 T: discrimination of viable from lysed cells. Magn Reson Med 2009; 62: 325–332.

32.   Kostura L, Kraitchman DL, Mackay AM, Pittenger MF, Bulte JW. Feridex labeling of mesenchymal stem cells inhibits chondrogen- esis but not adipogenesis or osteogenesis. NMR Biomed 2004; 17: 513–517.

33.   de Vries IJ, Lesterhuis WJ, Barentsz JO, Verdijk P, van Krieken JH, Boerman OC, Oyen WJ, Bonenkamp JJ, Boezeman JB, Adema GJ, Bulte JW, Scheenen TW, Punt CJ, Heerschap A, Figdor CG. Magnetic resonance tracking of dendritic cells in melanoma patients for monitoring of cellular therapy. Nat Biotechnol 2005; 23: 1407–1413.

34.   Toso C, Vallee JP, Morel P, Ris F, Demuylder-Mischler S, Lepetit- Coiffe M, Marangon N, Saudek F, James Shapiro AM, Bosco D, Berney T. Clinical magnetic resonance imaging of pancreatic islet grafts after iron nanoparticle labeling. Am J Transplant 2008; 8: 701–706.

35.   Zhu J, Zhou L, XingWu F. Tracking neural stem cells in patients with brain trauma. New Engl J Med 2006; 355: 2376–2378.

36.   Farrell E, Wielopolski P, Pavljasevic P, Kops N, Weinans H, Bernsen MR, van Osch GJ. Cell labelling with superparamagnetic iron oxide has no effect on chondrocyte behaviour. Osteoarthritis Cartilage 2008.

37.   Arbab AS, Bashaw LA, Miller BR, Jordan EK, Bulte JW, Frank JA. Intracytoplasmic tagging of cells with ferumoxides and transfec- tion agent for cellular magnetic resonance imaging after cell transplantation: methods and techniques. Transplantation 2003; 76: 1123–1130.

38.   Das RH, Jahr H, Verhaar JA, van der Linden JC, van Osch GJ, Weinans H. In vitro expansion affects the response of chondrocytes to mechanical stimulation. Osteoarthritis Cartilage 2008; 16: 385–391.

3

Cell quantification: evolution of compartmentalization and distribution of iron-oxide particles and labeled cells

Gyula Kotek[a], Sandra T. van Tiel[a], Piotr A. Wielopolski[a], Gavin C. Houston[b], Gabriel P. Krestin[a] and Monique R. Bernsen[a]

[a] G. Kotek, S. T. Tiel, P. A. Wielopolski, G. P. Krestin, M. R. Bernsen
Department of Radiology, Erasmus MC, Rotterdam, The Netherlands

[b] G. C. Houston
Applied Science Laboratory, General Electric Healthcare, The Netherlands

Abstract

The purpose of the study was to show the feasibility of quantification in the case of cell death, cell migration and cell division by parametric MRI. We identify limitations for quantitative cell tracking owing to mixed parallel processes. Various intravoxel SPIO-labeled cell, super paramagnetic iron oxide particles (SPIO) and micron-sized paramagnetic iron oxide (MPIO) particle distributions were prepared by methods mimicking biologically relevant processes (compartmentalization, migration, division and cell death). R_2* and R_2 relaxometry measurements were performed at 3.0 T; iron concentration was measured by optical emission spectrometry. The effects of spatial distribution and compartmentalization of paramagnetic iron-oxide particles on relativity were analyzed. Assessment of R_2' (R_2*-R_2) allowed differentiation between intracellular and extracellular SPIO only if no high-iron-content extracellular particles were present. Relaxivity was sensitive to variations in cell labelling. Samples of the same cell types embedded in the same suspension media at the same cell density produced different relaxivity values, depending on the preparation of the labeled cells. In the case of cell division, a unique relationship between relaxation rate and iron concentration was found, where the relaxivity proved to be independent of initial cell labeling. In case of cell mixing, the cell density could be derived from relaxation values, even if iron concentration was undetermined. We demonstrated that relaxometry does not allow labeled cell quantification when multiple physiological processes such as cell division and cell migration coexist. The measured transversal relaxation rates were sensitive to the labeling technique. However, under special circumstances, despite the numerous limiting factors, quantification of the number of labeled cells by relaxometry was feasible.

Keywords: iron-oxide; cell labeling; relaxometry; MRI; cell fate; iron and cell quantification

Introduction

Cell labeling with super paramagnetic iron oxide particles (SPIO) offers a promising method for in vivo human and animal model cell tracking by MRI. The low signal intensity (SI) on T_2 or T_2* weighted images reveals the presence of labeled cells (1–6). Depending on the location and the different mechanisms in tissue development, the labeled cells can be followed for as long as several weeks (7,8). Cell death, cell division, cell migration and iron re-uptake by surrounding cells or macrophages influence the detected signal intensity (9,10), and eventually may lead to misinterpretation of SI differences between labeled and nonlabeled regions. Longitudinal studies require assessment of these processes. However, detection of low-SI areas is an inadequate method.

The imaging setup parameters (such as coil and patient position), the artifacts (owing to motion and flow) and also technical imperfections (e.g. inhomogeneity in the coil sensitivity, transmit- ter and receiver decoupling problems) may compromise the reproducibility of SI values. These problems hamper quantification or reliable tracking during physiologically relevant processes.

Some studies have suggested R_2 ($1/T_2$) and R_2* ($1/T_2$*) parametric mapping to be a feasible and reproducible quantification method of SPIO or SPIO labeled cells per voxel (11–13). At sufficiently high imaging resolution, where the image distortions owing to the susceptibility inhomogeneities are negligible, the relaxation rates can be related to the imaged voxels (14,15).

Voxel-based relaxometry potentially allows assessment of iron concentration if a unique relationship can be established between relaxation rates and iron concentrations. As such, voxel-based relaxometry may establish a method of quantification for density of labeling particles and eventually for the number of labeled cells. Although many reports have demonstrated a linear (or at least monotonic) relationship between R_2* or R_2 values and iron concentration (3,16–18), there are other variables that may influence relaxation values, such as intravoxel distribution and compartmentalization of iron oxide particles (12,16,17). Additionally, the dependence of R_2* or the R_2-Fe concentration calibration curve on compartmentalization or on labeling particle size and

3

type has also been reported (16). The reliability of relaxometry measurements is further complicated by deviations from a mono exponential decay in signal intensity (11,16,19–23).

We further assume that the effects of biologically relevant variations of spatial distribution and compartmentalization of iron oxide particles may additionally affect the relationship between relaxation rates and Fe concentration. Specifically in dividing cells, both cells and intracellular SPIO content are subject to various evolution pathways. Cells may divide, sharing their SPIO content to daughter cells (24), or simply may translocate to nonlabeled regions, resulting in a mixture of labeled and nonlabeled cells. Some cells may die and disintegrate, transferring their content to the extracellular space, while may be taken up by macrophages or other surrounding cells. As these pathways may be differently represented, their effects on the SPIO compartmentalization and spatial distribution may result in different R_2 and R_2* values at the same SPIO concentration (25). Under these circumstances, relaxometry may lead to a misinterpretation of iron concentrations and hence to false conclusions on how tissue develops.

In our study, we address the effects of these evolution pathways by investigating the resulting change in transversal relaxation times. For this purpose, suspensions of labeled and unlabeled cells were used as a model to mimic cell translocation effects. We studied the effect of cell division by monitoring the evolution of labeled cells. Aggregation effects were studied by suspensions of SPIO, MPIO and SPIO-complexes. To create different spatial distribution of labeling SPIOs, we varied cell labeling and extracellular SPIO content and used different cell densities.

Materials and Methods

Cell culture and cell labeling

As a model system for dividing cells, Brown Norway 175 (BN175) sarcoma cells were used. Cells were grown in advanced RPMI medium (Invitrogen, Breda, The Netherlands) with 1% (v/v) penicillin– streptomycin (10 000 U penicillin ml^{-1} + 10 000 ug streptomycin ml^{-1}; Cambrex, Verviers, Belgium) and 10% (v/v) fetal

bovine serum (Cambrex, Verviers, Belgium) in 175 cm^2 flasks (Fisher Scientific B.V., Landsmeer, The Netherlands).

Labeling of cells with SPIO was performed at 80–90% confluence using Endorem (Guerbet S.A., Paris, France) and lipofectamine 2000 (Invitrogen, Breda, The Netherlands). A labeling stock solution of 215 ug Fe ml^{-1}, for a 175 cm^2 flask, was prepared as follows: 25 ul Endorem was added to 625 ul Opti-MEM (Invitrogen, Breda, The Netherlands) and 25 ul of lipofectamine was added to 625 ul Opti-MEM. After 5 min the two solutions were mixed together and the resulting suspension was incubated at room temperature for 20 min. After washing the cells with phosphate-buffered saline (PBS; Invitrogen, Breda, The Netherlands), the culture medium was replaced by advanced RPMI medium with 1% (v/v) penicillin–streptomycin and 233 ug (1082 ul) of iron was added to the cells, which were then incubated for 24 h at 37°C–5% CO$_2$. Before further use of labeled cells, the monolayer cultures were rinsed three times with PBS.

Phantom preparation
For the MR measurements, phantoms were prepared consisting of six 0.5 ml Eppendorf tubes as sample holders. The sample holders were placed in 3 cm diameter dishes filled with water to avoid the proximity of an air interface (Fig. 2a and b). The samples were prepared with 0.3% agar (Becton Dickinson, Alphen aan de Rijn, The Netherlands) in order to avoid sedimentation. The cells used for the samples were fixed with 4% formaldehyde (Sigma-Aldrich, Zwijndrecht, The Netherlands) for 10 min at room temperature.

Incorporation of iron, localization of iron complexes and label retention
The used agar samples were dried for 72 h at 60 ^{o}C. Subsequently they were digested in 40 ul of a 3:1 mixture of ultra-pure perchloric acid (EM Science, Gibbstown, NJ, USA) and ultrapure nitric acid (JT Baker, Deventer, The Netherlands) at 60 ^{o}C for 6 h. To the digested substance 4 ml MiliQ was added and the amount of iron was determined with a Perkin Elmer Optical Emission Optima 4300 DV Spectrometer (Perkin Elmer Instruments, Norwalk, NC, USA) at 259 nm. The experiments were performed three times with triplicate samples. To assess the presence and distribution of the iron complexes, cytospin slides were prepared from labeled cells. After the slides were dried by air the cells were fixed in absolute methanol (Sigma-Aldrich, Zwijndrecht,

the Netherlands) and Prussian blue staining (Sigma-Aldrich, Zwijndrecht, The Netherlands) was performed. The slides were covered with a cover slip and imaged with an Axiovert S100 microscope (Zeiss, Oberkochen, Germany). In order to eliminate extracellular presence of SPIO, samples for cytospin slides were taken from labeled cell stocks. After visual inspection with microscopy, stocks were further processed (washed) if extracellular SPIOs were detected or otherwise approved for sample preparation (Fig. 1).

MR imaging and post-processing
Imaging was performed on a GE Signa 3.0 T whole-body clinical scanner (General Electric Healthcare, Milwaukee, USA). For radio-frequency (RF) excitation, the built-in whole body coil was used, and signal detection was performed with receive-only custom-made single channel 5 cm surface loop coil. R_2 Relaxometry was carried out with a single-slice (coronal plane) two-dimensional (2D) spin-echo (SE) sequence at various echo times (12 echoes, echo time TE = 10–210 ms, repetition time TR = 1500 ms). The image matrix was 256 x 256, at a field-of-view (FOV) of 40 x 40 mm, with a slice thickness of 0.7 mm (resolution 0.16 x 0.16 x 0.7 mm).

For R_2^* relaxometry, a three-dimensional (3D) RF-spoiled gradient recalled echo (SPGR) sequence was used at the same resolution as the R_2 measurements (0.16 x 0.16 x 0.7 mm), with eight echoes TE = 4–25 ms, TR = 33 ms and a flip angle of 13°. Coronal (horizontal plane) images were used for evaluation.

The TE values for both measurements were chosen to sample the expected exponential decay curves for different SPIO concentrations. Signal-to-noise ratios were taken into account to provide a good fit. Imaging resolution was chosen to match in vivo protocols, where R_2 and R_2^* measurements were also matched in order to achieve a voxel based comparison with the in vitro results.

Mono-exponential curve fitting was carried out on T_2- and T_2^*-weighted images with MATLAB (Levenberg–Marquardt algorithm, the MathWorks, Natick, MA, USA). The voxel-based and selected-region-of-interest based curve fitting was performed. Figure 2(b) illustrates the quality of data and fit results for spin echo (R_2) measurements, and Fig. 2(d) for gradient echo (R_2^*) measurements. A three-parameter exponential function was used:

$$SI = a \cdot \exp(-b \cdot TE) + c$$

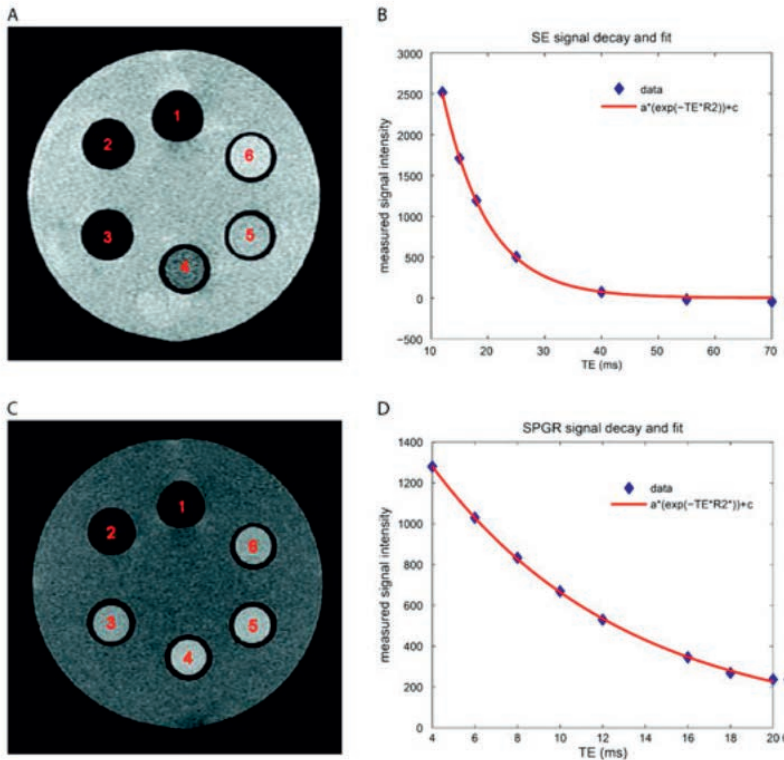where SI is the measured signal intensity and TE is echo time. The fitting parameters are a, b and c.

Figure 1 A Coronal plane image of Eppendorf tubes containing super paramagnetic iron oxide particles (SPIO)-labeled cell suspensions. Tubes are embedded in a water-agar phantom to reduce macroscopic magnetic field inhomogeneities. The image was acquired using a 2D SE sequence. Distortions are observable around sample 1. Samples exhibiting distortion also had very short T_2^* value and thus were excluded from evaluation. **B** The graph displays measured signal intensities in SE experiments (data) as a function of echo time (TE). Exponential fit is also displayed (red continuous line), illustrating curve fit accuracy and data quality. Data points were acquired from sample 3. This sample contained a mixture of SPIO-labeled and unlabeled cells (in total 3106 cells) in 0.3% agar. R_2 of the fit: $R_2 > 0.99$. **C** Coronal plane gradient echo (SPGR) image of the same sample as in (A). **D** Measured signal intensities in SPGR experiments as a function of TE are displayed. Curve fitting result is plotted (red line). R^2 of the fit: $R^2 > 0.99$.

Relaxivity values ($r_2 = dR_2/dc_{Fe}$ and $r_2^* = dR_2^*/dc_{Fe}$) were determined by linear fitting to the relaxation rate vs iron concentration (c_{Fe}) curves. Cellular relaxivity was calculated similarly from relaxation rate vs cell density plots; relative

relaxivity was calculated from relative relaxation rate vs relative extracellular iron content plots.

The R_2' relaxation rate, as a physical quantity characterizing the B_0 inhomogeneity was calculated as $R_2' = R_2^* - R_2$. Similarly, the relaxivity, characterizing the samples, was calculated as $r_2' = r_2^* - r_2$.
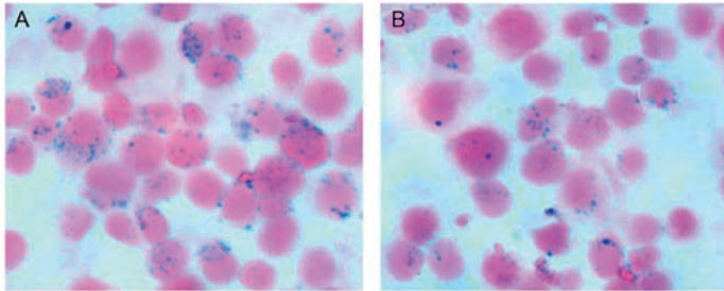

Figure 2 BN175 cells and labeling super paramagnetic iron oxide particles (SPIO) particles (image acquired at 400 x magnification), prepared for MRI measurements. The typical vesicular perinuclear distribution of SPIO can be observed as often reported following endocytosis. No excess SPIO are observable in the extracellular space. **A** Cytospin slide after labeling; **B** cytospin slide 48 h after labeling.

Distribution phantoms

1. Aggregation and compartmentalization of the labeling particles

In order to assess the effect of labeling particle aggregation, a dilution series of SPIO, SPIO–lipofectamin complexes (in the following referred to as SPIOc) and MPIO (1.1 pg iron per particle, average size 1.63 um, Bangs Laboratories Inc., Fishers, IN, USA) was prepared. Separate SPIO (33.6, 16.8, 8.4, 4.2, 2.1 and 1.05 ug iron content) and MPIO (36.9, 18.4, 9.2, 4.6, 2.3 and 1.15 ug iron content) solution series in 0.3% agar were prepared. SPIOc samples were prepared from a stock SPIO–lipofectamin complex dilution solution of 0.215 ug Fe ul^{-1}. Different amounts (7–224 ug Fe) were mixed with 200 ul 0.3% agar in a 500 ul Eppendorf tube.

To characterize the effect of compartmentalization of labeling particles, suspensions of SPIO particles and labeled cells were prepared, where the cell density was kept constant with increasing amount of SPIO in the extracellular space. An aliquot of 3×10^6 cells was suspended in 200 ul 0.3% agar with various (0–2.7 ug) SPIO contents added.

2. Cell migration: variations in labeled and unlabeled cell densities

The physical principle of cell migration was mimicked by the mixing of the suspensions of labeled and unlabeled cells. To characterize the effect of variations in the density of labeled cells, phantoms were created with a total of 3×10^6 cells in 200 ul 0.3% agar. The ratios of labeled and unlabeled cells were 1:1, 1:3, 1:7, 1:15, 1:31 and 1:63.

3. Intracellular variations: cell division and labeling efficiency

We generated sample series to assess the effect of heterogeneity, which may arise from uneven SPIO distribution to daughter cells or from variations in cell doubling times. Cells were harvested from an initially labeled stock at different time points after labeling. Cells were growing in cell culture, and their SPIO content was passed on to daughter cells; thus the level of cell labeling was subject to cell division.

After labeling the cells were replated and the next samples were taken at 24, 48 and 72 h. The pelleted cells were resuspended in 200 ul 0.3% agar (Becton Dickinson, Alphen aan de Rijn, The Netherlands) in a 500 ul Eppendorf tube (Fisher Scientific B.V., Landsmeer, The Netherlands).

To study the effect of variations in cell labeling, two different protocols (High and Low in the following) were followed to generate batches of labeled cells. The protocols were only different in the step preceding incubation for 24 h(see the protocol details in the 'Cell culture and cell labeling' section.): the added iron content was 279 ug (= 1296 ul) for the 'High' protocol or 233 ug (=1082 ul) for the 'Low' protocol. Both batches were used independently in the cell dilution series (mixing labeled and unlabeled cells) and in the cell division series.

Results

Free and incorporated labeling particles

The relaxivity showed a strong dependence on the type of the labeling particles. MPIOs exhibited the highest relaxivity $r_2^*= 635$ mM^{-1} s^{-1}, followed by SPIOc $r_2^*= 226$ mM^{-1} s^{-1} and SPIO particles $r_2^* = 170$ mM^{-1} s^{-1}. Compared
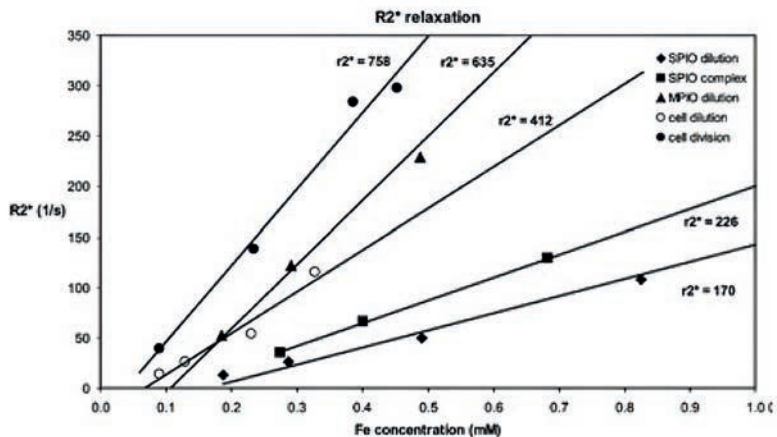
Figure 3 R_2* relaxation rate (1/s) plotted against iron concentration cFe (mM). Linear fit on data is shown. Relaxivity values (slope of linear fitted curve) are shown next to linear fits (in units: mM^{-1} s^{-1}). Free super paramagnetic iron oxide particles (SPIO), SPIO complex (SPIOc) and MPIO dilution series exhibit different relaxivities (r_2*); r_2* is higher for particles of higher Fe content. Cells labeled with SPIOc exhibit higher r_2* than SPIOc dilutions. Cell division series (initially labeled and harvested at increasing delay times) and cell dilution series (mixture of labeled and unlabeled cells) exhibit different r_2*. Cell density is identical for all cell-containing samples.
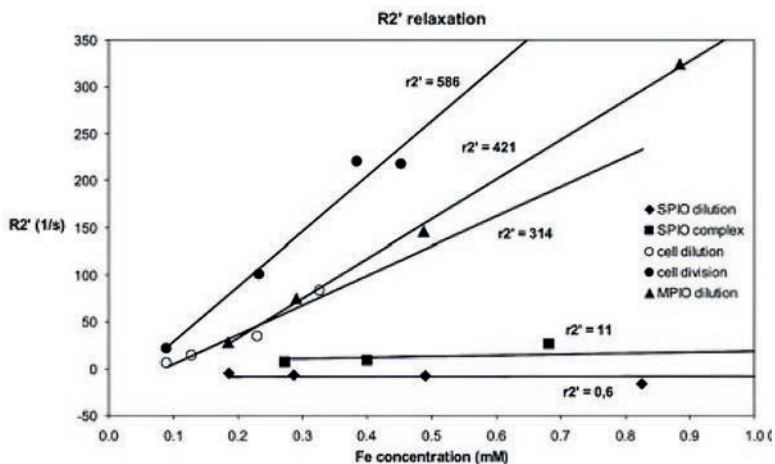
Figure 4 R_2' relaxation rate (1/s) plotted against iron concentration cFe (mM). Relaxivity values are shown next to linear fits (in units: mM^{-1} s^{-1}). Preparation of samples is identical to that in Fig. 3. R_2' differentiates between intra- and extracellular super paramagnetic iron oxide particles (SPIO). r_2' ≈ 0 for free SPIO and SPIOc. MPIO and cell dilutions have very close r_2' values. For cell division and cell dilution samples, r_2' values are different.
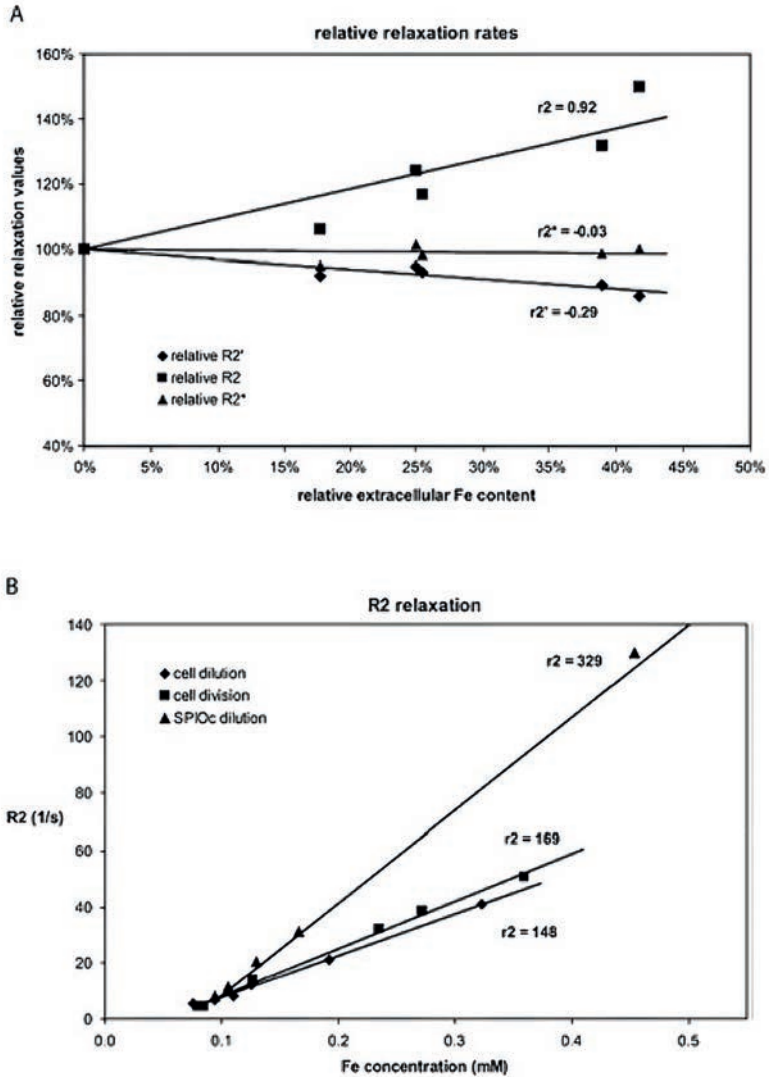
Figure 5 A Relative relaxation rates R_2, R_2^* and R_2' (relaxation values normalized by relaxation value of the sample with no extracellular super paramagnetic iron oxide particles, SPIO) are plotted against relative extracellular iron content (percentage of the total SPIO content that is in the extracellular space). The samples have identical intracellular iron content, extracellular SPIO is evenly distributed and the cell number is kept constant throughout all samples. Relative relaxivities are displayed (slope of linear fit). **B** R_2 relaxation rate plotted against iron concentration for SPIOc dilution, cell dilution and cell division samples. The SPIO complexes have lower r_2 relaxivity when incorporated in the cells.

with the free suspensions, SPIOc particles exhibited dramatically increased relaxivity when incorporated into cells: $r_2^* = 412$ mM^{-1} s^{-1} for the cell dilution series and $r_2^* = 758$ mM^{-1} s^{-1} for the cell division series (Fig. 3).

Figure 4 shows the R_2' relaxation rates for the different samples. Free SPIO and SPIOc dilutions exhibited zero r_2' relaxivity. SPIOc particles incorporated in cells and MPIO particles yielded nonzero r_2' relaxivity. The cell dilution and the MPIO dilution series resulted in very close R_2' values when Fe concentrations were in the same range (0.1–0.3 mM, see fitted linear curves, Fig. 4). The estimated values of the iron content per particle for the MPIOs and for the labeled cells in cell dilution series were 1.1 and 1.4 pg respectively (based on optical emission spectrometry for labeled cells and manufacturer data for MPIO particles). Figure 5(a) depicts the relative changes in the R_2, R_2^* and R_2' values, where the density of labeled cells was kept constant with increasing concentration of extracellular SPIO complex. For the coexistence of extracellular and intracellular SPIO, the relative change in R_2^* value with increasing amount of extracellular SPIO was negligible. Although the total iron content was almost doubled at a fixed number of labeled cells, R_2^* remained constant within error. In contrast, R_2 value showed sensitivity to total iron content (relative relaxivity was 0.92). R_2' was less sensitive to the change in the extracellular SPIO concentration (relative relaxivity was - 0.29); it decreased with increasing extracellular iron content. Figure 5(b) shows the R_2 relaxation rate dependence on iron concentration for three different compartmentalization models: dilution series of free SPIO complexes; dilution series of cells labeled with SPIO; and cell division series with SPIO labeled cells. The r_2 relaxivity was enhanced for free SPIO complexes ($r_2 = 329$ mM^{-1} s^{-1}) compared with incorporated SPIO complexes ($r_2 = 169$ mM^{-1} s^{-1} for cell division and $r_2 = 148$ mM^{-1} s^{-1} for cell dilution).

Distribution of intracellular SPIO complexes
The R_2^* and R_2' values at the same iron concentrations (also the r_2^* and r_2' values) were different for the cell dilution and for the cell division series (see Figs 3 and 4.). Although the cell types, the labeling particles and the cell densities were identical for these series, the relaxivities were clearly different (r_2^*, 758 vs 412 mM^{-1} s^{-1}; r_2', 586 vs 314 mM^{-1} s^{-1}).
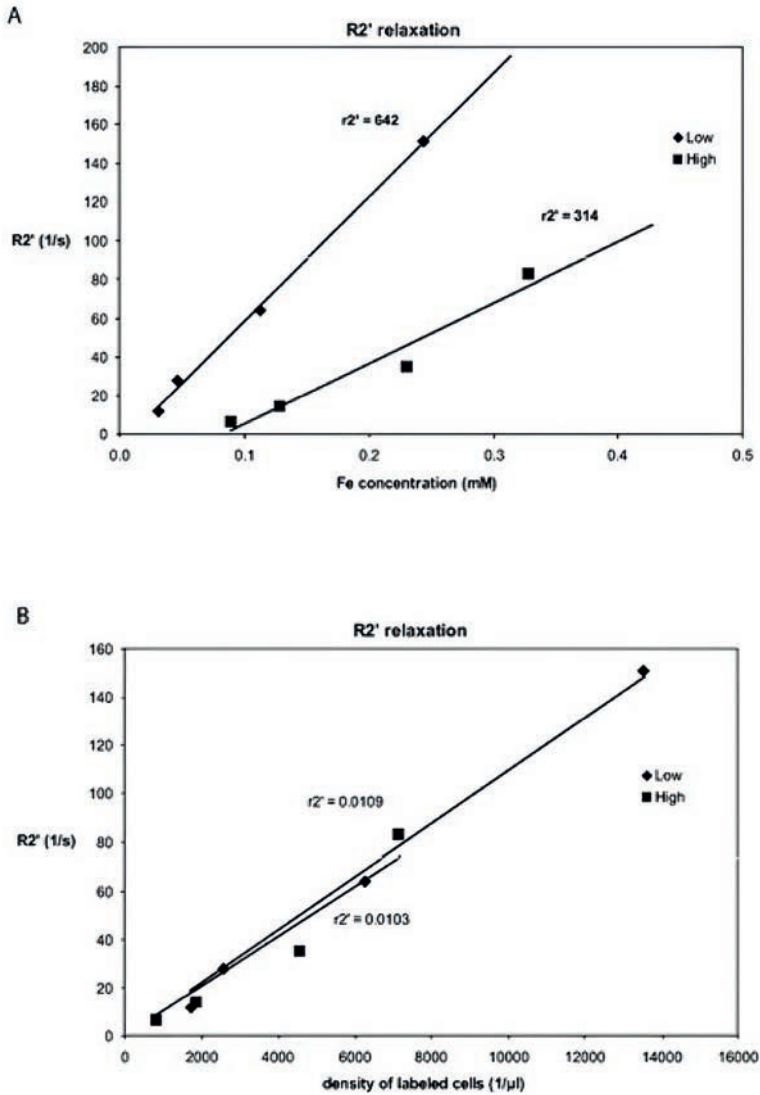
Figure 6 A R_2' relaxation rate plotted against iron concentration. The linear fit is displayed for both sample series; relaxivities are displayed next to linear fits (in mM^{-1} s^{-1} units). In sample 'low' the average cell iron content is 1.0 pg. In sample 'high' the average cell iron content is 1.4 pg. The r_2' relaxivity is more than double for sample series 'low': 642 mM^{-1} s^{-1} compared with 314 mM^{-1} s^{-1}. **B** The R_2' relaxation rate plotted against labeled cell density. The cellular relaxivity values are very close 0.01091 l/s for the labeled series 'high' and 0.01031 l/s for the 'low' series.
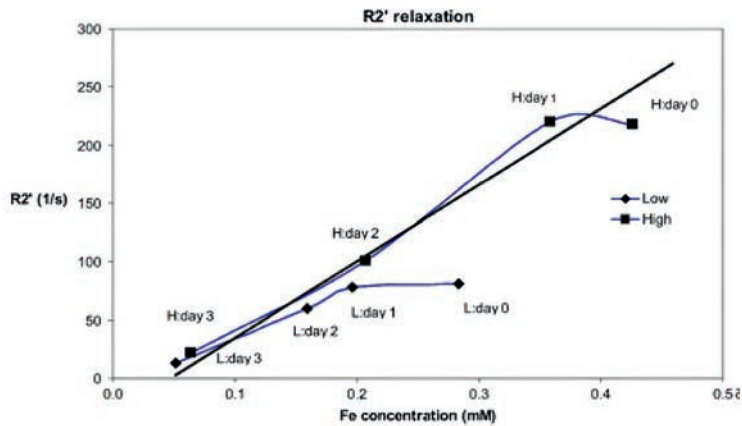
Figure 7 R_2' relaxation rate plotted against iron concentration. The linear fit on all data points excluding the day 0 data points is displayed. Data points belonging to one cell division series are connected. Data points are labeled, referring to data series (high, H; low, L) and the day of harvesting after labeling (days 0, 1, 2 and 3). After one day (approximately one cell cycle), all data points converged to the same relaxation curve (linear fit). Deviation from this relaxation curve on day 0 was apparent and proved to be systematic.

The different labeling protocols (High and Low) resulted in different estimated values of average iron content per cell (based on optical emission spectrometry). The High labeling protocol resulted in 1.4 pg per cell iron content; the Low yielded 1.0 pg per cell. The cell dilution series of these batches resulted in different r_2' relaxivities (Fig. 6a). The relaxivity was more than double ($r_2' = 642$ mM^{-1} s^{-1}) in the case of the Low labeling protocol compared with the one of the High protocol ($r_2' = 314$ mM^{-1} s^{-1}). Figure 6b exhibits R_2' relaxation rates as a function of labeled cell density. Despite the large difference in the average iron content per cell (High and Low labeling protocols), relaxation values at the same cell densities were very close, the cellular relaxivities being $r_2' = 10.9 \times 10^{-3}$ ul s^{-1} for the Low series and $r_2' = 10.3 \times 10^{-3}$ ul s^{-1} for the high series.

A comparison between labeled cell division series, where the labeling protocol was different, is depicted in Fig. 7. The series exhibit very close R_2' relaxation rates in a wide range of iron concentrations after one division cycle. In the case of the cell division series, R_2' showed no sensitivity to the differences in initial cell labeling. Both division series converged to the same linear curve established by linear fit to the data points. The deviation from the relaxation vs iron concentration curve at day 0 appeared in both batches.

Discussion

Mono-exponential signal decay

Several theoretical works and experimental studies (20–23) report deviation from mono-exponential signal decay in the presence of magnetic particles. In the case of SPIO labeled cells, a very fast initial signal decay followed by a slower decay was expected, where the components originated from the extra- and the intracellular compartments (21). Furthermore, Jensen et al. (26) predict nonexponential behavior of the signal decay, where the deviation from exponential depends on the MR acquisition scheme, diffusion and the shape of magnetic disturbers.

However, these predictions were not observed in our measurements. We found good agreement with mono-exponential signal decay in every investigated sample. This can be explained in part by the relatively large value of the minimum echo times (10 ms in spin-echo, 4 ms in gradient echo experiments), that prohibit the observation of the fast initial signal decay.

Theoretical considerations

The theoretical works of Brown (27) and Yablonskiy and Haacke (28) describe relaxation rates in the presence of magnetic inhomogeneities. These models are valid under certain assumptions, most importantly the static dephasing and dilute disturbers regimes (hereafter SD). From the model it follows that the relaxation rate is proportional to the local magnetization dose (LMD), the product of the volume fraction of the magnetic compartments, f (in our case, SPIO labeled cells) and the internal magnetization of these compartments, M:

$$R_2' = \gamma \frac{2\pi}{9\sqrt{3}} \cdot f \cdot M \qquad (1)$$

With one further assumption, that the internal magnetization of the labeled cells (M) is proportional to the number of incorporated SPIOs, this predicts the following: rearrangement of SPIO particles between cells leaves R_2' unchanged, if cell number (NL), total number of SPIOs and total volume (V) are constant.

$$LMD = f \cdot M = \frac{v \cdot N_L}{V} \cdot \frac{n \cdot \mu}{v} = \frac{\mu}{m_0} \cdot \frac{n \cdot N_L \cdot m_0}{V} = \frac{\mu}{m_0} \cdot c_{Fe} \qquad (2)$$

where v is the cell volume, n is the number of SPIOs in a cell, m is the magnetic moment of an SPIO, m_0 is the mass of iron per SPIO particle and c_{Fe} is the iron concentration in the sample. Any spatial rearrangement of SPIO leaves the iron concentration constant, and also 'R_2' if SD is valid.

The difference between cell dilution and cell division sample at a given SPIO concentration (Fig. 4) can be viewed as a simple rearrangement of SPIOs in labeled cells: in the cell dilution samples the SPIOs are concentrated in fewer cells. Also the 'High' labeled sample has fewer cells with higher load compared with the 'Low' labeled sample at an equal amount of SPIO particles (Fig. 6a). These rearrangements of labeling particles lead to different R_2' values and r_2' relaxivities. SD theory fails to describe this behavior. The following explains this result: SD increasingly underestimates R_2' at higher volume fractions of labeled cells (16,20,29). A rough estimate of the volume fraction range of the magnetic disturbers is 0.3–5% in our cell suspension samples. With the assumption of even distribution of SPIOs to daughter cells, the cell division samples represent a higher volume fraction of magnetic disturbers (here: labeled cells) compared with cell dilution samples; therefore the elevation of R_2' values from SD prediction is higher. Similar to this, the 'Low' labeled samples have higher volume fractions compared with 'High' labeled samples at the same SPIO content, resulting in higher elevation of R_2' values.

The SPIO and cell dilution samples exhibit minor deviation from the linear relaxivity–concentration curve (Fig. 3): the relaxivities decrease at lower concentrations. Also, an extrapolation to lower concentration from the data points leads to negative relaxation rates at zero iron concentration. Based on our results and the SD theory, one can predict that the different samples exhibit the same relaxivity when dilute; this relaxivity value is described by the SD theory. With increasing concentrations (as the theoretical prediction underestimates the relaxivity values), the relaxation rates of the samples deviate from the mutual, theoretically predicted value and exhibit higher relaxivity. As our results demonstrate, this relaxivity is dependent on spatial distribution of SPIOs.

Another possible explanation of the differences in relaxivities (Fig. 4) may be that the magnetization of the labeled cells is not proportional to the number of incorporated SPIOs (a hypothesized saturation effect). In this case, the samples where SPIOs are concentrated in fewer cells would lead to lower cellular magnetization and LMD value, and thus lower R_2', according to SD model. However, this hypothesis would contradict the previous findings reported by Bowen et al. [(16), table 3], where the LMD and iron content of SPIO labeled cells were found proportional.

According to SD theory predictions, the relaxation rate is proportional to the internal magnetization of the magnetic disturbers relative to the magnetization of the surrounding medium $R_2' \approx (M - M_0)$. The R_2' values of the labeled cell suspensions are reduced by the presence of SPIOs in the suspension medium. This prediction is in good agreement with our findings (Fig. 5a). Irrespective to the validity of SD, it can be assumed that R_2' is a monotonic function of $M - M_0$.

The behavior of R_2' relaxation illustrated in Fig. 6(a and b) is surprising, especially in comparison with the SD predictions. SD regime assumption with the further assumption that the intracellular magnetization is proportional to the SPIO content per cell predicts that R_2' is determined by the iron concentration. The findings illustrated by Fig. 6 contradict this prediction. It can be hypothesized that at increasing volume fraction of the magnetic disturbers (moving away from the dilute SD regime), the cellular magnetization plays a lesser role and the number of disturbers (volume fraction) becomes more important.

Extra-cellular/intra-cellular differentiation
Numerous studies have suggested that the r_2* and r_2 relaxivities depend on compartmentalization of iron particles. The r_2' relaxivity is negligible for free, equally distributed SPIO. As was previously suggested (12), R_2' values can be used to determine labeled cell number per voxel. R_2' is a valid measure of the number of labeled cells, assuming a simple scenario for cell death, where SPIO is transferred from the intracellular space to the extracellular space and evenly distributed. Our results confirm this assumption. However, they also suggest that extracellular iron may give a nonzero contribution to R_2'. In case of extreme iron deposits (see MPIO on Fig. 3), extracellular iron produces

relaxivity values close to the relaxivity of samples with labeled cells. When the highly aggregated extracellular iron coexist with the labeled cells in the imaging voxels, the R_2' based cell quantification method fails.

Cell death

Large clusters of EC SPIO may also be produced during cell death. When dead cells do not disintegrate entirely, or the EC matrix prevents even distribution of released labeling particles (e.g. in the presence of a collagen matrix), particles of high iron content may be present in the EC space. Consequently R_2' will not indicate changes in cell viability (30).

In the case of the aforementioned simplistic scenario (where dead cells spread their contents to EC evenly), though, theoretically, one can find an indication of cell death: the R_2' value will decrease (owing to decreasing concentration of labeled cells, see Fig. 4, and owing to increasing concentration of extracellular iron, see Fig. 5a). On the other hand, R_2 will increase if SPIO is transferred from the intracellular to the extracellular space (12). Figure 5(b) shows that the relaxivity for free SPIO is higher than that for SPIO incorporated in cells. Furthermore, R_2 is sensitive to solute concentration, and the IC space is usually more concentrated. R_2 will increase if cell content is transferred from the IC to the EC space (31–33). Therefore, the decrease in the R_2' value and the simultaneous increase in the R2 value may well indicate on- going cell death in the labeled cell region.

Cell migration/mixing

Translocation of cells potentially leads to a mix of labeled and unlabeled cells. R_2' and R_2^* prove to be reliable measures. Both show a linear dependence on iron concentration. If it is assumed that there is no other source for iron deposits resulting from other sources, e.g. from red blood cells, it is possible to quantify the number of labeled cells. However, a careful calibration is necessary. As Fig. 6(a) indicates, the variations in iron content per cell can lead to different relaxivities. The iron concentration cannot be determined unambiguously by relaxometry. However, with a priori knowledge of the iron content per cell the cell density can be derived from the R_2' relaxation rate (see Fig. 6b).

Cell division

The problem with quantifying the number of labeled cells in the case of cell division (passing SPIO content to daughter cells) was indicated in previous studies (24). Even in a simplified model of a cluster of dividing labeled cells, where cell density is kept constant, increasing heterogeneity is expected. Variations in cell doubling time and uneven distribution of SPIO to daughter cells lead to inhomogeneities in the spatial distribution of SPIOs. However, our results on cell division samples reveal a unique curve of the relaxation rate vs iron concentration (Fig. 7). Despite the differences in the initial iron content per cell, the samples could be characterized by the same relaxivity. We can conclude that in a volume where the cells are labeled and dividing, and also the cell density is constant (e.g. constant intracellular volume ratio and cell size can be assumed), the iron content can be determined. This iron content may serve as a basis for estimation of the number of labeled cells in the corresponding volume.

Mixed processes

Cell death, cell migration (or translocation), cell division, extracellular SPIO accumulation or dispersion can be modelled in vitro and a calibration on relaxivity can be established. We have demonstrated here that mixing, division and cellular load variations can exhibit different relaxivities. Unless there is only one, well-defined process going on in the volume of interest, neither the iron concentration nor the density of labeled cells can be determined by relaxation rate measurements only. Based on theoretical grounds, this finding would make cell quantification impossible for many in vivo situations. However, one can argue that, at sufficiently high imaging resolution, the coexistence of the different pathways in a single voxel is not probable. This biologically homogeneous compartment size could be determined for the investigated tissue type and assumed physiological processes, thus the imaging resolution could be chosen correspondingly. In this scenario, with the further assumption that the processes can be identified on a voxel level, we can conclude that iron quantification can be carried out by relaxometry.

Conclusion

Our results suggest that in vitro relaxivity calibrations can be applied to in vivo measurements only under special circumstances. We can conclude that the cell-to-cell variations play an important role in transversal relaxation rates. We demonstrated that samples of labeled cells of the same type at the same cell density at a given iron concentration can exhibit different R_2^* and R_2' relaxation rates, depending on the cell-to-cell variations in the labeling particle content. Unless there is only one, well-defined, dominant process in the investigated volume, iron content cannot be determined by relaxation measurement. During cell mixing, cell densities can be derived from relaxation values, even if iron concentration remains ambiguous. When cell division is the dominant process, despite labeling variations, iron content and also cell densities can be determined from re- laxation rates. Cell death can be identified by the simultaneous increase in R_2 and decrease in R_2'.

Acknowledgement

References

1. Long CM, van Laarhoven HW, Bulte JW, Levitsky HI. Magnetovaccination as a novel method to assess and quantify dendritic cell tumor antigen capture and delivery to lymph nodes. Cancer Res 2009; 69: 3180–3187.

2. Hauger O, Frost EE, van Heeswijk R, Deminiere C, Xue R, Delmas Y, Combe C, Moonen CT, Grenier N, Bulte JW. MR evaluation of the glo- merular homing of magnetically labeled mesenchymal stem cells in a rat model of nephropathy. Radiology 2006; 238: 200–210.

3. Bos C, Delmas Y, Desmouliere A, Solanilla A, Hauger O, Grosset C, Dubus I, Ivanovic Z, Rosenbaum J, Charbord P, Combe C, Bulte JW, Moonen CT, Ripoche J, Grenier N. In vivo MR imaging of intravascu- larly injected magnetically labeled mesenchymal stem cells in rat kidney and liver. Radiology 2004; 233: 781–789.

4. Flexman JA, Cross DJ, Tran LN, Sasaki T, Kim Y, Minoshima S. Quanti- tative analysis of neural stem cell migration and tracer clearance in the rat brain by MRI. Mol Imag Biol 2011; 13(1): 104–111.

5. Farrell E, Wielopolski P, Pavljasevic P, van Tiel S, Jahr H, Verhaar J, Weinans H, Krestin G, O'Brien FJ, van Osch G, Bernsen M. Effects of iron oxide incorporation for long term cell tracking on MSC differen- tiation in vitro and in vivo. Biochem Biophys Res Commun 2008; 369: 1076–1081.

6. Zhang Z, van den Bos EJ, Wielopolski PA, de Jong-Popijus M, Bernsen MR, Duncker DJ, Krestin GP. In vitro imaging of single living human umbilical vein endothelial cells with a clinical 3.0-T MRI scanner. MAGMA 2005; 18: 175–185.

7. de Vries IJ, Lesterhuis WJ, Barentsz JO, Verdijk P, van Krieken JH, Boerman OC, Oyen WJ, Bonenkamp JJ, Boezeman JB, Adema GJ, Bulte JW, Scheenen TW, Punt CJ, Heerschap A, Figdor CG. Magnetic resonance tracking of dendritic cells in melanoma patients for mon- itoring of cellular therapy. Nat Biotechnol 2005; 23: 1407–1413.

8. Himes N, Min JY, Lee R, Brown C, Shea J, Huang X, Xiao YF, Morgan JP, Burstein D, Oettgen P. In vivo MRI of embryonic stem cells in a mouse model of myocardial infarction. Magn Reson Med 2004; 52: 1214–1219.

9. Terrovitis J, Stuber M, Youssef A, Preece S, Leppo M, Kizana E, Schar M, Gerstenblith G, Weiss RG, Marban E, Abraham MR. Magnetic reso- nance imaging overestimates ferumoxide-labeled stem cell survival after transplantation in the heart. Circulation 2008; 117: 1555–1562.

10. Pawelczyk E, Arbab AS, Chaudhry A, Balakumaran A, Robey PG, Frank JA. In vitro model of bromodeoxyuridine or iron oxide nanoparticle uptake by activated macrophages from labeled stem cells: implica- tions for cellular therapy. Stem Cells 2008; 26: 1366–1375.

11. Boutry S, Forge D, Burtea C, Mahieu I, Murariu O, Laurent S, Vander Elst L, Muller RN. How to quantify iron in an aqueous or biological matrix: a technical note. Contrast Media Mol Imag 2009; 4: 299–304.

12. Kuhlpeter R, Dahnke H, Matuszewski L, Persigehl T, von Wallbrunn A, Allkemper T, Heindel WL, Schaeffter T, Bremer C. R_2 and R_2^* mapping for sensing cell-bound superparamagnetic nanoparticles: in vitro and murine in vivo testing. Radiology 2007; 245: 449–457.

13. Peldschus K, Schultze A, Nollau P, Kaul M, Schumacher U, Wagener C, Adam G, Ittrich H. Quantitative MR imaging of targeted SPIO parti- cles on the cell surface and comparison to flow cytometry. Magn Reson Imag 2010; 28(4): 599–606.

14. Young IR, Cox IJ, Bryant DJ, Bydder GM. The benefits of increasing spatial resolution as a means of reducing artifacts due to field inho- mogeneities. Magn Reson Imag 1988; 6: 585–590.

15. Frahm J, Merboldt KD, Hanicke W. Direct FLASH MR imaging of mag- netic field inhomogeneities by gradient compensation. Magn Reson Med 1988; 6: 474–480.

16. Bowen CV, Zhang X, Saab G, Gareau PJ, Rutt BK. Application of the static dephasing regime theory to superparamagnetic iron-oxide loaded cells. Magn Reson Med 2002; 48: 52–61.

17. Rad AM, Arbab AS, Iskander AS, Jiang Q, Soltanian-Zadeh H. Quanti- fication of superparamagnetic iron oxide (SPIO)-labeled cells using MRI. J Magn Reson Imag 2007; 26: 366–374.

18. Politi LS, Bacigaluppi M, Brambilla E, Cadioli M, Falini A, Comi G, Scotti G, Martino G, Pluchino S. Magnetic-resonance-based tracking and quantification of intravenously injected neural stem cell accumulation in the brains of mice with experimental multiple sclerosis. Stem Cells 2007; 25: 2583–2592.

19.	Cheng YC, Haacke EM, Yu YJ. An exact form for the magnetic field density of states for a dipole. Magn Reson Imag 2001; 19: 1017–1023.

20.	Muller RN, Gillis P, Moiny F, Roch A. Transverse relaxivity of particu- late MRI contrast media: from theories to experiments. Magn Reson Med 1991; 22: 178–182;discussion 195–176.

21.	Bulte JW, Miller GF, Vymazal J, Brooks RA, Frank JA. Hepatic hemosi- derosis in non-human primates: quantification of liver iron using dif- ferent field strengths. Magn Reson Med 1997; 37: 530–536.

22.	Gossuin Y, Gillis P, Muller RN, Hocq A. Relaxation by clustered ferritin: a model for ferritin-induced relaxation in vivo. NMR Biomed 2007; 20: 749–756.

23.	St Pierre TG, Clark PR, Chua-Anusorn W. Single spin-echo proton trans- verse relaxometry of iron-loaded liver. NMR Biomed 2004; 17: 446–458.

24.	Walczak P, Kedziorek DA, Gilad AA, Barnett BP, Bulte JW. Applicability and limitations of MR tracking of neural stem cells with asymmetric cell division and rapid turnover: the case of the shiverer dysmyeli- nated mouse brain. Magn Reson Med 2007; 58: 261–269.

25.	Liu W, Frank JA. Detection and quantification of magnetically labeled cells by cellular MRI. Eur J Radiol 2009; 70: 258–264.

26.	Jensen JH, Chandra R. Strong field behavior of the NMR signal from mag- netically heterogeneous tissues. Magn Reson Med 2000; 43: 226–236.

27.	Brown R. Distribution of fields from randomly placed dipoles: free precession signal-decay as result of magnetic grains. Phys Rev 1961; 121: 1379–1382.

28.	Yablonskiy DA, Haacke EM. Theory of NMR signal behavior in mag- netically inhomogeneous tissues: the static dephasing regime. Magn Reson Med 1994; 32: 749–763.

29.	Brooks RA, Moiny F, Gillis P. On T2-shortening by weakly magnetized particles: the chemical exchange model. Magn Reson Med 2001; 45: 1014–1020.

30.	Winter EM, Hogers B, van der Graaf LM, Gittenberger-de Groot AC, Poelmann RE, van der Weerd L. Cell tracking using iron oxide fails to distinguish dead from living transplanted cells in the infarcted heart. Magn Reson Med 2010; 63(3): 817–821.

31.	Kotek G, Berente Z, Schwarcz A, Vajda Z, Hadjiev J, Horvath I, Repa I, Miseta A, Bogner P. Effects of intra- and extracellular space proper- ties on diffusion and T(2) relaxation in a tissue model. Magn Reson Imag 2009; 27: 279–284.

32.	Calamante F, Lythgoe MF, Pell GS, Thomas DL, King MD, Busza AL, Sotak CH, Williams SR, Ordidge RJ, Gadian DG. Early changes in water diffusion, perfusion, T1, and T2 during focal cerebral ischemia in the rat studied at 8.5 T. Magn Reson Med 1999; 41: 479–485.

33.	Van Dorsten FA, Olah L, Schwindt W, Grune M, Uhlenkuken U, Pillekamp F, Hossmann KA, Hoehn M. Dynamic changes of ADC, per- fusion, and NMR relaxation parameters in transient focal ischemia of rat brain. Magn Reson Med 2002; 47: 97–104.

4

SPIO labeling of endothelial cells using ultrasound and targeted microbubbles at diagnostic pressures

Ilya Skachkov[1], Ying Luan[1], Sandra T. van Tiel[2], Antonius F. W. van der Steen[1,3], Nico de Jong[1,3], Monique R. Bernsen[2¶], Klazina Kooiman[1¶]

[1] Department of Biomedical Engineering, Thoraxcenter, Erasmus MC, Rotterdam, the Netherlands

[2] Department of Radiology & Nuclear Medicine, Erasmus MC, Rotterdam, the Netherlands

[3] Laboratory of Acoustical Wavefield Imaging, Faculty of Applied Sciences, Delft University of Technology, Delft, the Netherlands

¶ These authors contributed equally to this work.

Abstract

In vivo cell tracking of therapeutic, tumor, and endothelial cells is an emerging field and a promising technique for imaging cardiovascular disease and cancer development. Site-specific labeling of endothelial cells with the MRI contrast agent superparamagnetic iron oxide (SPIO) in the absence of toxic agents is challenging. Therefore, the aim of this *in vitro* study was to find optimal parameters for efficient and safe SPIO-labeling of endothelial cells using ultrasound-activated CD31-targeted microbubbles for future MRI tracking. Ultrasound at a frequency of 1 MHz (10,000 cycles, repetition rate of 20 Hz) was used for varying applied peak negative pressures (10 – 160 kPa, i.e. low mechanical index (MI) of 0.01 – 0.16), treatment durations (0 – 30 s), time of SPIO addition (-5 min – 15 min with respect to the start of the ultrasound), and incubation time after SPIO addition (5 min – 3 h). Iron specific Prussian Blue staining in combination with calcein-AM based cell viability assays were applied to define the most efficient and safe conditions for SPIO-labeling. Optimal SPIO labeling was observed when the ultrasound parameters were 40 kPa peak negative pressure (MI 0.04), applied for 30 s just before SPIO addition (0 min). Compared to the control, this resulted in an approximate 12 times increase of SPIO uptake in endothelial cells *in vitro* with 85% cell viability. Therefore, ultrasound-activated targeted ultrasound contrast agents show great potential for effective and safe labeling of endothelial cells with SPIO.

Introduction

In vivo cell tracking is a very promising technique to visualize cells of interest inside the body. It allows tracking of motile therapeutic cells like immune cells, stem cells, and endothelial progenitor cells to sites of inflammation, cancer, or ischemia [1-5]. Additionally, this technique can be used to track tumor cells [6], tumor vasculature [7, 8], or endothelial cells in tissue engineered valves [9] and vascular grafts [10].

After labeling the cells of interest with an imaging probe, they can be tracked by an imaging modality. Magnetic resonance imaging (MRI) is interesting for cell tracking because it is precise, harmless, and thus well suited for longitudinal studies. Moreover, single cell tracking is possible by MRI. However, *in vivo* cell labeling with an MRI contrast agent is challenging [6, 11-16]. For cell labeling, the T2 and T2*-shortening MRI contrast agent superparamagnetic iron oxide nanoparticles (SPIO) of 80–180 nm in size [17] are often used [18, 19]. They are relatively safe compounds [19-22], but most of *in vitro* cell labeling techniques for SPIO are not applicable *in vivo,* because of the high toxicity and broad systemic effects of transfection agents [23]. Therefore, there has been growing interest in safe, site-specific cell labeling techniques. One potential method involves using ultrasound contrast agent, which are comprised of microbubbles. The microbubbles have a low diffusible gas core (for example C_4F_{10}), vary in diameter from 1–10 μm, and are encapsulated by a coating material (for example phospholipids). When ultrasound is applied, the microbubbles oscillate due to sequential compression and expansion caused by pressure variations in the surrounding medium. The oscillation of microbubbles has been shown to deliver therapeutic materials into cells and interstitial tissue [24-27]. Up till now there is no consensus on the mechanism of the enhanced uptake. One of the uptake routes is a phenomenon called sonoporation, when reversible or non-reversible cell membrane pores are generated upon microbubble oscillations or violent collapse. Other uptake routes include enhanced endocytosis and opening of cell-cell contacts [25, 26, 28]. It has been reported that the efficacy of cellular uptake of therapeutic agents can be improved up to 7.7-fold *in vitro* [29] and up to fivefold *in vivo* [30] by using targeted microbubbles (tMB) instead of non-targeted microbubbles (non-

4

tMB). The tMB have a ligand added in their coating by which the tMB can adhere to disease-specific cell membrane biomarkers [31, 32].

It was previously shown that 45–60 nm SPIO (Resovist) could be delivered *in vivo* into the swine brain using SonoVue lipid-coated non-tMB and ultrasound (28-kHz ultrasound with 100-ms burst length and repetition rate of 1 Hz at 0.6 – 1 MPa (mechanical index (MI) 4.8 – 6.0) applied for 5 min; MRI performed 3 h after treatment) [33]). Brain tumor delivery of SPIO (mean diameter 6 – 10 nm [34] or 35.7 ± 9.2 nm [35]) loaded in the lipid-coating of in-house produced non-tMB was shown *in vivo* in rats using ultrasound (0.4 MHz with 1,000 cycles and repetition rate of 1 Hz at 325 kPa (MI 0.5) applied for 90 s; MRI performed 40 min after treatment [34] or 1 MHz with 5,000 cycles and repetition rate of 1 Hz at 300 kPa (MI 0.3) applied for 4 min; MRI performed 1 and 3 h after treatment [35]). Delivery of 120 – 180 nm SPIO (Feridex) was also shown in the aortic arch by SonoVue and ultrasound treatment (8.5 MHz ultrasound at an MI of 1.2 applied for 20 min; MRI performed 1 h after treatment) [36]. These studies demonstrate the possibility of SPIO-loaded MB or co-administrated SPIO with MB for labeling extravascular tissues and subsequent MRI imaging of the SPIO, but do not cover cell labeling. Successful SPIO (Revovist) mesenchymal stem cell labeling using SonoVue and ultrasound (1 MHz, 50% duty cycle, 1.0 W/cm^2 acoustic power applied for 60 s) has been reported *in vitro* [37]. SPIO (12 nm mean diameter) loaded in the polymer coating of in-house produced non-tMB were used to successfully label tumor cells *in vitro* using ultrasound (1 MHz, 20 cycles per burst, repetition rate of 10 kHz, 0.1 – 0.75 W/cm^2 acoustic power applied for 40 s) [38]. However, MB are blood pool agents. Endothelial cells, which form the inner lining of vessels, are therefore the main target of intravascular administered MB [39, 40]. Exceptions are tumors that invade into the vasculature, as reported for hepatocellular cancer (i.e. a primary liver tumor) [41] and colorectal cancer [42]. On the other hand, tMB were shown to target ovarian cancer cells preclinically by an alternative administration route, namely intraperitoneal injection [43]. Additionally, tMB are preferable instead of non-tMB since they can be specifically targeted to the cells of interest and upon binding are close to the endothelium, which is a perquisite for the MB-mediated drug delivery effectiveness [26]. The *in vivo* study by Gao et al. demonstrated arterial wall uptake of SPIO particles using non-tMB and ultrasound [36], but only under one acoustic setting (8.5 MHz ultrasound at

1.2 MI, i.e. 3.5 MPa acoustic pressure), which induced considerable arterial wall damage. To the best of our knowledge, no in-depth studies have been performed to characterize the parameters (e.g., the acoustic settings, the SPIO addition time and incubation time) that strongly influence the efficacy and safety of SPIO-labeling of endothelial cells using tMB at low MI (<0.2).

The aim of our *in vitro* study was to find optimal parameters for non-invasive, tMB-mediated, SPIO-labeling of endothelial cells for the future application of MRI tracking of tumor vasculature and tissue engineered vasculature structures. We used lipid-coated tMB targeted against CD31 (i.e. platelet/endothelial cell adhesion molecule-1 (PECAM1)), a biomarker constitutively expressed on endothelial cell membranes [44], as proof of concept. Iron specific Prussian Blue staining in combination with calcein-AM based cell viability assays were applied to define the most efficient and safe conditions for SPIO-labeling of endothelial cells *in vitro*. We investigated a fixed ultrasound driving frequency of 1 MHz and a series of low diagnostic acoustical pressures (<200 kPa; MI<0.2) and treatment duration times (0 – 30 s). In our study we used 1 MHz as the ultrasound frequency because it is commonly used for microbubble-mediated drug delivery studies and is close to the resonance frequency of microbubbles [26]. Although the exact link between the type of microbubble behavior and drug uptake is not yet known [26], it was reported that endocytosis was stimulated at longer (2,000 – 10,000 cycles) acoustic cycles [45-47]. SPIO are typically 80 – 150 nm [17] nanoparticles which may require uptake by endocytosis, as this has been shown to be the main uptake mechanism for therapeutics larger than ~17 nm in radius [46]. This is the reason why we chose to study 10,000 acoustic cycles.

Materials and Methods

Endothelial cells

Human umbilical vein endothelial cells (HUVECs) (Lonza, Verviers, Belgium) were cultured in EGM-2 (Lonza) medium in T75 flasks (BD, Breda, the Netherlands) in a humidified incubator at 37°C with 5% CO_2. Cells were detached with 0.25% Trypsin in EDTA (Lonza) and replated on one side of the acoustically transparent OptiCell™ (NUNC, Wiesbaden, Germany) chambers.

HUVECs were cultured as described before [48], for two days until 70% confluence to resemble neovasculature endothelial cells.

Targeted microbubbles

Biotinylated lipid-coated microbubbles (mean diameter 2.5 μm) consisting of a coating of DSPC (84.8 mol %; P 6517; Sigma-Aldrich, Zwijndrecht, the Netherlands), PEG-40 stearate (8.2 mol %; P 3440; Sigma-Aldrich), DSPE-PEG(2000) (5.9 mol %; 880125 P; Avanti Polar Lipids, Alabaster, AL, USA), and DSPE- PEG(2000)-biotin (1.1 mol %; 880129 C; Avanti Polar Lipids) with a perfluorobutane (C_4F_{10}) gas core (F2 Chemicals, Preson, UK) were made by sonication as previously described [49, 50]. Biotinylated anti-human CD31-antibody (BAM3567; R&D Systems, Europe, Abingdon, United Kingdom) was conjugated to the microbubbles via avidin-biotin bridging as previously described [50, 51]. Specificity of binding of these CD31-targted microbubbles was previously reported by us [48].

Cell treatment

The concentration of tMB was evaluated by Coulter Counter (Multisizer 3, Beckman Coulter, Mijdrecht, the Netherlands) measurements (n = 3) using a 20-μm aperture tube allowing quantification of particle diameters between 0.4 and 12 μm using a linear spacing between the 256 channels. Ten million tMB were added to an OptiCell™ chamber with cells plated on the bottom (cell to bubble ratio of 1:3), which was turned upside down to let microbubbles adhere to the cells by flotation. After 5 min incubation at 37°C, the chamber was reverted for the experiment so the bound tMB were on top of the endothelial cells as shown in Fig 1A. SPIO nanoparticles (Endorem™, Gerber S.A., Paris, France) were added at four time-points: 5 min before, immediately before (0 min), 5 min after, and 15 min after insonification as illustrated in Fig 1B, at a final concentration of 22.4 μg Fe/ml. Each OptiCell™ chamber was divided into six acoustically non-overlapping areas (25 × 30 mm each; see Fig 1C), which covered the beam area (6.5 mm for -6dB beam width) at the focus of the 1.0 MHz transducer (V303; Panametrics-NDT™, Olympus NDT, Waltham, MA, USA), as verified in advance with a calibrated 0.2 mm PVDF needle hydrophone (Precision Acoustics Ltd, Dorchester, UK). The OptiCell chamber was placed into a 37 °C water bath and connected to a 2D micropositioner (Fig 1 D). The 1

MHz focused transducer was configured at a 45° angle below the sample and the acoustic focus was aligned with the center of each subsection.

During the experiment, the position of the OptiCell chamber was manipulated so that the center of each subsection was insonified in sequence at a predefined pressure (10 to 160 kPa peak negative pressure (PNP), Fig 1C). A prolonged burst of 10,000 cycles with a repetition rate of 20 Hz was applied generated by an arbitrary waveform generator (33220A, Agilent, Palo Alto, CA, USA) and amplified using a broadband amplifier (ENI A-500, Electronics & Innovation, Rochester, NY, USA). The first subsection, without the application of ultrasound, was used as the control. The effect of the different total insonification time was determined (1 s, 10 s, and 30 s) at 40, 80, and 160 kPa PNP when SPIO were added 5 min prior to insonfication. To investigate the effect of the incubation time with SPIO, the OptiCells were incubated at 37°C for 5 min, 1 h, and 3 h after insonification when SPIO were added 5 min prior to insonification. The effect of SPIO addition time (-5, 0, 5, and 15 min with
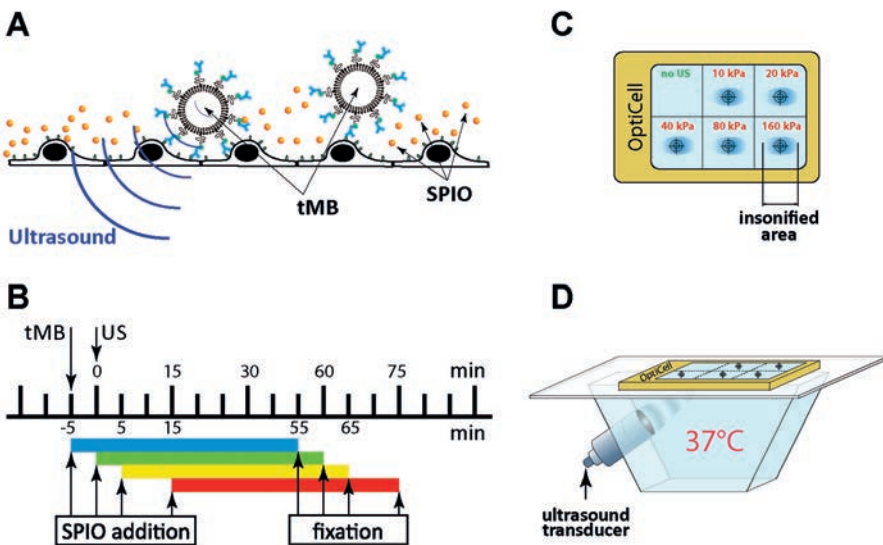
Figure 1 Experimental setup. A Schematic representation of the tMB adhering to HUVECs during treatment. **B** Timing diagram of the experiment. The time of insonification (0 min) was used as the reference time. Targeted microbubbles (tMB) were added 5 min before the ultrasound was applied; SPIO was added 5 min before (i.e. -5 min), just before (i.e. 0 min), 5 min after, and 15 min after insonification. Cells were fixated 60 min after SPIO addition. **C** Scheme of insonification of subsections of the OptiCell™ chamber (to scale). The acoustic pressure is given in PNP. **D** The treatment setup.

respect to the start of insonification) was determined at 10, 20, 40, 80, and 160 kPa PNP. To check the effect of insonification of HUVECs on SPIO uptake in the absence of tMBs, the OptiCells were insonified at 40, 80, and 160 kPa PNP for 30 s, while SPIO was added 5 min prior to insonification (n = 2). All other experiments were repeated three times. From these three datasets the average and standard deviation are plotted.

SPIO labeling

After the treatment described above (see also Fig 1B), cells were rinsed three times with phosphate-buffer saline (PBS; Invitrogen, Groningen, the Netherlands) to remove non-internalized SPIO. Then, cells were fixated with 4% formaldehyde (Sigma-Aldrich, Zwijndrecht, the Netherlands) for 10 min. After fixation, the cells were washed three times with PBS and then incubated with Prussian Blue solution for 30 min (aqueous solution of 10% hydrochloric acid (Sigma-Aldrich) and 5% potassium ferrocyanide (Sigma-Aldrich)) to assess the SPIO-labeling [52]. Next, the cells were washed three times with PBS and the nuclei were stained with 0.1% nuclear fast red solution (Sigma-Aldrich). Thereafter the OptiCells were dried for 48 h and microscopically examined using a microscope (Olympus, Zoeterwoude, the Netherlands) equipped with 20× Plan (NA 0.4) objective (Olympus) and a color camera (Axiocam MRc, Carl Zeiss, Germany). SPIO uptake was assessed by manually counting Prussian Blue positive cells among ~500 cells (acquired in 5 fields of view) located within a circle of 6 mm diameter around the center point of each insonified area. A cell was counted as SPIO positive when it contained one or more Prussian Blue stained iron particles.

Cell viability assay

For each SPIO uptake measurement, cell viability was determined in triplicate by calcein-AM and propidium iodide (PI) assays in parallel. Cells were treated with SPIO, tMB and ultrasound as described before (see also Fig 1). Within 3 to 4 min after the US treatment of all subsections of the Opticells, HUVECs were incubated at 37 °C, 5% CO_2. Thirty min before assessing the cell viability, calcein-AM was added to the OptiCell chamber (C3100MP; Invitrogen; 0.25 μM final concentration from a 1 mM stock prepared in DMSO (Sigma-Aldrich)) and incubated for 30 min under the same conditions. Thereafter PI (P4864, Sigma-Aldrich, 25 μg/ml final concentration) and Hoechst

33342 (Invitrogen; 5 µg/ml final concentration) were added to the Opticell chamber. Microscopic examination was performed directly after the PI and Hoechst addition with a fluorescent microscope (Olympus) equipped with the same setup as applied for SPIO labeling measurements, only that a 5× LMPlanFl (NA 0.13) objective (Olympus) was used here. For each condition five different fields of view were acquired (~2900 cells) within the 6 mm circle around the center of the insonified area. Different filter sets (U-MWU2, 330 – 385/420 nm; U-MWIB2, 460 – 490/510 nm; U-MWG2, 510 – 550/570 nm, Olympus) were applied for detecting all cells (stained with Hoechst), viable cells (stained with calcein-AM), and dead cells (stained with PI) respectively. All images were automatically analyzed in ImageJ [53]. The Find Maxima function in ImageJ was used to define the exact number of cells. To find an appropriate tolerance for the Find Maxima function in every image, the number of local maxima was defined for tolerance parameters of 0 to 200 in steps of two. We analyzed the differences in number of maxima between the steps. When the difference became smaller than 20, this point was considered as the correct tolerance and the corresponding number of cells as correct number of cells. This approach was validated by selective manual counting of number of cells (n=10). The difference between manual and automatic counting was 2.1±0.4%. As shown in S1 Fig, the % of viable cells determined from the calcein-AM staining (live cells) was the same as the cell viability determined from the PI staining (dead cells). The cell viability data was therefore presented as the % of viable cells determined from the calcein-AM staining.

4

Results

Microbubble dynamics

During all studied ultrasound bursts, we observed displacement and disappearance of tMB. This was most pronounced for the 30 s insonification period, as shown in Fig 2. During insonification, tMB also clustered (Figs 2B-D). After the 30 s insonification period, no tMB were observed in the field of view (Fig 2E), suggesting they had been destroyed.
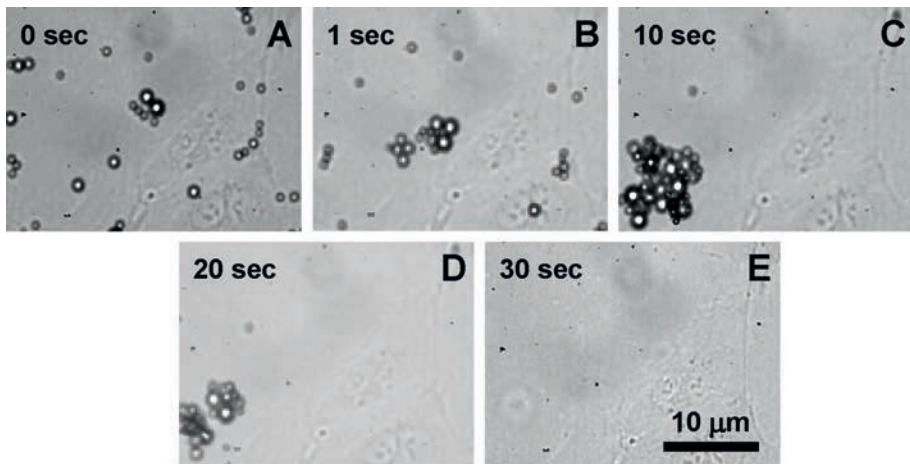

Figure 2 Optical recording of tMB on HUVECs during ultrasound treatment. A before treatment. **B-E** tMB displacement, clustering, and destroyment during 30 s insonification (1 MHz, 80 kPa PNP, 10,000 cycles, repetition rate of 20 Hz, 30 s insonification treatment, SPIO added at -5 min with respect to the start of insonification).

Insonification duration

In the absence of ultrasound, less than 2% of cells intracellularly incorporated SPIO naturally (Fig 3A). The efficacy of SPIO uptake by HUVECs and the corresponding cell viability as a function of the acoustic PNP and the total insonification duration (1, 10, or 30 s) at low MI (<0.16) are shown in Fig 3. The total ultrasound exposure time was a key factor for SPIO uptake efficacy. This was demonstrated by the amount of SPIO positive cells not exceeding 4% for 1 s and 6% for 10 s of insonification, but with 30 s of insonification the amount of SPIO positive cells increased to more than 10%. Additionally, the PNP also influenced SPIO uptake significantly. With 30 s of insonification, the proportion of SPIO positive cells significantly increased with the PNP (i.e., from

~10% at 40 kPa to ~16% at 160 kPa). At the same time, cell viability (Fig 3B) decreased with both the increasing acoustical pressure and the insonification time. For example at 80 kPa PNP, the cell viability decreased from ~70% for 10 s of insonification to ~60% for 30 s of insonification. For a treatment time of 30 s, the cell viability dropped by nearly two-fold from 40 kPa to 160 kPa PNP. In general, the cell viability remained high for up to 40 kPa PNP. Specifically, insonification for 30 s demonstrated the best SPIO uptake and was selected for further experiments. We did not investigate a longer insonification time because after 30 s all tMB were destroyed (see Fig 2E).
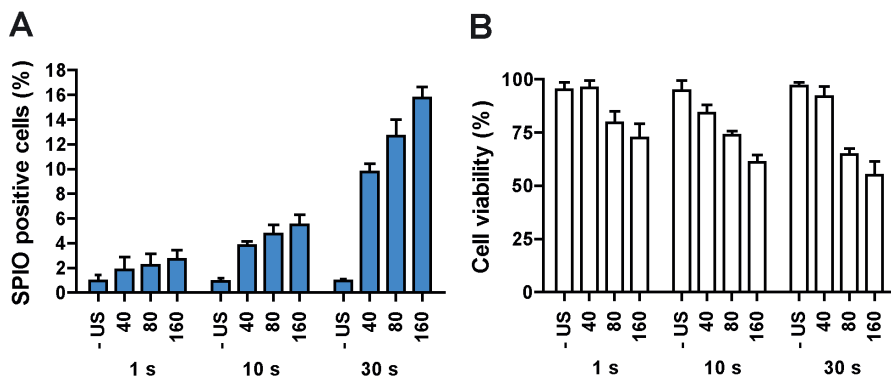
4

Figure 3 The influence of ultrasound insonification time on intracellular SPIO uptake efficiency. A SPIO positive cells. **B** Cell viability. HUVECs were treated with tMB and no ultrasound (- US) or ultrasound at varying PNP (40, 80, or 160 kPa) for 1, 10, or 30 s; SPIO added 5 min before insonification (-5 min); 1 h of incubation after SPIO addition.

SPIO incubation time

The influence of the SPIO incubation time (5 min, 1 h or 3 h) after the treatment with ultrasound and tMB on SPIO uptake and cell viability is illustrated in Fig 4. In general, SPIO uptake increased prominently with the incubation time, for example for 180 kPa PNP SPIO uptake increased from below ~4% to ~22%. The largest ratio between control and treated uptake was at 1 h of incubation for all PNPs. Cell viability (Fig 4B) remained high (>75%) at 40 kPa PNP for all incubation times. It decreased with the pressure (80 – 160 kPa PNP) for both 1 h and 3 h of incubation time. A longer incubation time did not lower cell viability, as cell viability was slightly higher after 3 h of incubation than after 1 h of incubation. Based on the results from this experiment, 1 h of incubation with SPIO was selected for further investigations.
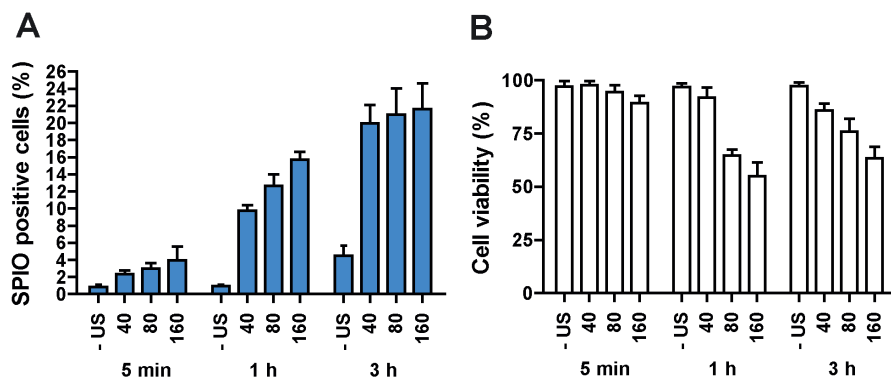
Figure 4 The influence of SPIO incubation time on intracellular SPIO uptake efficiency. A SPIO positive cells. **B** Cell viability. HUVECs were treated with tMB and no ultrasound (- US) or ultrasound at varying PNP (40, 80, or 160 kPa) for 30 s. SPIO were added 5 min before insonification (-5 min). Incubation time after SPIO addition was varied from 5 min to 1 h and 3 h.

SPIO addition time

In Fig 5 the percentage of SPIO positive cells and cell viability are plotted for four different times between insonification and SPIO addition for different acoustic PNP. Similar to the previous observations, no ultrasound application resulted in less than 2% of SPIO positive cells. In addition, ultrasound application without tMBs present showed no significant difference in SPIO uptake in comparison to the control without ultrasound application for all studied PNP when the SPIO were added 5 min prior to insonification. For both additions of SPIO at 5 min prior (-5 min) and just before (0 min) the ultrasound application, we obtained a relatively large percentage of SPIO positive cells

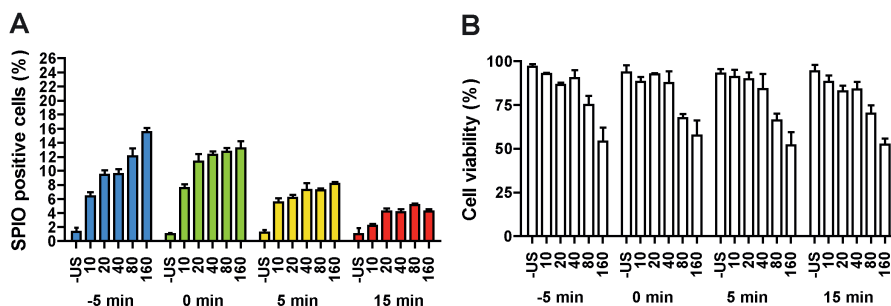**Figure 5 The influence of SPIO addition time on intracellular SPIO uptake efficiency**. **A** SPIO positive cells. **B** Cell viability. HUVECs were treated with tMB and no ultrasound (- US) or ultrasound at varying PNP (10, 20, 40, 80, or 160 kPa) for 30 s; SPIO were added 5 min before insonification (-5 min), just before insonification (0 min), 5 min after or 15 min after insonification; 1 h of incubation after SPIO addition.

(~>10%) for acoustic pressures above 20 kPa PNP. Moreover, the percentage of SPIO positive cells increased up to ~12-15% with higher PNP for SPIO addition before the insonification. In contrast, SPIO addition at 5 and 15 min after ultrasound application resulted in much lower SPIO uptake (<8%). Similarly, the cell viability remained above 50% for all settings.

SPIO cell labeling

In the absence of ultrasound, intracellularly incorporated SPIO were detected as small iron particle aggregates distributed in the cytoplasm (Figs 6A, 6B).
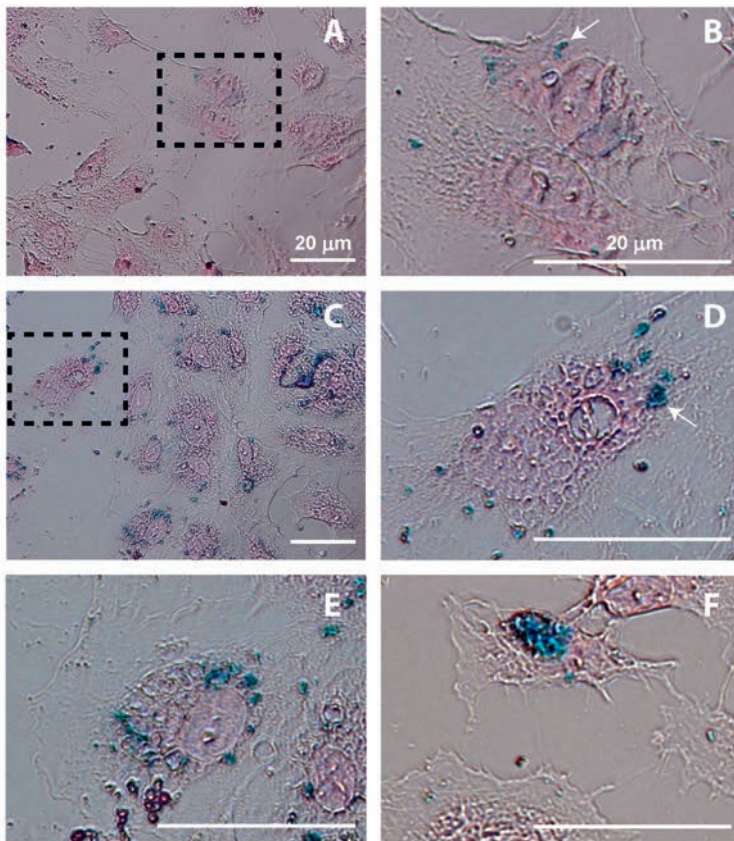
Figure 6 SPIO cell labeling. Prussian Blue staining of SPIO uptake in (**A**, **B**) the control (i.e. no ultrasound, 1 h after incubation) and in (**C**–**F**) the ultrasound and tMB treated HUVECs at different treatment conditions. **C,D,E**: 80 kPa PNP, SPIO added at -5 min, 30 s insonification, 1 h incubation after SPIO addition; F: 160 kPa PNP, SPIO added at 15 min, 30 s insonification, 1 h incubation after SPIO addition. **B** and **D** are zoomed in from **A** and **C** as illustrated by the dashed rectangles. In **B** and **D**, one example of a SPIO aggregate is indicated by an arrow.

Ultrasound and tMB treated cells demonstrated much higher SPIO uptake as shown in Figs 6C–G. Iron particles were detected as aggregates of different sizes in the cytoplasm (Figs 6C, 6D). Other typical individual examples of intracellular SPIO distribution patterns after ultrasound and tMB treatment are shown in Figs 6E-F. These staining patterns included distribution of aggregates varying in size and blue intensity throughout the cytoplasm (Fig 6E) and one large aggregate mainly located near the nucleus (Fig 6F) having a higher blue intensity in comparison to the aggregates in Fig 6E. The intensity differences of the blue stain suggest different concentrations of SPIO particles.

Discussion

Tracking of endothelial cells is important for cancer and cardiovascular disease. There are several ways of SPIO cell labeling *in vitro* [22, 54]. Most of these techniques require different transfection agents, which cannot be used *in vivo* due to the associated high toxicity and systemic effects. We therefore studied a technique, based on ultrasound-activated ultrasound contrast agents that will be compatible for *in vivo* use. The SPIO uptake was dependent on multiple factors, including the ultrasound settings, the time of SPIO addition, and the incubation time of SPIO with cells after the ultrasound treatment. Optimal labeling at 1 MHz ultrasound frequency was observed when the ultrasound parameters were 40 kPa peak negative pressure (MI 0.04), 10,000 cycles and repetition rate of 20 Hz, applied for 30 s when SPIO were added at 0 min. Compared to the control, this resulted in an approximate 12 times increase of SPIO uptake with 85% cell viability.

Microbubble dynamics
We found an increasing trend of both SPIO positive cells and cell death with the acoustic PNP increase. Note that we studied acoustic pressures up to 160 kPa PNP, a regime in which the amplitude of radial lipid-coated microbubble oscillations increases with pressure [55, 56]. A previous study by Vos et al. [57] has reported that highly non-spherical microbubble vibrations can be induced at pressures as low as 140 kPa PNP for lipid-coated microbubbles at resonance. In this regime, the acoustic streaming generated by oscillating microbubbles and the produced shear stresses [58-61] can be one of the mechanisms for

enhanced permeability of the cell membrane [26]. As was expected, the total duration of insonification also showed an effect on the SPIO uptake (Fig 3A). It has been reported that at 1 MHz frequency at a low mechanical index (MI < 0.1), a lipid-coated microbubble can repeatedly oscillate for thousands of cycles; while at higher MI microbubbles are destroyed within about 100 µs (i.e. 100 cycles) irrespective of pulse length [62]. We indeed observed microbubbles still present up to 30 s at 80 kPa PNP (MI=0.08) (Fig 2). The improved uptake with prolonged insonification may be related with the persistent effect produced by microstreaming generated by microbubble vibrations as formulated earlier. Moreover, we noticed displacement of tMB with subsequent microbubble clustering and merging driven by secondary radiation force over the prolonged burst, as illustrated by Fig 2. These findings are in line with our previous study where tMB bound to endothelial cells also displaced, clustered, and merged by insonification at 1 MHz, albeit for a single burst of up to 50,000 cycles [63]. Detachment of bound lipid-coated tMB has been reported to be due to the attractive secondary Bjerknes force between two tMB [64, 65]. Aggregation of detached tMB forming bigger microbubble clusters may have influenced their oscillation dynamics as larger microbubbles have a lower resonance frequency than individual small microbubbles [66]. At a low driving frequency (for example 1 MHz as applied in this study), microbubble clusters are expected to have a higher amplitude of oscillation as they will be closer to resonance, which could have contributed to the enhanced SPIO uptake.

SPIO uptake

In our study, HUVECs showed ~1% natural uptake after 1 h of incubation, and this value increased to ~5% after 3 h (Fig 4A). Although the natural uptake of SPIO by HUVECs was previously reported by van Tiel et al. [67], this percentage of labeled cells is not sufficient for cell tracking. Treatment of HUVECs with ultrasound and tMB led to a dramatic increase of ~10-fold in SPIO uptake after 1 h incubation (Fig 4A). On the other hand, cell viability decreased between 5 min and 1 h incubation time (Fig 4B), suggesting that instantaneous cell death (i.e. irreversible sonoporation due to large pores) is less prominent than induced cell death. Induced cell death could occur via the apoptotic pathway, a process that takes time [68, 69], that can be activated by ultrasound and microbubbles as previously reported by others [70-72]. We also observed that the SPIO labeling efficiency was influenced by the SPIO addition time in

respect to the time of treatment with tMB and ultrasound (Fig 5). We observed the highest efficacy when SPIO were added with the tMB (0 min) for acoustic PNPs up to 80 kPa. When SPIO were added 5 or 15 min after treatment, SPIO uptake was lower, but still significantly higher (more than fivefold at 5 min) than natural uptake. This may suggest stimulated endocytosis as uptake mechanism rather than sonoporation, since resealing of pores created by ultrasound activated microbubbles has been reported on a relatively short time scale of up to a minute [28, 73]. On the other hand, our results may also suggest that both uptake by stimulated endocytosis and pore formation occurred when SPIO were added 5 min before or just before (0 min) treatment (Fig 5A). This is supported by four earlier ultrasound contrast agent studies [46, 47, 74, 75] as they reported uptake by both pore formation and endocytosis using similar (1 MHz [46, 47, 74, 75]) and different (0.3 MHz [74]) acoustic settings. Meijering et al. [46] and De Cock et al. [47] also addressed the influence of particle size on the uptake route: for dextrans larger than ~17 nm in radius, the primary uptake route was endocytosis instead of pore formation. On the other hand, pores of 1 nm in size [76] to > 100 μm^2 in area [28] have been observed. However, induced pores >100 μm^2 do not tend to reseal [28] which likely leads to cell death. This could explain why higher acoustic pressures (i.e., ≥ 80 kPa) in our study corresponded to increased cell death. Pores < 100 μm^2 can still reseal, according to a recent study [28]. The SPIO colloid with low molecular weight dextran coating in Endorem^{TM}, as used in our study, are 120 – 180 nm in size [77] so they could enter cells via resealable pores. The reason why Meijering et al. [46] observed dextran particles larger than ~17 nm mainly to be taken up by endocytosis, could be the different type of microbubble used (SonoVue versus tMB in our study) and/or the type of cells studied (bovine aortic endothelial cells versus HUVECs in our study).

The amount of SPIO positive cells was almost two times higher when SPIO were added 5 min instead of 15 min after insonification. This suggests a relatively short temporal window when the therapeutic agent can be actively taken up after microbubble insonification, especially when compared to the study by Yudina et al. who reported a temporal window of 24 h [78]. The difference could be due to the therapeutic compound (small 600 Da molecule Sytox Green versus the 120 – 180 nm SPIO in our study), the type of microbubble (SonoVue versus tMB in our study), the acoustic settings (ultrasound frequency

of 1.5 MHz, 440 kPa PNP, 300 cycles at 1 kHz repetition rate for 30 s versus 1 MHz, ≤160 kPa PNP, 10,000 cycles at 20 Hz for 30 s in our study) and/or the type of cells studied (C6 rat glioma cells versus HUVECs in our study). Recently, the temporal window was reported to be cell type-dependent by the same group [79]. For HUVECs, the temporal was found to be 1 h for the small molecule SYTOX green.

In our study, we defined a cell as SPIO positive when we detected one or more SPIO particles within the cell. It is unlikely that the SPIO particles we detected were extracellular because the cells were washed three times. We observed different labeling patterns, namely differences in the intensity and the intracellular distribution of the SPIO particles, although we did not quantify this degree of uptake. Some cells took up small spots (submicron) of SPIO as dense granules ~2 nm in diameter, while others had large SPIO aggregates in the cytoplasm. This variation in uptake patterns may also suggest uptake by pore formation and endocytosis as SPIO homogeneously distributed in the cytoplasm may suggest pore formation while small aggregates may indicate endocytic uptake. This is supported by different uptake patterns previously reported for dextrans with aggregates verified to be co-localized with endocytic vesicles [46, 47].

As ultrasound contrast agent-mediated SPIO-labeling of endothelial cells is likely faster clinically approved for labeling tumor vasculature, we decided to mimic the tumor vasculature's compromised endothelial monolayer with poorly connected and sprouting endothelial cells [80] by culturing the HUVECs till 70% confluence. Our findings of effective tMB-mediated SPIO-labeling may therefore not be applicable to a monolayer of HUVECs, i.e. 100% confluence, applicable to vascular grafts. Different ultrasound pressures may be needed for effective tMB-mediated SPIO-labeling HUVECs in a monolayer as cells in a monolayer are more likely in the senescent cell cycle phase (G_0) and have a more organized cytoskeleton. With respect to sensitivity to ultrasound treatment, cells in the mitotis(M)-phase [81, 82] and synthesis(S)-phase [82] have been reported most sensitive whereas cells in the senescent cell cycle phase were least sensitive. By contrast, another study showed the opposite: cells in the M and S-phases were more resistant to ultrasound treatment [83]. However, these ultrasound sensitivity studies were performed without the

4

presence of MB and on cancer/epithelial cells. These studies may therefore not translate to our study and it needs further investigation whether the amount of cell confluence influences the response to tMB-treatment.

It was previously shown [38] that microbubbles with SPIO incorporated in their coating in combination with ultrasound could lead to an about three fold increase of SPIO labeling of tumor cells *in vitro,* without compromising cell viability. A polymer coated microbubble was used, which has been shown to behave differently than a lipid coated microbubble when exposed to ultrasound. Polymer microbubbles have a stiff coating, which can respond to ultrasound exposure under a high MI (>1) by cracking and releasing the encapsulated gas. On the contrary, lipid coated microbubbles will oscillate at low MI and can also fuse [26]. They can therefore have a more prolonged interaction with cells than polymer microbubbles. This could explain why we found a ~12 fold increase in SPIO labeling compared to the control treatment.

Clinical implications

From the *in vivo* perspective, using tMB instead of non-tMB is preferable for endothelial cell labeling and drug delivery since tMB can be specifically targeted to diseased endothelial cells [84]. In addition, when ultrasound is applied to bound tMB, the vibrations of the ultrasound-activated tMB will have a direct effect on the cell membrane. This may be the reason why tMB have been shown to be up to ~5 times more effective in stimulating cellular uptake of therapeutics *in vivo* [30]. CD31 used as target in this proof of concept study was chosen as model ligand because it is constitutively expressed on endothelial cell membranes. It can therefore be used to label endothelial cells with SPIO in tissue-engineered valves or vascular grafts *in vitro*. However, CD31 cannot be used *in vivo* as it is expressed throughout the entire vasculature tree [85]. For targeting tMB to tumor vasculature, $\alpha_v\beta_3$ or vascular endothelial growth factor receptor 2 (VEGFR2) can be used [84]. SPIO uptake by ultrasound-activated tMB *in vivo* is expected as we recently reported that tMB bound to $\alpha_v\beta_3$ can stimulate endothelial cell drug uptake *in vivo* [50]. VEGFR2 is another biomarker of interest for tMB. BR55, a tMB against VEGFR2, has recently successfully been used in clinical trials for prostate, breast, and ovarian cancer [86, 87]. Our future studies will focus on *in vivo* SPIO labeling as well as *in vivo* MRI tracking of the labeled endothelial cells. For the *in vivo* studies, our *in vitro* acoustic settings will need to be extrapolated taking into account that ultrasound is attenuated

by tissue (0.5 dB/cm/MHz [88]) and the microbubble vibration is damped in blood [89]. In our *in vitro* study we incubated the HUVECs for 1 h with the SPIO. As the elimination half-life of Endorem™ (Feridex® in the USA) is 2.4 ± 0.2 h in humans and the SPIO are administered as a drip infusion over ~30 min [77, 90], it may be expected that the SPIO will circulate long enough *in vivo* to also achieve the 1 h incubation period. It was shown before that single cell tracking is possible by MRI using iron oxide as the label [13, 14, 16]. The micron-sized paramagnetic iron oxide (MPIO) particles used in one of these studies [13] are ten times bigger (1.6 µm) than SPIO. As it was revealed before [67] that the iron content of cells labeled with SPIO is less (~10 folds) than with MPIO, more cells may have to be labeled by SPIO to be detectable by MRI *in vivo*.

4

Conclusion

Our study shows that ultrasound-activated tMB are a promising technique to non-invasively enhance SPIO uptake by endothelial cells. From the current *in vitro* study, we derived optimal ultrasound parameters for SPIO delivery to HUVECs, that is, 40 kPa at 1 MHz (MI 0.04), 10,000 cycles and repetition rate of 20 Hz, applied for 30 s when SPIO were added at 0 min. This setting increased SPIO uptake up to 12 times compared to the control with 85% cell viability.

Acknowledgments

References

1. Akbari-Birgani S, Paranjothy T, Zuse A, Janikowski T, Cieslar-Pobuda A, Likus W, et al. Cancer stem cells, cancer-initiating cells and methods for their detection. Drug Discov Today. 2016;21(5):836-42.

2. Moreira ML, da Costa Medeiros P, de Souza SA, Gutfilen B, Rosado-de-Castro PH. In Vivo Tracking of Cell Therapies for Cardiac Diseases with Nuclear Medicine. Stem Cells Int. 2016;2016:3140120.

3. Bernsen MR, Kooiman K, Segbers M, van Leeuwen FW, de Jong M. Biomarkers in preclinical cancer imaging. Eur J Nucl Med Mol Imaging. 2015;42(4):579-96.

4. Accomasso L, Gallina C, Turinetto V, Giachino C. Stem Cell Tracking with Nanoparticles for Regenerative Medicine Purposes: An Overview. Stem Cells Int. 2016;2016:7920358.

5. Liu Z, Li Z. Molecular imaging in tracking tumor-specific cytotoxic T lymphocytes (CTLs). Theranostics. 2014;4(10):990-1001.

6. Hong H, Yang Y, Zhang Y, Cai W. Non-invasive cell tracking in cancer and cancer therapy. Curr Top Med Chem. 2010;10(12):1237-48.

7. Gimi B, Mori N, Ackerstaff E, Frost EE, Bulte JW, Bhujwalla ZM. Noninvasive MRI of endothelial cell response to human breast cancer cells. Neoplasia. 2006;8(3):207-13.

8. Xiong L, Cao F, Cao X, Guo Y, Zhang Y, Cai X. Long-term-stable near-infrared polymer dots with ultrasmall size and narrow-band emission for imaging tumor vasculature in vivo. Bioconjug Chem. 2015;26(5):817-21.

9. Ramaswamy S, Schornack PA, Smelko AG, Boronyak SM, Ivanova J, Mayer JE, Jr., et al. Superparamagnetic iron oxide (SPIO) labeling efficiency and subsequent MRI tracking of native cell populations pertinent to pulmonary heart valve tissue engineering studies. NMR Biomed. 2012;25(3):410-7.

10. Fayol D, Le Visage C, Ino J, Gazeau F, Letourneur D, Wilhelm C. Design of biomimetic vascular grafts with magnetic endothelial patterning. Cell Transplant. 2013;22(11):2105-18.

11. Fu Y, Azene N, Xu Y, Kraitchman DL. Tracking stem cells for cardiovascular applications in vivo: focus on imaging techniques. Imaging Med. 2011;3(4):473-86.

12. Youn H, Hong KJ. In vivo non invasive molecular imaging for immune cell tracking in small animals. Immune Netw. 2012;12(6):223-9.

13. Shapiro EM, Sharer K, Skrtic S, Koretsky AP. In vivo detection of single cells by MRI. Magn Reson Med. 2006;55(2):242-9.

14. Lee N, Kim H, Choi SH, Park M, Kim D, Kim HC, et al. Magnetosome-like ferrimagnetic iron oxide nanocubes for highly sensitive MRI of single cells and transplanted pancreatic islets. Proc Natl Acad Sci USA. 2011;108(7):2662-7.

15. Ngen EJ, Artemov D. Advances in Monitoring Cell-Based Therapies with Magnetic Resonance Imaging: Future Perspectives. Int J Mol Sci. 2017;18(1).

16. Zhang Z, van den Bos EJ, Wielopolski PA, de Jong-Popijus M, Bernsen MR, Duncker DJ, et al. In vitro imaging of single living human umbilical vein endothelial cells with a clinical 3.0-T MRI scanner. MAGMA. 2005;18(4):175-85.

17. Gamarra LF, Brito GES, Pontuschka WM, Amaro E, Parma AHC, Goya GF. Biocompatible superparamagnetic iron oxide nanoparticles used for contrast agents: a structural and magnetic study. J Magn Magn Mater. 2005;289(0):439-41.

18. Neuwelt A, Sidhu N, Hu CA, Mlady G, Eberhardt SC, Sillerud LO. Iron-based superparamagnetic nanoparticle contrast agents for MRI of infection and inflammation. AJR Am J Roentgenol. 2015;204(3):W302-13.

19. Bernsen MR, Guenoun J, Van Tiel ST, Krestin GP. Nanoparticles and clinically applicable cell tracking. Brit J Radiol. 2015;88(1054).

20. Reddy LH. Drug delivery to tumours: recent strategies. J Pharm Pharmacol. 2005;57(10):1231-42.

21. Reddy LH, Arias JL, Nicolas J, Couvreur P. Magnetic nanoparticles: design and characterization, toxicity and biocompatibility, pharmaceutical and biomedical applications. Chem Rev. 2012;112(11):5818-78.

22. Frank JA, Anderson SA, Kalsih H, Jordan EK, Lewis BK, Yocum GT, et al. Methods for magnetically labeling stem and other cells for detection by in vivo magnetic resonance imaging. Cytotherapy. 2004;6(6):621-5.

23. Rodriguez-Porcel M, Kronenberg MW, Henry TD, Traverse JH, Pepine CJ, Ellis SG, et al. Cell tracking and the development of cell-based therapies: a view from the Cardiovascular Cell Therapy Research Network. JACC Cardiovasc Imaging. 2012;5(5):559-65.

24. Ferrara K, Pollard R, Borden M. Ultrasound microbubble contrast agents: fundamentals and application to gene and drug delivery. Annu Rev Biomed Eng. 2007;9:415-47.

25. Lentacker I, De Cock I, Deckers R, De Smedt S, Moonen CTW. Understanding ultrasound induced sonoporation: Definitions and underlying mechanisms. Adv Drug Deliver Rev. 2014.

26. Kooiman K, Vos HJ, Versluis M, de Jong N. Acoustic behavior of microbubbles and implications for drug delivery. Adv Drug Deliver Rev. 2014;72C:28-48.

27. Sutton JT, Haworth KJ, Pyne-Geithman G, Holland CK. Ultrasound-mediated drug delivery for cardiovascular disease. Expert Opin Drug Deliv. 2013;10(5):573-92.

28. Hu Y, Wan JM, Yu AC. Membrane perforation and recovery dynamics in microbubble-mediated sonoporation. Ultrasound Med Biol. 2013;39(12):2393-405.

29. Yan F, Li X, Jin Q, Jiang C, Zhang Z, Ling T, et al. Therapeutic ultrasonic microbubbles carrying paclitaxel and LyP-1 peptide: preparation, characterization and application to ultrasound-assisted chemotherapy in breast cancer cells. Ultrasound Med Biol. 2011;37(5):768-79.

30. Xie A, Belcik T, Qi Y, Morgan TK, Champaneri SA, Taylor S, et al. Ultrasound-Mediated Vascular Gene Transfection by Cavitation of Endothelial-Targeted Cationic Microbubbles. JACC Cardiovasc Imag. 2012;5(12):1253-62.

31. Klibanov AL. Preparation of targeted microbubbles: ultrasound contrast agents for molecular imaging. Med Biol Eng Comput. 2009;47(8):875-82.

32. van Rooij T, Daeichin V, Skachkov I, de Jong N, Kooiman K. Targeted ultrasound contrast agents for ultrasound molecular imaging and therapy. Int J Hyperthermia. 2015;31(2):90-106.

33. Liu HL, Chen PY, Yang HW, Wu JS, Tseng IC, Ma YJ, et al. In vivo MR quantification of superparamagnetic iron oxide nanoparticle leakage during low-frequency-ultrasound-induced blood-brain barrier opening in swine. J Magn Reson Imaging. 2011;34(6):1313-24.

34. Fan CH, Ting CY, Lin HJ, Wang CH, Liu HL, Yen TC, et al. SPIO-conjugated, doxorubicin-loaded microbubbles for concurrent MRI and focused-ultrasound enhanced brain-tumor drug delivery. Biomaterials. 2013;34(14):3706-15.

35. Fan CH, Cheng YH, Ting CY, Ho YJ, Hsu PH, Liu HL, et al. Ultrasound/Magnetic Targeting with SPIO-DOX-Microbubble Complex for Image-Guided Drug Delivery in Brain Tumors. Theranostics. 2016;6(10):1542-56.

36. Gao WQ, Li X, Liu PC, Bai ZY, Zhong YF, Han HB, et al. Investigation in vivo of effect of ultrasound-mediated microbubble destruction on entrance of feridex into the aortal wall. Zhonghua yi xue za zhi. 2009;89(39):2797-801.

37. Liu ZY, Wang Y, Liang CH, Li XH, Wang GY, Liu HJ, et al. In vitro labeling of mesenchymal stem cells with superparamagnetic iron oxide by means of microbubble-enhanced US exposure: initial experience. Radiology. 2009;253(1):153-9.

38. Yang F, Zhang M, He W, Chen P, Cai X, Yang L, et al. Controlled release of Fe3O4 nanoparticles in encapsulated microbubbles to tumor cells via sonoporation and associated cellular bioeffects. Small. 2011;7(7):902-10.

39. Correas JM, Helenon O, Pourcelot L, Moreau JF. Ultrasound contrast agents. Examples of blood pool agents. Acta Radiol Suppl. 1997;412:101-12.

40. Greis C. Ultrasound contrast agents as markers of vascularity and microcirculation. Clin Hemorheol Microcirc. 2009;43(1):1-9.

41. Eguchi S, Takatsuki M, Hidaka M, Soyama A, Tomonaga T, Muraoka I, et al. Predictor for histological microvascular invasion of hepatocellular carcinoma: a lesson from 229 consecutive cases of curative liver resection. World J Surg. 2010;34(5):1034-8.

42. Sternberg A, Amar M, Alfici R, Groisman G. Conclusions from a study of venous invasion in stage IV colorectal adenocarcinoma. J Clin Pathol. 2002;55(1):17-21.

4

43. Pu C, Chang S, Sun J, Zhu S, Liu H, Zhu Y, et al. Ultrasound-mediated destruction of LHRHa-targeted and paclitaxel-loaded lipid microbubbles for the treatment of intraperitoneal ovarian cancer xenografts. Mol Pharm. 2014;11(1):49-58.

44. Newman PJ, Newman DK. Signal transduction pathways mediated by PECAM-1: new roles for an old molecule in platelet and vascular cell biology. Arterioscl Thromb Vas. 2003;23(6):953-64.

45. Jin LF, Li F, Wang HP, Wei F, Qin P, Du LF. Ultrasound targeted microbubble destruction stimulates cellular endocytosis in facilitation of adeno-associated virus delivery. Int J Mol Sci. 2013;14(5):9737-50.

46. Meijering BD, Juffermans LJ, van Wamel A, Henning RH, Zuhorn IS, Emmer M, et al. Ultrasound and microbubble-targeted delivery of macromolecules is regulated by induction of endocytosis and pore formation. Circ Res. 2009;104(5):679-87.

47. De Cock I, Zagato E, Braeckmans K, Luan Y, de Jong N, De Smedt SC, et al. Ultrasound and microbubble mediated drug delivery: acoustic pressure as determinant for uptake via membrane pores or endocytosis. J Control Release. 2015;197:20-8.

48. Kooiman K, Foppen-Harteveld M, van der Steen AFW, de Jong N. Sonoporation of endothelial cells by vibrating targeted microbubbles. J Control Release. 2011;154(1):35-41.

49. Klibanov AL, Rasche PT, Hughes MS, Wojdyla JK, Galen KP, Wible JH, Jr., et al. Detection of individual microbubbles of ultrasound contrast agents: imaging of free-floating and targeted bubbles. Invest Radiol. 2004;39(3):187-95.

50. Skachkov I, Luan Y, van der Steen AF, de Jong N, Kooiman K. Targeted microbubble mediated sonoporation of endothelial cells in vivo. IEEE Trans Ultrason Ferroelectr Freq Control. 2014;61(10):1661-7.

51. Lindner JR, Song J, Christiansen J, Klibanov AL, Xu F, Ley K. Ultrasound assessment of inflammation and renal tissue injury with microbubbles targeted to P-selectin. Circulation. 2001;104(17):2107-12.

52. Clark G. Staining procedures used by the Biological Stain Commission. 3 ed: Published for the Biological Stain Commission by Williams & Wilkins; 1973.

53. Rasband WS. ImageJ. Bethesda, Maryland, USA: U.S. National Institutes of Health; 1997-2018.

54. Bernsen MR, Moelker AD, Wielopolski PA, van Tiel ST, Krestin GP. Labelling of mammalian cells for visualisation by MRI. Eur Radiol. 2010;20(2):255-74.

55. Vos HJ, Dollet B, Bosch JG, Versluis M, de Jong N. Nonspherical vibrations of microbubbles in contact with a wall: a pilot study at low mechanical index. Ultrasound Med Biol. 2008;34(4):685-8.

56. Overvelde M, Garbin V, Dollet B, de Jong N, Lohse D, Versluis M. Dynamics of coated microbubbles adherent to a wall. Ultrasound Med Biol. 2011;37(9):1500-8.

57. Vos HJ, Dollet B, Versluis M, de Jong N. Nonspherical Shape Oscillations of Coated Microbubbles in Contact with a Wall. Ultrasound Med Biol. 2011;37(6):935-48.

58. Prentice P, Cuschierp A, Dholakia K, Prausnitz M, Campbell P. Membrane disruption by optically controlled microbubble cavitation. Nat Phys. 2005;1(2):107-10.

59. Mukherjee D, Wong J, Griffin B, Ellis SG, Porter T, Sen S, et al. Ten-fold augmentation of endothelial uptake of vascular endothelial growth factor with ultrasound after systemic administration. J Am Coll Cardiol. 2000;35(6):1678-86.

60. Ohl CD, Arora M, Ikink R, de Jong N, Versluis M, Delius M, et al. Sonoporation from jetting cavitation bubbles. Biophys J. 2006;91(11):4285-95.

61. Ooi A, Tho P, Manasseh R. Cavitation microstreaming patterns in single and multiple bubble systems. J Acoust Soc Am. 2007;122(5):3051.

62. Mannaris C, Averkiou MA. Investigation of microbubble response to long pulses used in ultrasound-enhanced drug delivery. Ultrasound Med Biol. 2012;38(4):681-91.

63. van Rooij T, Skachkov I, Beekers I, Lattwein KR, Voorneveld JD, Kokhuis TJ, et al. Viability of endothelial cells after ultrasound-mediated sonoporation: Influence of targeting, oscillation, and displacement of microbubbles. J Control Release. 2016;238:197-211.

64. Kokhuis TJ, Garbin V, Kooiman K, Naaijkens BA, Juffermans LJ, Kamp O, et al. Secondary Bjerknes forces deform targeted microbubbles. Ultrasound Med Biol. 2013;39(3):490-506.

65. Garbin V, Dollet B, Overvelde M, Cojoc D, Di Fabrizio E, van Wijngaarden L, et al. History force on coated microbubbles propelled by ultrasound. Phys Fluids. 2009;21(9):092003.

66. Dayton PA, Morgan KE, Klibanov AL, Brandenburger GH, Ferrara KW. Optical and acoustical observations of the effects of ultrasound on contrast agents. IEEE Trans Ultrason Ferroelectr Freq Control. 1999;46(1):220-32.

67. van Tiel ST, Wielopolski PA, Houston GC, Krestin GP, Bernsen MR. Variations in labeling protocol influence incorporation, distribution and retention of iron oxide nanoparticles into human umbilical vein endothelial cells. Contrast Media Mol Imaging. 2010;5(5):247-57.

68. Green DR. Apoptotic pathways: ten minutes to dead. Cell. 2005;121(5):671-4.

69. Elmore S. Apoptosis: a review of programmed cell death. Toxicol Pathol. 2007;35(4):495-516.

70. Feril LB, Jr., Kondo T, Zhao QL, Ogawa R, Tachibana K, Kudo N, et al. Enhancement of ultrasound-induced apoptosis and cell lysis by echo-contrast agents. Ultrasound Med Biol. 2003;29(2):331-7.

71. Zhong W, Sit WH, Wan JM, Yu AC. Sonoporation induces apoptosis and cell cycle arrest in human promyelocytic leukemia cells. Ultrasound Med Biol. 2011;37(12):2149-59.

72. Miller DL, Dou C. Induction of apoptosis in sonoporation and ultrasonic gene transfer. Ultrasound Med Biol. 2009;35(1):144-54.

73. Fan Z, Liu H, Mayer M, Deng CX. Spatiotemporally controlled single cell sonoporation. Proc Natl Acad Sci USA. 2012;109(41):16486-91.

74. Afadzi M, Strand SP, Nilssen EA, Masoy SE, Johansen TF, Hansen R, et al. Mechanisms of the ultrasound-mediated intracellular delivery of liposomes and dextrans. IEEE Trans Ultrason Ferroelectr Freq Control. 2013;60(1):21-33.

75. Zeghimi A, Escoffre JM, Bouakaz A. Role of endocytosis in sonoporation-mediated membrane permeabilization and uptake of small molecules: a electron microscopy study. Phys Biol. 2015;12(6):066007.

76. Yang F, Gu N, Chen D, Xi X, Zhang D, Li Y, et al. Experimental study on cell self-sealing during sonoporation. J Control Release. 2008;131(3):205-10.

77. Wang YX. Superparamagnetic iron oxide based MRI contrast agents: Current status of clinical application. Quant Imaging Med Surg. 2011;1(1):35-40.

78. Yudina A, Lepetit-Coiffe M, Moonen CT. Evaluation of the temporal window for drug delivery following ultrasound-mediated membrane permeability enhancement. Mol Imaging Biol. 2011;13(2):239-49.

79. Lammertink B, Deckers R, Storm G, Moonen C, Bos C. Duration of ultrasound-mediated enhanced plasma membrane permeability. Int J Pharm. 2015;482(1-2):92-8.

80. Hashizume H, Baluk P, Morikawa S, McLean JW, Thurston G, Roberge S, et al. Openings between defective endothelial cells explain tumor vessel leakiness. Am J Pathol. 2000;156(4):1363-80.

81. Clarke PR, Hill CR. Biological action of ultrasound in relation to the cell cycle. Exp Cell Res. 1969;58(2):443-4.

82. Hrazdira I, Skorpikova J, Dolnikova M. Ultrasonically induced alterations of cultured tumour cells. Eur J Ultrasound. 1998;8(1):43-9.

83. Fu YK, Miller MW, Lange CS, Griffiths TD, Kaufman GE. Ultrasound lethality to synchronous and asynchronous Chinese hamster V-79 cells. Ultrasound Med Biol. 1980;6(1):39-46.

84. Abou-Elkacem L, Bachawal SV, Willmann JK. Ultrasound molecular imaging: Moving toward clinical translation. Eur J Radiol. 2015;84(9):1685-93.

85. DeLisser HM, Newman PJ, Albelda SM. Molecular and functional aspects of PECAM-1/CD31. Immunol Today. 1994;15(10):490-5.

86. Smeenge M, Tranquart F, Mannaerts CK, de Reijke TM, van de Vijver MJ, Laguna MP, et al. First-in-Human Ultrasound Molecular Imaging With a VEGFR2-Specific Ultrasound Molecular Contrast Agent (BR55) in Prostate Cancer: A Safety and Feasibility Pilot Study. Invest Radiol. 2017;52(7):419-27.

87. Willmann JK, Bonomo L, Carla Testa A, Rinaldi P, Rindi G, Valluru KS, et al. Ultrasound Molecular Imaging With BR55 in Patients With Breast and Ovarian Lesions: First-in-Human Results. J Clin Oncol. 2017;35(19):2133-40.

4

88. Mast TD. Empirical relationships between acoustic parameters in human soft tissue. Acoust Res Lett Online. 2000;1:37-42.

89. de Jong N, Bouakaz A, Frinking P. Basic acoustic properties of microbubbles. Echocardiography. 2002;19(3):229-40.

90. FDA. Feridex I.V.® label [http://www.fda.gov/ohrms/dockets/ac/05/briefing/2005-4095B1_02_14-FDA-Tab-7-9.pdf]. [http://www.fda.gov/ohrms/dockets/ac/05/briefing/2005-4095B1_02_14-FDA-Tab-7-9.pdf:[Available from:http://www.fda.gov/ohrms/dockets/ac/05/briefing/2005-4095B1_02_14-FDA-Tab-7-9.pdf.

Supporting Information
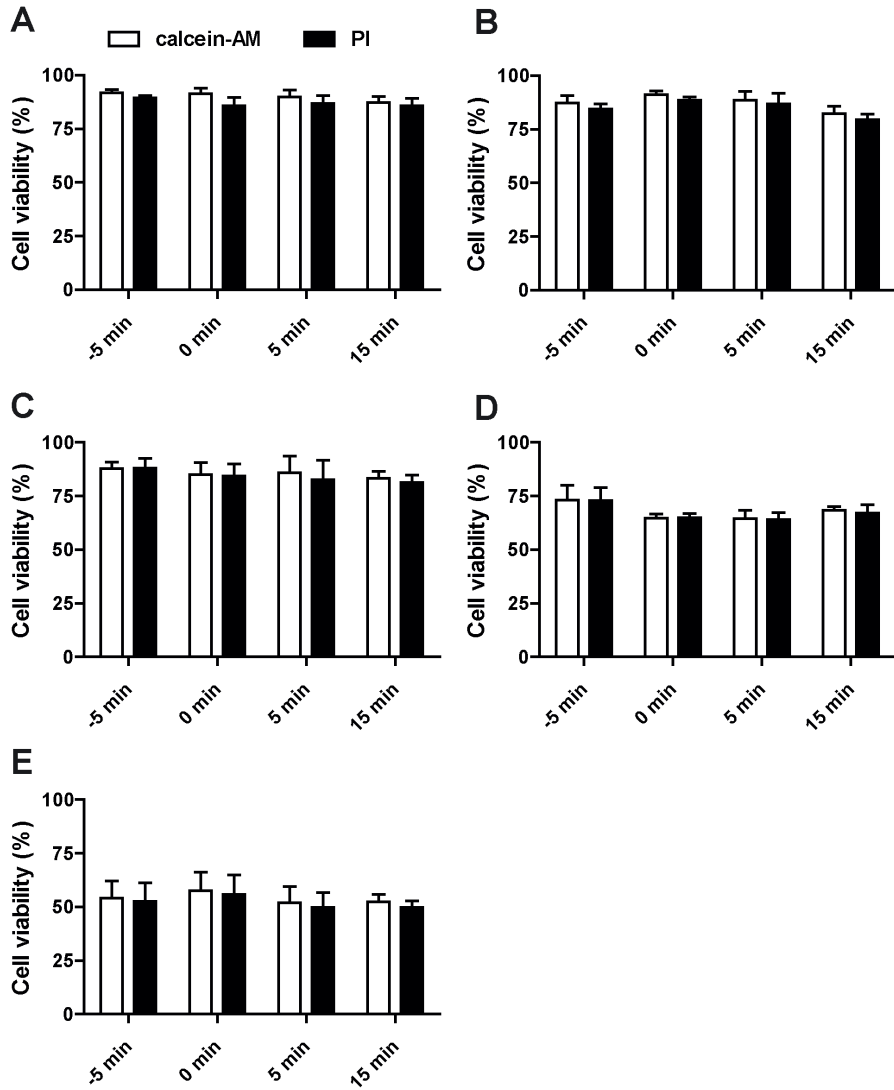
S1 Figure Cell viability determined from calcein-AM versus PI staining. Insonification for 30 s for SPIO added at -5, 0, 5, or 15 min in respect to the start of insonification and incubated for 1 h. The acoustic PNP in **A** was 10 kPa, while this was 20 kPa in **B**, 40 kPa in **C**, 80 kPa in **D**, and 160 kPa in **E**.

5

In vivo stabilized SB3, an attractive GRPR antagonist, for pre- and intra-operative imaging for prostate cancer

Ingrid L. Bakker[1], Sandra T. van Tiel[1], Joost Haeck[1], Gabriela N. Doeswijk[1],
Erik de Blois[1], Marcel Segbers[1], Theodosia Maina[2], Berthold A. Nock[2],
Marion de Jong[1], and Simone U. Dalm[1].

[1] Dept. of Radiology & Nuclear Medicine, Erasmus MC, Rotterdam, The Netherlands
[2] Molecular Radiopharmacy, INSRATES, NCSR "Demokritos", Athens, Greece

Abstract

Purpose
The gastrin releasing peptide receptor (GRPR), overexpressed on various tumor types, is an attractive target for receptor-mediated imaging & therapy. Another interesting approach would be the use of GRPR radioligands for pre-operative imaging and subsequent radio-guided surgery, with the goal to improve surgical outcome. GRPR radioligands were successfully implemented in clinical studies, especially Sarabesin 3 (SB3) is an appealing GRPR antagonist with high receptor affinity. Gallium-68 (^{68}Ga) labelled SB3 has good in vivo stability, after labeling with Indium-111 (^{111}In) however, the molecule shows poor in vivo stability, which negatively impacts tumor targeting capacity. A novel approach to increase in vivo stability of radiopeptides is by co-administration of the neutral endopeptidase (NEP) inhibitor, phosphoramidon (PA). We studied in vivo stability and biodistribution of [^{111}In]SB3 without/with (-/+) PA in mice. Furthermore, SPECT/MRI on a novel, state-of-the-art platform was performed.

Procedures
GRPR-affinity of SB3 was determined on PC295 xenograft sections using [^{125}I] Tyr^4-bombesin with tracer only or with increasing concentrations of SB3. For in vivo stability, mice were injected with 200/2000 pmol [^{111}In]SB3 -/+ 300 μg PA. Blood was collected and analyzed. Biodistribution and SPECT/MRI studies were performed at 1, 4 and 24 h post injection (p.i.) of 2.5 MBq/200 pmol or 25 MBq/200 pmol [^{111}In]SB3 -/+ 300 μg PA in PC-3-xenografted mice.

Results
SB3 showed high affinity for GRPR (IC50: 3.5 nM). Co-administration of PA resulted in twice higher intact peptide in vivo versus [^{111}In]SB3 alone. Biodistribution studies at 1, 4 and 24 h pi. show higher tumor uptake values with PA co-administration (19.7±3.5 vs 10.2±1.5, 17.6±5.1 vs 8.3±1.1, 6.5±3.3 vs 3.1±1.9 %ID/g tissue (P<0.0001)). Tumor imaging with SPECT/MRI clearly improved after co-injection of PA.

Conclusions
Co-administration of PA increased in vivo tumor targeting capacity of [^{111}In] SB3, making this an attractive combination for GRPR-targeted tumor imaging.

5

Introduction

The gastrin releasing peptide receptor (GRPR) is a G-protein coupled receptor overexpressed in a number of cancer types such as prostate cancer, breast cancer and gastrointestinal cancer, thereby representing an attractive molecule for tumor targeting [1, 2]. Multiple GRPR radioligands have been synthesized during the past decade, mainly for the purpose of receptor-mediated nuclear imaging and therapy [3, 4]. These studies, at the preclinical as well as clinical level, have expanded our knowledge on GRPR radioligands and have proven that targeting of GRPR for nuclear imaging and/or therapy can be beneficial in patient care [5-8]. Moreover, research has demonstrated that GRPR antagonists are usually superior to agonists for tumor targeting, in addition to exhibiting less adverse events [9, 10].

Sarabesin 3 (SB3) is a recently developed GRPR antagonist that has excellent receptor affinity and good in vivo stability when labeled with the positron-emitting radionuclide gallium-68 (^{68}Ga; $t_{1/2}$: 68 minutes). Preclinical as well as clinical PET imaging studies using [^{68}Ga]SB3 have been performed with great success [11, 12]. A novel and interesting approach would be the use of SB3 for pre-operative imaging and intra-operative radio-guided tumor detection of GRPR-expressing tumors, especially for the detection of GRPR-expressing metastases and non-palpable tumors.

Radio-guided tumor detection is based on the intra-operative localization of malignant lesions using handheld detection probes following injection of a radiopharmaceutical (Fig. 1). Combining this intra-operative method with information from pre-operative nuclear imaging by single photon emission computed tomography (SPECT) or positron emission tomography (PET), together with computed tomography (CT) or magnetic resonance imaging (MRI), allows for accurate surgical guidance, ultimately improving surgical outcome while minimizing surgical invasiveness [13].

Currently, radio-guided surgery is successfully applied clinically for lymphoscintigraphy in melanoma and breast cancer patients, radio-guided occult lesion localization and radio-guided seed localization of non-palpable tumors, as well as minimal invasive parathyroid surgery for removal of

parathyroid adenomas [14-18]. Multiple radiopharmaceuticals and administration methods are applied for radio-guided surgery amongst which the application of systemically administered radiopharmaceuticals directed against targets that are overexpressed on tumor cells. Examples include ongoing preclinical and (pilot) patient studies evaluating the potential benefits of radio-guided surgery for the detection of neuroendocrine tumor and prostate cancer lesions using somatostatin receptor-targeting and prostate-specific membrane antigen-targeting radiotracers [19-24].

Ideally, for radio-guided surgery, SB3 has to be radiolabeled with a gamma emitter that has a half-life enabling detection of radioactivity prior to surgery and during the full surgical procedure. For this purpose SB3 was therefore labeled with the clinically well-established γ-emitter indium-111 (^{111}In; $t_{1/2}$: 2.8 days). This [^{111}In]SB3 can be used for SPECT/MRI, which offers the opportunity to combine sensitive functional imaging by SPECT with high-resolution anatomical/functional imaging by MRI. Compared to commonly used CT, MRI has a number of advantages such as improved soft tissue contrast and the added value of multiparametric imaging, which may lead to better tumor localization.

[^{111}In]SB3 has poor in vivo stability, ultimately resulting in low tumor uptake [25]. An explanation for the poor in vivo stability is degradation of the peptide by naturally occurring enzymes in vivo, such as the neutral endopeptidase (NEP), which cleaves peptides at the amino side of hydrophobic residues [26, 27]. To increase the in vivo stability of radiopeptides multiple solutions are available, including structural modifications of a peptide or the novel approach of inhibition of enzymes responsible for enzymatic degradation. Since structural modifications are time-consuming, and may have a negative impact on the binding affinity or biodistribution profile of the peptide, the latter solution is very attractive. Co-administration of the NEP inhibitor phosphoramidon (PA) enhanced the in vivo stability and thereby the tumor targeting capacity of multiple radiotracers [5, 26, 28-30]. The aim of our study is to evaluate whether we can also improve tumor targeting of [^{111}In]SB3 by co-administration of PA to potentially use the radiotracer for pre-operative SPECT/MRI and ultimately for intra-operative radio-guided tumor detection of GRPR-expressing tumors and/or metastases as well. For this we compared

the in vivo stability and the biodistribution of [^{111}In]SB3 without/with (-/+) PA, the latter by performing both biodistribution and SPECT/MRI studies in mice bearing GRPR-expressing PC-3 tumor xenografts.

Materials and Methods

Radiolabeling

SB3 (Fig. 2) was radiolabeled with ^{111}In (Covidien) as previously described [31]. Small volume reactions were performed in conical vials. Sodium acetate was used to control pH, resulting in a final pH value of 4-4.5 and quenchers (ascorbic- and gentisic acid 3.5 mM and methionine 10 mM as final concentration) were added to prevent radiolysis. A mixture of 1 nmol SB3 and 125 MBq equivalent ^{111}InCl$_3$ and quenchers in a final volume of 140 µL were heated for 15 min at 80°C. To complex non-incorporated ^{111}In, after cooling down to room temperature, 5 µL of 4 mM DTPA was added. To obtain a molar activity of 12.5 MBq/nmol, after the labelling 9 nmoles of SB3 was added. The incorporation was determined by instant thin layer chromatography (ITLC) silica gel using sodium citrate (0.1 M, pH 5) as solvent [32] and radiochemical purity (RPC) was measured by a HPLC system (Breeze, Waters), containing a 2690 quaternary pump, and radioactivity was monitored with a NaI detector, digital multichannel analyzer and dedicated software (MetorX B.V). A Symmetry C$_{18}$ column (5 µm x 4.6 mm x 250 mm, Waters) was used with a gradient profile of: 0–5 min 100% A, 5-5.01 min 60% B, 5.01–20 min 80% B, 20–20.01 min 100% B, 20.01–25 min 100% B, 25.01–30 min (flow 1 mL/min), where A was 0.1% trifluoroacetic acid (TFA) in H$_2$O and B was LC-MS grade methanol. No further purification was required.

A molar activity of 12.5 MBq/nmol and 125 MBq/nmol was used for the biodistribution and SPECT/MRI studies, respectively. For the in vivo stability studies both molar activities were used. To determine the affinity of SB3 for the human GRPR in a competition-binding assay, Tyr^4-Bombesin (Sigma-Aldrich) was radiolabeled with iodine-125 (^{125}I) based on the Iodo Beads® (Pierce) method, adapted with 5 min pre-incubation before addition of the peptide, as previously described [33, 34]. In short, 100 µL of PBS 50 mM Pi pH 7.5, sodium iodide solution (10-20 MBq Na^{125}I in 0.01 M NaOH) and pre-rinsed Iodo Beads® were pre-incubated for 5 min, and Iodo Beads® were removed. Then,
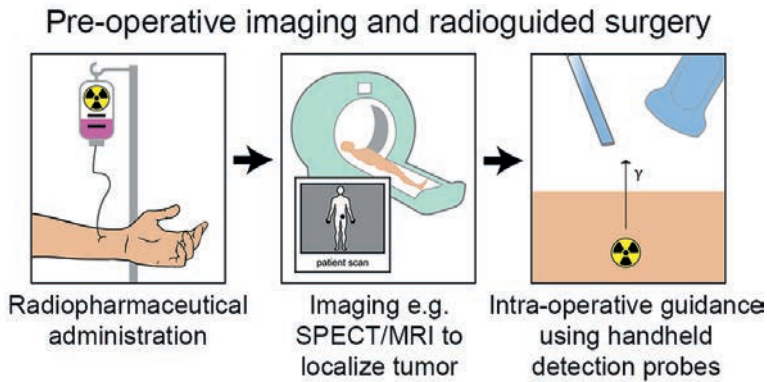
Figure 1 The concept of radio-guided surgery: **A** Radiopharmaceuticals directed at tumor cells are administered to the patient followed by accumulation of radioactivity in these cells over time. **B** Subsequently, full body nuclear imaging is performed, e.g. SPECT/MRI, to localize the tumor pre-operatively. **C** Using this information the patient is operated for removal of the tumor. Intra-operatively a handheld device is used to detect radioactivity derived from the tumor cells to guide the surgeon towards the tumor.

5
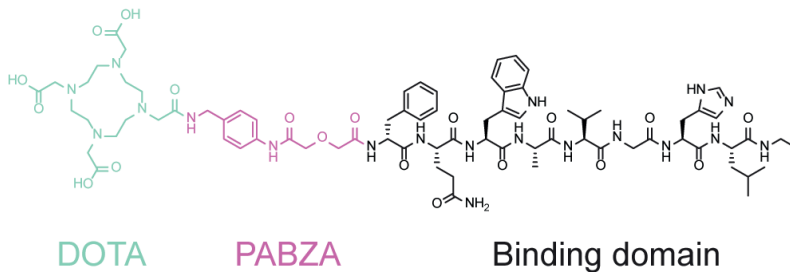
Figure 2 Structure of SB3.

total volume was added to 70 nmol of peptide in PBS, and the mixture was allowed to react for 5 min at room temperature. To exclude non-labeled iodine, a purification was performed by solid phase extraction using a J.T. Baker C_{18} cartridge followed by HPLC purification [34].

Internalization studies

Internalization with [^{111}In]SB3 was performed in PC-3 cells, a commonly used human derived androgen independent GRPR-expressing PC cell line (AACR). The cells were seeded in six-well plates at a density of 0.6×10^6 cells per well and cultured overnight. On the day of the experiment cells were washed twice with 37°C PBS. Fresh internalization medium, RPMI + Glutamax with 20mM HEPES

and 1% Bovine Serum Albumin fraction V pH 7.4, 10^{-9} M [^{111}In]SB3 was added. The cells were incubated at 37℃ in triplicates for 60 minutes, incubation was stopped by removal of the medium and rinsing with cold PBS twice. Thereafter, the cells were incubated for 10 minutes with acid wash buffer (50 mM Glycin-HCl/100 mM NaCl, pH 2.8). The supernatant was collected (membrane fraction), the cells were rinsed with acid wash buffer and collected in the same tube. Cells were lysed with 0.1 M NaOH and collected in another tube (internalized cell fraction). The amount of activity in the membrane- and cell fraction was measured on an automatic gamma counter.

Animal model

Healthy or xenografted Balb c nu/nu male mice (Janvier) were used in this study. To obtain xenografted mice, animals were injected subcutaneously in the right shoulder with PC-3, 3×10^6 cells in Matrigel (total volume: 150 μL, solution: 66% RPMI, 33% Matrigel) per animal. Prior to tumor cell inoculation the PC-3 cells were cultured in RPMI medium supplemented with 10% fetal bovine serum, 5,000 IU/mL penicillin and 5,000 μg/mL streptomycin at 37 ℃ in a humidified atmosphere containing 5% CO_2. PC295 is an androgen-dependent patient derived cell line with high GRPR-expression. Xenografts were generated by subcutaneous implantation of the PC295 human prostate tumor as previously described and were stored at -80℃ until further use [35]. All culture supplies were purchased at Gibco.

Competition binding assay

For the competition binding assay, fresh frozen PC295 xenograft tissue slices (10 μm) were incubated in triplicate with 80 μL 5×10^{-10} M [^{125}I]Tyr^4-Bombesin, with tracer only or with an increasing concentration (10^{-12} to 10^{-6} M) of unlabeled SB3 for 1 h and exposed to super resolution phosphor screens (PerkinElmer) for 48 h. The phosphor screens were read using the Cyclone (PerkinElmer) and quantified using OptiQuant software. Binding of unblocked [^{125}I]Tyr^4-bombesin to the tissue slices was set at 100% and the percentage of binding relative to the unblocked tissue sample was calculated for the blocked tissue sections. These values were used to determine the IC$_{50}$ value of unlabeled SB3.

Stability studies

To determine the stability of [^{111}In]SB3 -/+ PA in vivo, healthy mice (n = 3 per group) were intravenously injected with 200 pmol/25 MBq or 2000 pmol/25 MBq [^{111}In]SB3 (volume: 100 µL), co-injected with either 300 µg/100 µL PA (Peptides International Inc) in 0.5% ethanol or 100 µL saline solution. Five minutes after injection of [^{111}In]SB3 -/+PA, blood (0.5 – 1 mL) was collected by cardiac puncture, while animals were under isoflurane/O$_2$ anesthesia, and transferred to blood-collection tubes containing 90 USP units of lithium heparin (spray coated), HPLC grade ethanol was added in a 1:1 (v/v) ratio, and the tubes were placed on ice. Blood samples were centrifuged 5 minutes at 1250 G, and supernatant was collected. Next the collected supernatant was centrifuged again for 5 minutes at 12500 G. The secondary supernatant was collected and diluted with MilliQ down to <25% ethanol before injection on HPLC. The samples were analyzed by HPLC (Alliance, Waters) including a Symmetry C$_{18}$ column (5 µm × 4.6 mm × 250 mm). Elution was performed in a 1 mL/min flow, completed in 30 min, with the gradient: 0–5 min 100% A, 5–5.01min 40% A 60% B, 5.01–20 min 20% A 80% B, 20–20.01min 100% B, 20.01–25min 100% B, 25.01–30 min 100% A, where A was 0.1% TFA in H$_2$O and B was methanol. In one animal the sample volume was too low for further analysis, this animal was therefore excluded.

Biodistribution studies

Tumor-bearing mice received an intravenous injection of 200 pmol/2.5 MBq [^{111}In]SB3, co-injected with either 300 µg/100 µL PA in 0.5% ethanol or 100 µL saline solution (n = 4 animals per group for each time point). In previous in vivo studies 200 pmol appeared to be the optimal peptide amount (regarding uptake in tumor and pancreas, data not shown). To determine specificity of tumor and organ uptake blocking experiments were performed; an additional group of animals (n = 3) was pre-injected with an excess (20 nmol) of unlabeled SB3 followed by injection of the radiotracer -/+ PA. At 3 different time points p.i. (1 h, 4 h and 24 h) animals were euthanized and blood, organs and tumors were collected, weighed and measured in a γ-counter (1480 WIZARD automatic γ-counter, Perkin Elmer). For γ-counter measurements an isotope specific energy window, a counting time of 60 sec and a counting error ≤ 5% was used. Results were expressed as the percentage of the injected dose per gram tissue (%ID/g tissue). Animals that had ≥ 7% ID in the tail were excluded.

SPECT/MRI

For SPECT/MRI, PC-3-xenografted mice were intravenously injected with 25 MBq/200 pmol [^{111}In]SB3, co-injected with either 300 μg/100 μL PA in 0.5% ethanol or 100 μL saline solution. Subsequently, imaging was performed 1 h, 4 h and 24 h p.i. of the radiotracer, while animals were anesthetized using isoflurane/O$_2$, body temperature was maintained using warm air flow and respiratory rate was monitored. Whole body SPECT images were acquired using the novel and state-of-the-art 4-head multipinhole system (NanoScan SPECT/MRI, Mediso Medical Imaging) in 30 min (28 projections, 29 s/projection and 7 cm axial field of view). Images were reconstructed using OSEM with 6 iterations and 4 subsets on a 120 × 120 matrix with 0.25 × 0.25 × 0.25 mm isotropic voxels. MR based attenuation correction was applied to all images. T2 MR images were acquired using a spin echo sequence (TR/TE=4500/52 ms) with a 35 mm diameter solenoid coil. Other scan parameters were: field of view: 70 mm, matrix: 256 × 128 and slice thickness: 1 mm with 0.1 mm spacing between slices. An ROI of the tumor was drawn by an experienced technician on the T2-weighted MR image to measure the intensity in the SPECT image.

Statistics

All statistical evaluations were performed with Graphpad Prism software (v 5.01). The IC$_{50}$ value was calculated using a log (inhibitor) vs response model. To compare in vivo stability -/+ PA, radioactivity uptake in the tumor -/+ PA and radioactivity uptake in the tumor without and with an excess of unlabeled peptide an unpaired t-test was used. P values <0.05 were considered statistically significant. Tumor to organ uptake ratios were calculated per animal and expressed as mean and standard deviation per group.

Results

Radiolabeling
The RCP and radiometal incorporation were both >90%.

Internalization studies
In internalization experiments with [^{111}In]SB3 in PC-3 cells, the membrane faction contained almost 4 times more radioactivity compared to the cell faction.

Competition binding assay
Quantified binding of [^{125}I]Tyr^4-bombesin to PC259 tissue sections without and with increasing concentrations of unlabeled SB3 resulted in an IC$_{50}$ value of 3.5 nM (95% CI: 1.9 nM to 6.4 nM) (Fig. 3).

5
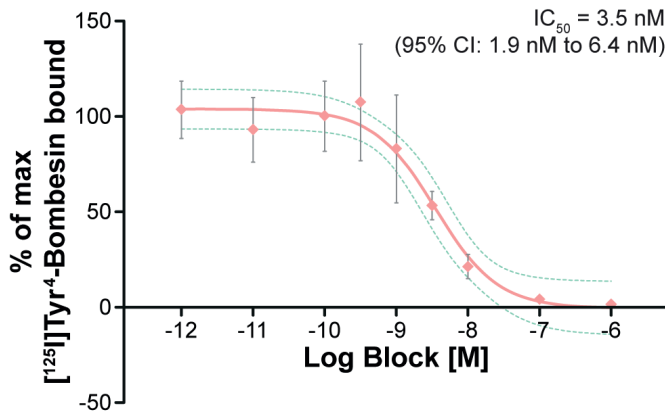
Figure 3 Competitive binding assay using [125I]Tyr4-bombesin blocked with increasing concentrations of unlabeled SB3. 95% CI is shown in green.

Stability studies
In vivo stability of [^{111}In]SB3 -/+ PA was analyzed in blood samples, collected 5 min p.i. In the animals receiving 200 pmol [^{111}In]SB3 37.3±2.5 % of the remaining circulating activity consisted of intact radiotracer, while this value significantly increased (P<0.0001) to 86.7±1.5 % when [^{111}In]SB3 was co-injected with PA (Fig. 4 A+B). When a 10× higher peptide amount was administered, these values were 42.0±0.2 % vs 87.9±1.1 % (P<0.0001) of the radiotracer still being

intact in the blood, respectively (Fig. 4 C+D), indicating a clear increase of stability even with 2000 pmol peptide.

Biodistribution studies

The results of the biodistribution studies are displayed in Fig. 5. A maximum tumor uptake of 10.2±1.5 %ID/g tissue was reached using 2.5 MBq/200 pmol [^{111}In]SB3 1 h p.i. in contrast to 19.7±3.5 % ID/g tissue after injection of [^{111}In] SB3 + PA. At all studied time points, there was significantly higher (P<0.0001) tumor uptake when PA was co-administered with [^{111}In]SB3. Next to tumor uptake, high radiotracer uptake was also observed in the GRPR-expressing pancreas and in the kidneys, the latter as a result of renal excretion and partial reabsorption of the radiopeptide. The increased in vivo stability of [^{111}In]SB3 + PA also resulted in an increase in pancreatic uptake (4.1±2.3 vs 10.1±4.3 %ID/g tissue 1 h p.i. -/+ PA, respectively), while renal uptake remained similar (3.9±1.4 vs 4.5±1.4 %ID/g tissue 1 h p.i. -/+ PA, respectively). At 4 h and 24 h p.i. the same pattern was observed. A similar tumor to pancreas radioactivity ratio was found for [^{111}In]SB3 +/- PA (3.4±2.5 vs 2.2±0.8, 1 h p.i. -/+ PA, respectively). The tumor to kidney ratio was more favorable however when the radiotracer was combined with PA (2.8±1.0 vs 4.8±2.2, 1 h p.i. -/+ PA respectively). Also, radiotracer uptake in the pancreas and the tumor was receptor-specific as can be concluded from the significantly decreased (P≤0.001) uptake when an excess of unlabeled SB3 was co-administered.

SPECT/MRI

In line with the biodistribution studies, SPECT/MR imaging performed 1 h, 4 h and 24 h p.i. of 25 MBq/200 pmol [^{111}In]SB3 +/- PA resulted in clearly improved tumor visualization when the radiotracer was combined with PA, at all imaging time points (Fig. 6 A). ROI analysis showed an increase of 70% in signal intensity (1424 vs 2434 kBq/mL) 1 h p.i. of [^{111}In]SB3 only and [^{111}In]SB3 + PA, respectively. Intensity curves and the biodistribution time activity curves were normalized to 100% at 1 h for the + PA group. The normalized curves obtained from SPECT/MR images and biodistribution studies showed a well-comparable pattern for the tumor radioactivity (Fig. 6 B).
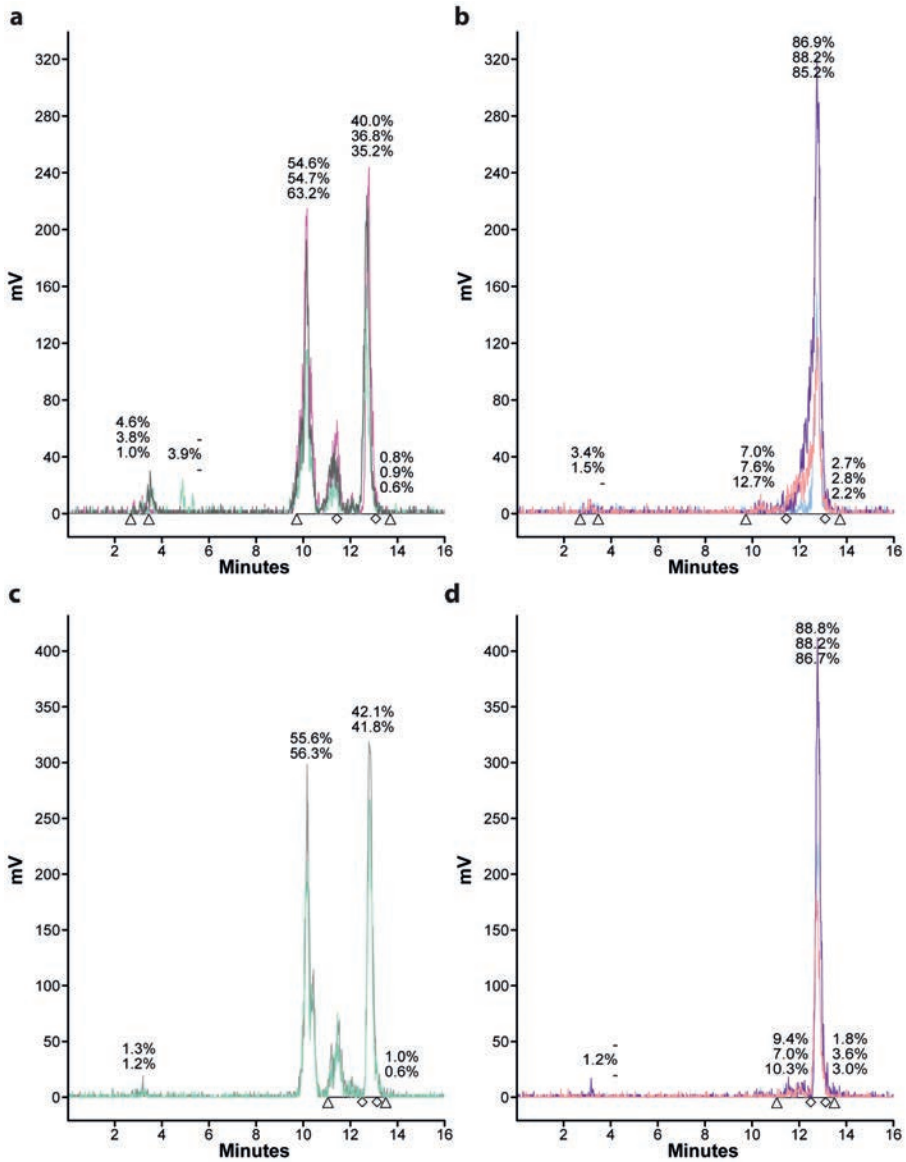
Figure 4 *In vivo* stability of [111In]SB3. HPLC analysis of extracted radioactivity from blood 5 min p.i. of a low peptide amount (200 pmol/25 MBq) either **a** in the absence of PA or **b** in the presence of PA, and 5 min p.i. with a high peptide amount (2000 pmol/25 MBq) either **c** in the absence or **c** in the presence of PA. - = peak is missing.
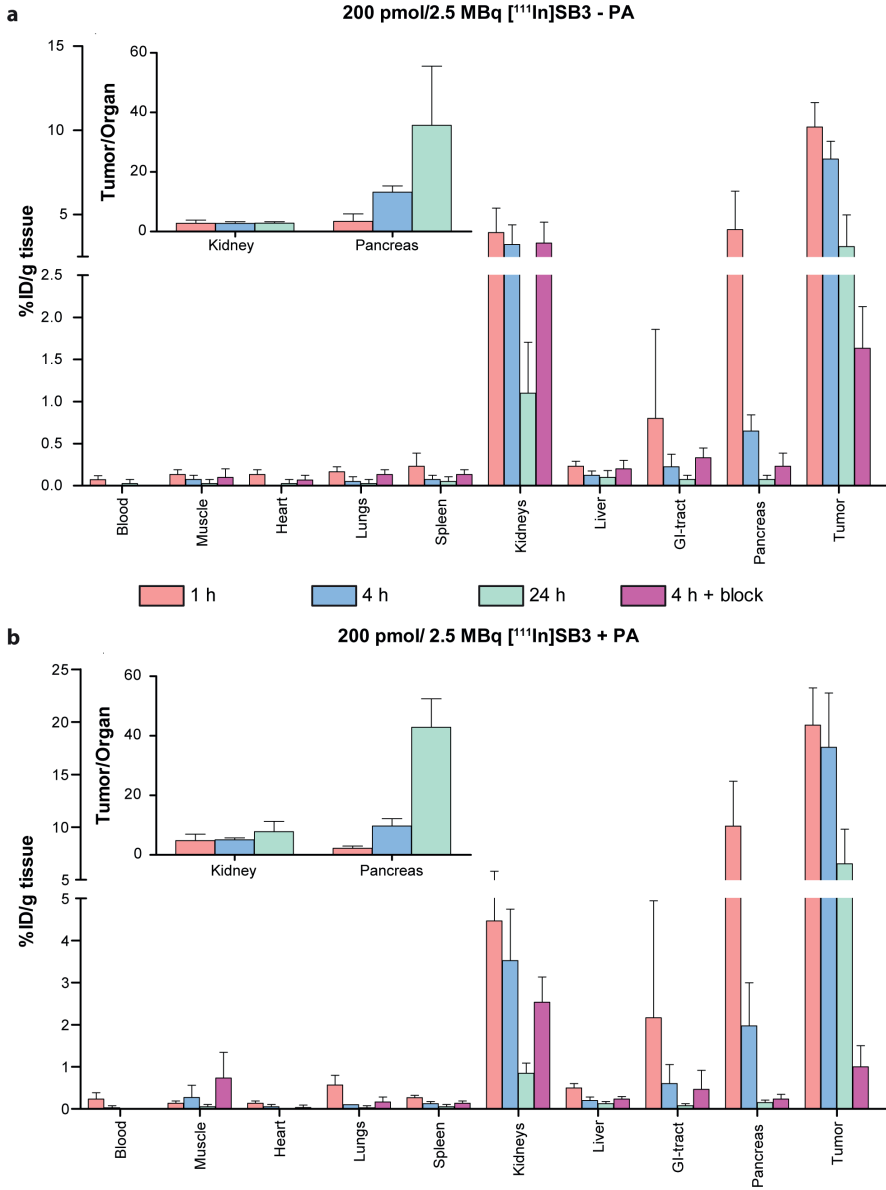
Figure 5 Blood, organ and tumor uptake of [111In]SB3 **a** administered without PA and **b** with PA. Tumor to kidney and tumor to pancreas ratios are displayed in the insets of graphs of **a** and **b**.
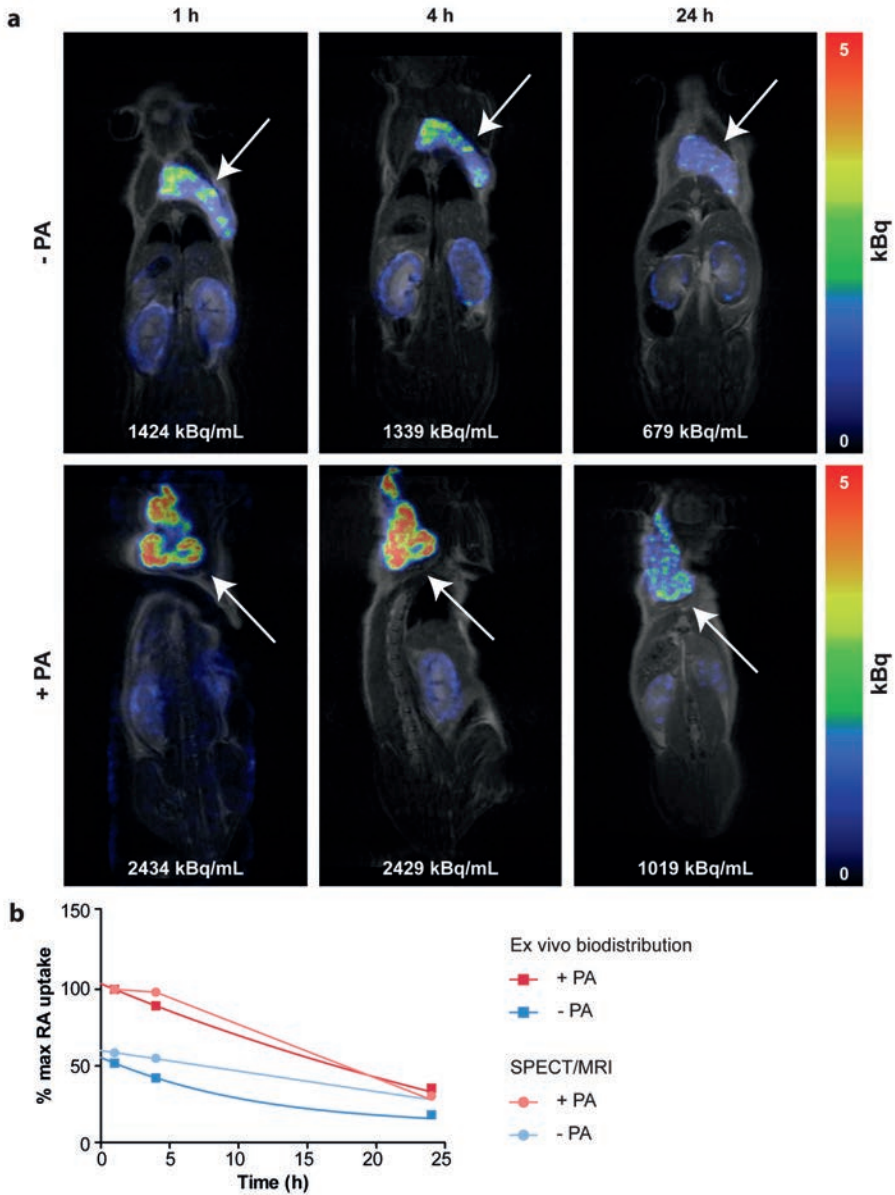
Figure 6 a SPECT/MRI 25 MBq/200 pmol [111In]SB3 without (top panel) and with (bottom panel) co-administration of PA. The arrows indicate the tumor. **b** Time activity curve of radioactivity uptake in PC-3 xenografts obtained by *ex vivo* biodistribution (200 pmol/2.5 MBq/mouse) and by ROI analysis on SPECT/MRI (200 pmol/25 MBq/mouse).

Discussion

The GRPR is overexpressed at high incidence and high density on various tumors, including prostate cancer, making it an appealing molecule for tumor targeting [2]. Over time multiple and promising GRPR targeting radiotracers have been developed, mostly for nuclear imaging and therapeutic purposes. Another interesting approach would be the application of GRPR radioligands for radio-guided surgery since handheld probes and cameras can be used to detect radioactive decay intra-operatively. For GRPR-targeting to be successful, the radiotracer applied should have good in vivo stability, good receptor affinity and favorable pharmacokinetic properties.

In this study we evaluated whether co-administration of the NEP inhibitor PA with [^{111}In]SB3, a radiolabeled GRPR antagonist, leading to in vivo stabilization of the radioligand, would improve the application use of the radiopharmaceutical for pre-operative SPECT/MRI, and the future use of peri-operative scintigraphy and radio-guided surgery. Currently MRI is the most powerful imaging tool for prostate cancer, among other factors because of its high soft-tissue contrast and high resolution [36, 37]. Combining MRI with sensitive and specific targeted nuclear imaging by SPECT potentially improves tumor detection.

Thereto, we performed in vivo stability studies, biodistribution studies and SPECT/MR imaging in healthy mice and mice subcutaneously xenografted with the GRPR-expressing prostate cancer cell line PC-3. Prior to this we confirmed a considerable higher membrane binding compared to internalized fraction of [^{111}In]SB3 as expected for a receptor antagonist. Also we determined the receptor affinity of the unlabeled compound on tissue slices of xenografts generated from the human prostate tumor PC295, confirming previous reported affinities of unlabeled SB3 and ^{nat}In labeled SB3 in the low nanomolar range [25]. This data showed that SB3 had excellent affinity for the GRPR, confirming previous findings [11].

In vivo stability studies 5 min p.i. of [^{111}In]SB3 -/+ PA in healthy mice, showed twice as much intact radiopeptide in the blood when PA was co-administered, similar to what has been reported for other radiopeptides [5,

28, 29]. The large amount of unlabeled compound might hamper formation and detection of radiometabolites, so caution is advised when comparing the results of the low and high peptide amounts. However, even when using a high amount of peptide a clear effect of PA was still observed.

The metabolic susceptibility of peptides can be influenced by a multitude of characteristics. Next to the peptide structure, also charge and configuration can play a role. The most well-known approach to protect peptides against degradation is modify the peptide, e.g. by stabilizing peptide bonds. It was found that specific changes of the C-terminal structure of peptide gastrin releasing peptide analogues resulted in receptor antagonists with improved potency and stability [38]. Previously it has been reported that charge, peptide chain length, choice of linker, etc can all, have large effects on metabolic stability and pharmacokinetics of GRP ligands [39, 40].

Concerning the biodistribution studies, stabilization of [111In]SB3 by inhibition of NEP, resulted in higher tumor uptake. Next to higher tumor uptake, high uptake of the radiotracer was also observed in the pancreas. Even though the radiopeptide uptake in the pancreas increased when [111In]SB3 was co-administered with PA, the tumor to pancreas ratio remained unaffected. Nevertheless, this high uptake in the pancreas should be kept in mind when the radiotracer would be used for radio-guided surgery of lesions close to the pancreas. In this case the surgeon should carefully evaluate whether the signal measured by a gamma detection probe and/or a handheld gamma camera is derived from tumor lesions or neighboring healthy tissue. However, as can be seen from the biodistribution data, radioactivity washout from the pancreas was relatively fast, while tumor radioactivity uptake declined at a lower rate. This was also observed in previously published studies [11, 41-43]. So, determining the time window with optimal tumor/pancreas ratio is required for optimal pre-operative and intra-operative tumor detection. In this respect, the uptake in the kidneys and the bladder due to renal excretion of the radiotracer should also be taken into account.

An interesting next step would be to modify the peptide to create a molecule that can serve both as radioactivity- and fluorescence-carrier. Even though radio-guided surgery is profitable, it has limitations. So, the use of radiotracers

5

allows for gross tumor localization by detection of γ-photons outside of the body, but this method is not suited for accurate tumor delineation during surgery [44]. On the other hand, fluorescence imaging is limited by the penetration depth of fluorescent light, which can only be detected when at close distance. However, fluorescence imaging does allow exact tumor delineation and can provide real-time intra-operative visualization [44]. Combining the strengths of radio-guided and fluorescence guided surgery can therefore be of benefit.

SPECT/MR imaging resulted in successful identification of tumor lesions on scans and, as expected, higher radioactivity uptake was visualized when [^{111}In] SB3 was co-administered with PA. Time activity curves obtained with ex vivo biodistribution studies and ROI analysis on SPECT/MR images demonstrated similar patterns, indicating the SPECT/MRI platform to correctly depict the pharmacokinetics of the radiotracer.

With respect to the commercially available NEP inhibitor PA, to date preclinical studies evaluating its potential in potentiating the use of radiotracers have not indicated any adverse events [5, 28]. For application in patients NEP inhibitors that are already approved for clinical use such as Sacubitril and Racecadotril might be applied [45].

Furthermore, depending on the cancer type for which [^{111}In]SB3 + PA will be used for tumor detection pre- and intra-operatively, the application should be compared to that using other radiotracers under investigation or applied for similar purposes, e.g. lymphoscintigraphy for sentinel lymph node biopsy in breast cancer patients and PSMA radio-guided surgery in prostate cancer patients [21, 46].

Conclusions

Co-administration of [¹¹¹In]SB3 with the NEP inhibitor PA, led to a significant increase of in vivo stability of [¹¹¹In]SB3. So, SPECT/MRI using [¹¹¹In]SB3 + PA resulted in excellent visualization of tumors in our preclinical model, indicating its potency for (pre-operative) imaging and future radio-guided surgery applications.

Acknowledgments

5

Disclosures

The authors declare that they have no conflict of interest. All applicable institutional and/or national guidelines for the care and use of animals were followed.

References

1. Jensen RT, Battey JF, Spindel ER, Benya RV (2008) International Union of Pharmacology. LXVIII. Mammalian bombesin receptors: nomenclature, distribution, pharmacology, signaling, and functions in normal and disease states. Pharmacol Rev 60:1-42.

2. Reubi JC, Wenger S, Schmuckli-Maurer J, Schaer JC, Gugger M (2002) Bombesin receptor subtypes in human cancers: detection with the universal radioligand (125)I-[D-TYR(6), beta-ALA(11), PHE(13), NLE(14)] bombesin(6-14). Clin Cancer Res 8:1139-1146.

3. Sancho V, Di Florio A, Moody TW, Jensen RT (2011) Bombesin receptor-mediated imaging and cytotoxicity: review and current status. Curr Drug Deliv 8:79-134.

4. Moreno P, Ramos-Alvarez I, Moody TW, Jensen RT (2016) Bombesin related peptides/receptors and their promising therapeutic roles in cancer imaging, targeting and treatment. Expert Opin Ther Targets 20:1055-1073.

5. Chatalic KL, Konijnenberg M, Nonnekens J, et al (2016) In Vivo Stabilization of a Gastrin-Releasing Peptide Receptor Antagonist Enhances PET Imaging and Radionuclide Therapy of Prostate Cancer in Preclinical Studies. Theranostics 6:104-117.

6. Dumont RA, Tamma M, Braun F, et al (2013) Targeted radiotherapy of prostate cancer with a gastrin-releasing peptide receptor antagonist is effective as monotherapy and in combination with rapamycin. J Nucl Med 54:762-769.

7. Nock BA, Kaloudi A, Lymperis E, et al (2017) Theranostic Perspectives in Prostate Cancer with the Gastrin-Releasing Peptide Receptor Antagonist NeoBOMB1: Preclinical and First Clinical Results. J Nucl Med 58:75-80.

8. Stoykow C, Erbes T, Maecke HR, et al (2016) Gastrin-releasing Peptide Receptor Imaging in Breast Cancer Using the Receptor Antagonist (68)Ga-RM2 And PET. Theranostics 6:1641-1650.

9. Bodei L, Ferrari M, Nunn A, et al (2007) 177Lu-AMBA bombesin analogue in hormone refractory prostate cancer patients: a phase I escalation study with single-cycle administrations [abstract]. Eur J Nucl Med Mol Imaging 34 (Supplement 2):S221.

10. Cescato R, Maina T, Nock B, et al (2008) Bombesin receptor antagonists may be preferable to agonists for tumor targeting. J Nucl Med 49:318-326.

11. Maina T, Bergsma H, Kulkarni HR, et al (2016) Preclinical and first clinical experience with the gastrin-releasing peptide receptor-antagonist [(6)(8)Ga]SB3 and PET/CT. Eur J Nucl Med Mol Imaging 43:964-973.

12. Bakker I, Fröberg AC, Busstra MB, et al (2016) PET imaging of prostate cancer using the GRPr-targeting ligand Sarabesin 3 prior to radical prostatectomy [abstract]. Eur J Nucl Med Mol Imaging 43 (Supplement 1):S1-S734.

13. Povoski SP, Neff RL, Mojzisik CM, et al (2009) A comprehensive overview of radioguided surgery using gamma detection probe technology. World J Surg Oncol 7:11.

14. Bluemel C, Herrmann K, Giammarile F, et al (2015) EANM practice guidelines for lymphoscintigraphy and sentinel lymph node biopsy in melanoma. Eur J Nucl Med Mol Imaging 42:1750-1766.

15. Giammarile F, Bozkurt MF, Cibula D, et al (2014) The EANM clinical and technical guidelines for lymphoscintigraphy and sentinel node localization in gynaecological cancers. Eur J Nucl Med Mol Imaging 41:1463-1477.

16. Valdes Olmos RA, Vidal-Sicart S, Manca G, et al (2017) Advances in radioguided surgery in oncology. Q J Nucl Med Mol Imaging 61:247-270.

17. Desiato V, Melis M, Amato B, et al (2016) Minimally invasive radioguided parathyroid surgery: A literature review. Int J Surg 28 (Supplement 1):S84-93.

18. Chan BK, Wiseberg-Firtell JA, Jois RH, Jensen K, Audisio RA (2015) Localization techniques for guided surgical excision of non-palpable breast lesions. Cochrane Database Syst Rev 12:CD009206.

19. Cuccurullo V, Di Stasio GD, Mansi L (2017) Radioguided surgery with radiolabeled somatostatin analogs: not only in GEP-NETs. Nucl Med Rev Cent East Eur 20:49-56.

20. Adams S, Baum RP (2000) Intraoperative use of gamma-detecting probes to localize neuroendocrine tumors. Q J Nucl Med 44:59-67.

21. Rauscher I, Eiber M, Maurer T (2017) [PSMA-Radioguided Surgery for Salvage Lymphadenectomy in Recurrent Prostate Cancer] 111In-PSMA-radioguided surgery beim oligometastasierten Prostatakarzinomrezidiv. Aktuelle Urol 48:148-152.

22. Robu S, Schottelius M, Eiber M, et al (2017) Preclinical Evaluation and First Patient Application of 99mTc-PSMA-I&S for SPECT Imaging and Radioguided Surgery in Prostate Cancer. J Nucl Med 58:235-242.

23. Schottelius M, Wirtz M, Eiber M, Maurer T, Wester HJ (2015) [(111)In]PSMA-I&T: expanding the spectrum of PSMA-I&T applications towards SPECT and radioguided surgery. EJNMMI Res 5:68.

24. Maurer T, Weirich G, Schottelius M, et al (2015) Prostate-specific membrane antigen-radioguided surgery for metastatic lymph nodes in prostate cancer. Eur Urol 68:530-534.

25. Lymperis E, Maina-Nock T, Kaloudi A, Krenning EP, De Jong M, Nock BA (2014) Transient in vivo NEP inhibition enhances the theranostic potential of the new GRPR-antagonist [111In/177Lu]SB3 [abstract]. Eur J Nucl Med 41 (Supplement 2):S319.

26. Nock BA, Maina T, Krenning EP, de Jong M (2014) "To serve and protect": enzyme inhibitors as radiopeptide escorts promote tumor targeting. J Nucl Med 55:121-127.

27. Roques BP, Noble F, Dauge V, Fournie-Zaluski MC, Beaumont A (1993) Neutral endopeptidase 24.11: structure, inhibition, and experimental and clinical pharmacology. Pharmacol Rev 45:87-146.

28. Marsouvanidis PJ, Melis M, de Blois E, et al (2014) In vivo enzyme inhibition improves the targeting of [177Lu]DOTA-GRP(13-27) in GRPR-positive tumors in mice. Cancer Biother Radiopharm 29:359-367.

29. Maina T, Kaloudi A, Valverde IE, Mindt TL, Nock BA (2017) Amide-to-triazole switch vs. in vivo NEP-inhibition approaches to promote radiopeptide targeting of GRPR-positive tumors. Nucl Med Biol 52:57-62.

30. Suda H, Aoyagi T, Takeuchi T, Umezawa H (1973) Letter: A thermolysin inhibitor produced by Actinomycetes: phospholamidon. J Antibiot (Tokyo) 26:621-623.

31. de Blois E, Chan HS, Konijnenberg M, de Zanger R, Breeman WA (2012) Effectiveness of quenchers to reduce radiolysis of (111)In- or (177)Lu-labelled methionine-containing regulatory peptides. Maintaining radiochemical purity as measured by HPLC. Curr Top Med Chem 12:2677-2685.

32. Bakker WH, Albert R, Bruns C, et al (1991) [111In-DTPA-D-Phe1]-octreotide, a potential radiopharmaceutical for imaging of somatostatin receptor-positive tumors: synthesis, radiolabeling and in vitro validation. Life Sci 49:1583-1591.

33. Bakker WH, Krenning EP, Breeman WA, et al (1990) Receptor scintigraphy with a radioiodinated somatostatin analogue: radiolabeling, purification, biologic activity, and in vivo application in animals. J Nucl Med 31:1501-1509.

34. de Blois E, Chan HS, Breeman WA (2012) Iodination and stability of somatostatin analogues: comparison of iodination techniques. A practical overview. Curr Top Med Chem 12:2668-2676.

35. van Weerden WM, de Ridder CM, Verdaasdonk CL, et al (1996) Development of seven new human prostate tumor xenograft models and their histopathological characterization. Am J Pathol 149:1055-1062.

36. Guneyli S, Erdem CZ, Erdem LO (2016) Magnetic resonance imaging of prostate cancer. Clin Imaging 40:601-609.

37. Futterer JJ, Briganti A, De Visschere P, et al (2015) Can Clinically Significant Prostate Cancer Be Detected with Multiparametric Magnetic Resonance Imaging? A Systematic Review of the Literature. Eur Urol 68:1045-1053.

38. Heimbrook DC, Saari WS, Balishin NL, et al (1991) Gastrin releasing peptide antagonists with improved potency and stability. J Med Chem 34:2102-2107.

39. Marsouvanidis PJ, Maina T, Sallegger W, Krenning EP, de Jong M, Nock BA (2013) Tumor diagnosis with new 111In-radioligands based on truncated human gastrin releasing peptide sequences: synthesis and preclinical comparison. J Med Chem 56:8579-8587.

40. Kaloudi A, Nock BA, Lymperis E, Krenning EP, de Jong M, Maina T (2016) (99m)Tc-labeled gastrins of varying peptide chain length: Distinct impact of NEP/ACE-inhibition on stability and tumor uptake in mice. Nucl Med Biol 43:347-354.

5

41. Dalm SU, Bakker IL, de Blois E, et al (2017) 68Ga/177Lu-NeoBOMB1, a Novel Radiolabeled GRPR Antagonist for Theranostic Use in Oncology. J Nucl Med 58:293-299.

42. Mansour N, Paquette M, Ait-Mohand S, Dumulon-Perreault V, Guerin B (2018) Evaluation of a novel GRPR antagonist for prostate cancer PET imaging: [(64)Cu]-DOTHA2-PEG-RM26. Nucl Med Biol 56:31-38.

43. Mansi R, Wang X, Forrer F, et al (2011) Development of a potent DOTA-conjugated bombesin antagonist for targeting GRPr-positive tumours. Eur J Nucl Med Mol Imaging 38:97-107.

44. Lutje S, Rijpkema M, Helfrich W, Oyen WJ, Boerman OC (2014) Targeted radionuclide and fluorescence dual-modality imaging of cancer: preclinical advances and clinical translation. Mol Imaging Biol 16:747-755.

45. Kaloudi A, Nock BA, Lymperis E, et al (2016) Impact of clinically tested NEP/ACE inhibitors on tumor uptake of [(111)In-DOTA]MG11-first estimates for clinical translation. EJNMMI Res 6:15.

46. Nieciecki M, Dobruch-Sobczak K, Wareluk P, et al (2016) The role of ultrasound and lymphoscintigraphy in the assessment of axillary lymph nodes in patients with breast cancer. J Ultrason 16:5-15.

7

Evaluation of a radiolabeled somatostatin analog for SPECT imaging of pro-inflammatory macrophages

Sandra T. van Tiel[1,#], Lizette Utomo[2,#], Jan de Swart[1], Erik de Blois[1], Marion de Jong[1], Yvonne M. Bastiaansen-Jenniskens[2], Monique R. Bernsen[1]

[1]Department of Radiology & Nuclear Medicine, Erasmus MC, University Medical Center Rotterdam, the Netherlands

[2]Department of Orthopedics, Erasmus MC, University Medical Center Rotterdam, the Netherlands

# both authors contributed equally

Abstract

Background

Macrophages are crucial in the development and progression of various diseases. To monitor their role, various proteins expressed by macrophages may be used as imaging target. In this preclinical study we investigate the value of the somatostatin receptor subtype 2 (SSTR2) as a novel imaging marker for pro-inflammatory macrophages, using an experimental osteoarthritis (OA) mouse model.

Methods

SSTR2 gene expression levels in pro-inflammatory macrophages and human synovium was determined by qPCR. Tracer binding was determined in macrophages and human osteoarthritic synovium after *in vitro* stimulation with IFNγ and TNFα. Presence of pro-inflammatory macrophages in OA mice was determined by anti-CD64$^+$ staining. Accumulation of the tracer in OA knees was determined by μSPECT.

Results

Human macrophages and synovial tissue stimulated with IFNγ+TNFα had significantly upregulated *SSTR2* gene expression and showed increased uptake of SSTR2-targeting tracer. Shortly after OA induction an increase in the presence of pro-inflammatory macrophages was seen as assessed by immunohitochemsitry. Similar findings were obtained with SPECT, with peak uptake of the SSTR2-targeting tracer immediately after surgery followed by a gradual decrease during the course of the next 8 weeks.

Conclusions

Pro-inflammatory macrophages have elevated *SSTR2* expression which makes it possible to image an inflammatory process in the knee with a radiolabeled somatostatin analog for SPECT.

Keywords: macrophage, inflammation, somatostatin receptor subtype 2, imaging, osteoarthritis

Introduction

Macrophages play a crucial role in the development and progression of various diseases, for example osteoarthritis (OA) (1, 2), atherosclerotic plaque (3, 4), type 2 diabetes (5, 6), rheumatoid arthritis (7, 8) and schizophrenia (9, 10). Knowing the role of macrophages during disease development and progression opens possibilities for therapeutic interference . Macrophages varied roles can exacerbate and/or resolve diseases. To detect the presence of macrophage during disease processes, a specific target for imaging is needed. Depending on the activation state, macrophages express various proteins that may be used as imaging target such as the folate receptor β (11), mannose receptor (also known as CD206) (12) and translocator protein (TSPO) (13). These have been proposed as targets for a subtype of macrophages referred to as anti-inflammatory macrophages (14, 15).

Previous studies suggested that the somatostatin receptor subtype 2 (SSTR2) is also a marker for macrophages (16, 17). More recently, it was shown that inflammation-related uptake of an SSTR2-targeting tracer was elevated in atherosclerotic plaques and it was confirmed that the tracer had macrophage specificity (18-20). Somatostatin is a peptide hormone which induces inhibitory effects on two key cellular processes, secretion and cell proliferation. It can bind to five distinct receptors subtypes named SSTR1, SSTR2, SSTR3, SSTR4 and SSTR5. These somatostatin receptors belong to the G-protein coupled receptor family. SSTR2 are highly expressed in human tumors, and are also present in pancreas, spleen, cerebrum, kidney, jejunum, colon, and liver (21, 22). Upon differentiation of human monocytes into pro-inflammatory macrophages, *SSTR2* mRNA was found to be upregulated (23) in activated macrophages making it an interesting molecular target for these cells.

The aim of this preclinical study was to evaluate the potential of SSTR2 as a novel marker to monitor pro-inflammatory macrophages. We therefore determined gene expression levels of *SSTR2* in unstimulated and IFNγ+TNFα stimulated human macrophages, and evaluated SSTR2 protein expression via binding of a SSTR2-binding tracer. We further used osteoarthritis (OA) as disease model to investigate a SSTR2-targeting tracer for macrophage imaging in an osteoarthritic joint. During development of OA, macrophages

7

are attracted to the synovial lining (24, 25) and are pivotal in promoting the production of inflammatory and degradative mediators in the OA synovium, maintaining an inflammatory state in the joint. Human synovial explants were used to perform tracer binding tests in pro-inflammatory circumstances. In this study we evaluated targeting of SSTR2 as a tool for longitudinal imaging of pro-inflammatory macrophages in an experimental mouse model of OA.

Materials and Methods

Ethics approval

All animal experiments were performed in accordance with the ARRIVE guidelines for reporting on Animal Research (26), the Dutch law on animal experimentation, and were approved on March 12th 2014 by the committee on animal experimentation of the Erasmus MC, with protocol number EMC 3246. We chose male mice because sex hormones play a critical role in the progression of OA in the murine DMM surgical model, with males having more severe OA than females (27). Mice were housed at the Experimental Animal Facility of the Erasmus MC with a 12-h light–dark regimen, in individually ventilated cages including extensive cage enrichment. The mice received acidified tap water and standard chow *ad libitum*.

Synovial tissue was obtained with implicit consent from the patients, meaning that they had the right to refuse. The protocol was approved by the medical ethical committee of the Erasmus MC on November 12th 2004 with protocol number MEC-2004-322.

Somatostatin receptor subtype 2 expression

To verify the expression of *SSTR2* on monocyte-derived macrophages, primary human monocytes were isolated from five buffy coats of male donor blood samples (58±8Y; Sanquin Blood bank, Amsterdam, the Netherlands) by Ficoll density gradient separation (GE Healthcare, Little Chalfont, UK) and CD14^{+} magneticactivated- cell sorting (MACS; Miltenyi, Bergisch Gladbach, Germany), as previously described (15). To acquire pro-inflammatory macrophages *in vitro* (15, 28), the monocytes were stimulated 1h after plating with 10 ng/mL IFN-γ (PeproTech, New Jersey, USA) and 10 ng/mL TNF-α (PeproTech, New Jersey,

USA) in X-VIVO™ 15 medium (Lonza, Verviers, Belgium) supplemented with 20% heat-inactivated fetal calf serum (FCS; Lonza, Verviers, Belgium), 50 µg/mL gentamicin (Gibco, Carlsbad, USA) and 1.5 µg/mL amphotericin B (Gibco, Carlsbad, USA), from now on referred to as M(IFNγ+TNFα). The macrophages were stimulated 3 days at 37°C and 5% CO_2. Media and stimuli were refreshed 24h prior to harvest.

To determine the expression of *SSTR2* in human synovial tissue, synovium was obtained as waste material from OA patients (*n*=4, 60±13Y) undergoing total knee replacement surgery. Fat tissue was macroscopically removed and the synovium was cut into pieces of approximately 40 mg wet weight and cultured in Dulbecco's Modified Eagle Medium, low glucose (DMEM; Gibco, Carlsbad, USA), supplemented with 1% Insulin-Transferrin-Selenium (ITS+ Premix, Corning, New York, USA), 50 µg/mL gentamicin (Gibco, Carlsbad, USA), 1.5 µg/mL amphotericin B (Fungizone; Gibco, Carlsbad, USA) and 25 µg/mL L-ascorbic acid 2-phosphate (Sigma-Aldrich, St. Louis, USA). To simulate acute inflammation, half of the number of the explants was stimulated with 10 ng/mL IFNγ + 10 ng/mL TNFα. After 24h of stimulation, the synovial explants were harvested and stored at -80°C until gene expression analysis.

Messenger RNA (mRNA) was isolated from the macrophages using the RNeasy Micro Kit (Qiagen, Hilden, Germany) according to manufacturer's instructions. For the synovial explants, the tissue was first frozen in liquid nitrogen followed by pulverization using a Mikro-Dismembrator (B. Braun Biotech International GmbH, Melsungen, Germany) at 3000 rpm. The tissue was then homogenized with Trizol (Gibco, Carlsbad, USA) and 20% chloroform (Sigma-Aldrich, St. Louis, USA). Complementary DNA (cDNA) was synthesized using the RevertAid™ First Strand cDNA Synthesis Kit (Fermentas GmbH, Leon-Rot, Germany) according to manufacturer's instructions. Expression of *SSTR2* was evaluated using a TaqMan *SSTR2* Gene Expression Assay (Hs00990356_m1; Thermo Fisher Scientific). Glyceraldehyde-3-phosphate dehydrogenase (*GAPDH*; Fw: CAACGGATTTGGTCGTATTGGG; Rev: TGCCATGGGTGGAATCATATTGG; Probe: GGCGCCCCAACCAGCC) was used as a housekeeping gene.

7

Radiolabeled tracers

Two SSTR2 agonists, DOTA-Tyr^3-octreotate, further referred to as DOTA-TATE (BioSynthema, Saint Louis, USA) and DTPA-octreotide (Mallinckrodt Medical, Petten, The Netherlands), and the SSTR2 antagonist DOTA-JR11 (kindly provided by Dr. Helmut Maecke) were used. The tracers were radiolabeled with Indium-111 (Covidien, Zaltbommel, The Netherlands) as previously described (29, 30). Molar activity was 200-300 MBq/nmol. Radiochemical yield was >99% and radiochemical purity was >90% for each tracer.

Binding of SSTR2 tracer

The binding of the radiotracer to SSTR2 present on macrophages was established *in vitro*. Human monocytes were seeded in 6-well plates at a density of 5×10^5 cells/cm^2, and subsequently cultured for 3 days with IFNγ and TNFα, as described in the previous paragraph. After 3 days of stimulation, the macrophages were washed with PBS (Gibco, Carlsbad, USA) and were incubated with 4×10^{-9} M [^{111}In]In-DOTA-TATE. To determine specific binding the cells were also incubated with 4×10^{-9} M [^{111}In]In-DOTA-TATE plus 10^{-6} M DOTA-TATE for 1 h at 37°C. Cellular uptake of the tracer was stopped by removing the supernatant and washing twice with cold PBS. The cells were lysed with 0.1 M NaOH and the amount of radioactivity present in the samples was counted in a gamma counter (1480 WIZARD automatic gamma counter, PerkinElmer, Turku, Finland).

In vitro autoradiography was performed on human OA synovium cryosections (10 μm). The sections were incubated for 1 hour with 80 μL 10^{-9} M [^{111}In]In-DOTA-JR11 with or without excess (10^{-6} M) unlabeled DOTA-TATE to determine non-specific binding. After incubation, the excess radiotracer was removed and the sections were exposed to super resolution phosphor screens (Packard Instruments Co., Meriden, USA) for 7 days. Binding of the radiotracers to SSTR2 containing areas in the sections was quantified using Optiquant (Packard Instruments Co., Groningen, The Netherlands) and expressed as density light units/mm^2 (DLU/mm^2). Sections of human H69 tumour, an SSTR2-positive xenograft, were used as positive control. All sections were stained with hematoxylin and eosin to determine the localisation of cell dense areas where the macrophages can be found.

Osteoarthritis induction

Experimental OA was induced, during light time of the day/night cycle, by destabilization of the medial meniscus (DMM) (31). The right knees of 40 male C57BL/6 mice of 12-14 weeks old (Harlan Laboratories/Envigo, Cambridgeshire, UK) underwent dissection of the medial meniscotibial ligament (MMTL). As control, the contralateral knee underwent a sham procedure, which entailed no transection of the MMTL.

Immunohistochemical analysis

At 1, 3, 7, 14, 28, and 56 days after OA induction both DMM and control knees were excised and fixed for 10 days in 4% formaldehyde (BoomLab, Meppel, The Netherlands). After decalcification the knees were dehydrated, embedded in paraffin and completely sectioned in the coronal plane. For the CD64 histochemical (IHC) staining, a CD64 antibody (Sino-Biological, 50086-R001, 5 ug/ml) was incubated on the slides for 60 min, and subsequently incubated with link and label (Concentrated MultiLink® and Concentrated AP Label; BioGenex, Fremont, California, USA); New Fuchsine was used as substrate (32). The extent of positive CD64 staining in the sections was scored by bright-field microscopy and ranked. Ranking means that all knees were arranged from least intensely stained to most intensely stained using bright field microscopy. The staining intensity of the markers was ranked amongst all time points.

To confirm that OA was induced after 8 weeks, three consecutive thionin-stained sections of the medial femoral condyle and medial tibial plateau were evaluated. The structural cartilage damage was scored by the OARSI scoring system by Glasson *et al*. (1, 33). The score of the quadrants of three consecutive sections was summed and used for analysis. Histological images were acquired with a NanoZoomer 2.0-HT slide scanner (Hamamatsu, Hamamatsu City, Japan).

In vivo imaging

To evaluate the influx of pro-inflammatory macrophages during OA development, OA was induced in mice (n=6) as described above. Because macrophage polarization is a dynamic process, we wanted to scan the knee as soon as possible after tracer injection. The mice were imaged 2 hours after i.v. injection of radiolabeled tracer (60 MBq/200pmol [^{111}In]In-DTPA-

7

octreotide) on day 1, 3, 7, 14, 28 or 56 after induction of OA. At day 3 after OA induction 3 mice were injected with 40 nmol block, DOTA-Tyr^3-TATE, 1 minute prior to an injection with 60 MBq/200pmol [^{111}In]In-DTPA-octreotide. Single-photon emission computed tomography (SPECT) was performed on a MILabs VECTor+/CT system (Utrecht, the Netherlands) (34) with an ultra-high sensitivity mouse collimator with fifty-four 2.0 mm pinholes. A 55-minutes SPECT was acquired in list mode along a spiral trajectory, scan mode fine and 10 positions. SPECT was followed by CT (55 keV, 615 mA). SPECT data were reconstructed using the pixel-based ordered subsets expectation maximization (POSEM) developed by MILabs (35) algorithm with 30 iterations, 4 subsets and a voxel size of 0.4 mm. Photopeaks 171 and 245 keV were used, scatter and background were corrected for with the triple-energy-window method (for 171 keV peak % width of 7 and for 245 keV peak % width of 10) (36). CT was reconstructed using filtered back-projection. SPECT and CT were registered; SPECT data were corrected for attenuation using the CT data (34). A post-reconstruction 3-dimensional Gaussian filter was applied. The resulting data was analyzed using inviCRO VivoQuant software (Boston, MA, USA) by quantification of manually drawn regions of interests (ROIs) based on CT. All data were represented as percentage of the injected dose per tissue volume %IA/cm3).

Statistical analysis

For the *in vitro* experiments, a mixed linear model after log transform was used followed by a Bonferroni's *post hoc* comparisons test using PASW Statistics 22.0 (SPSS Inc. Chicago, USA). For the histological staining experiment, differences in CD64 ranks for the time points were determined by a Kruskal-Wallis test. In the uptake experiment and autoradiography the mean values between the different groups (± stimulation, ± block) were compared and analyzed with a Two-way ANOVA. To compare values for DMM and sham surgery (*in vivo* imaging) the paired t-test was applied. Differences were considered statistically significant when $p < 0.05$.

Results

Somatostatin receptor subtype 2 mRNA expression

To establish the effect of inflammatory stimuli on *SSTR2* mRNA expression of macrophages, *SSTR2* mRNA levels were determined in unstimulated and IFNγ+TNFα-stimulated macrophages by qPCR. Following stimulation with IFNγ+TNFα, expression of *SSTR2* mRNA significantly increased by a factor of 3.6 (*p*<0.005) relative to unstimulated macrophages (Fig. 1A). Similar to macrophages, stimulation of synovial tissue of OA patients with IFNγ+TNFα, also resulted in increased expression levels of *SSTR2 mRNA* (10-fold, *p*<0.001) relative to unstimulated tissue (Fig. 1B).
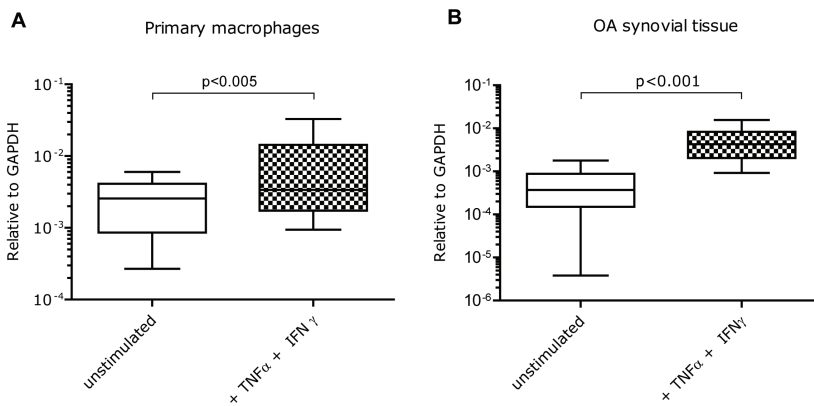
Figure 1 Gene expression levels of somatostatin receptor subtype 2 (*SSTR2*) in human primary macrophages and osteoarthritic synovial tissue. *SSTR2* gene expression relative to the expression of *GAPDH* in **A** unstimulated human monocyte-derived macrophages and IFNγ+TNFα-stimulated macrophages. **B** osteoarthritic synovial tissue, cultured *in vitro*, with and without IFNγ+TNFα stimulation. Data is presented from min to max including the median.

Binding of SSTR2 tracer

Stimulation of primary monocyte-derived macrophages with IFNγ+TNFα *in vitro* resulted in a significant increase of [^{111}In]In-DOTA-TATE uptake (Fig. 2). Relative to unstimulated macrophages the uptake of [^{111}In]In-DOTA-TATE increased (1.6-fold, p<0.05). For both stimulated and unstimulated macrophages uptake of [^{111}In]In-DOTA-TATE was largely blocked following addition of excess unlabeled DOTA-TATE (p<0.001).

Figure 2 Binding of [¹¹¹In]In-DOTA-TATE to SSTR2 on human monocyte-derived macrophages. Binding of [¹¹¹In]In-DOTA-TATE (as a measure of SSTR2 presence) to M(IFNγ+TNFα) in kBq/1e⁵ cells. Blocking of the specific binding to SSTR2 was performed with excess of unlabeled DOTA-TATE. Data is presented as mean + SD.
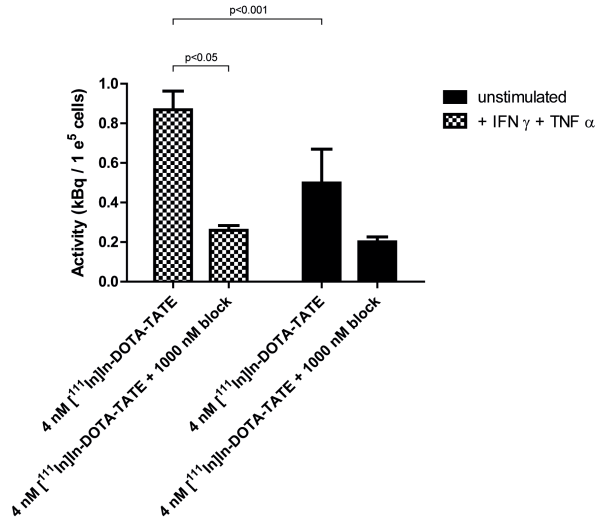
Autoradiography analysis of binding of the radiolabeled tracer [¹¹¹In]In-DOTA-JR11 showed regions with higher signal intensities corresponding to cell dense areas on H&E-stained sections (Fig. 3A and 3B). The intensity of the autoradiography signal was significantly increased up to 3.1 times (average 1.6; range 0.5-3.1; $p<0.05$) in IFNγ+TNFα-stimulated synovial tissue relative to unstimulated synovial tissue (Fig. 3C).

Presence of macrophages during experimental OA
To establish the relevance of SSTR2 tracer as a marker for pro-inflammatory macrophages *in vivo*, presence of macrophages and uptake of SSTR2 tracer was studied in a mouse DMM model for OA over time.

From knees, which were harvested eight weeks after induction of OA by DMM, three consecutive thionin-stained sections of the medial femoral condyle and medial tibial plateau were evaluated. The summed OARSI scores for three DMM knees were: 2.5, 4.0, and 10.5. Osteophytes were present in all DMM knees. Control knees did not have any signs of cartilage degradation (OARSI score 0 for all knees) and did not present any indications of osteophyte formation (Fig. 4).
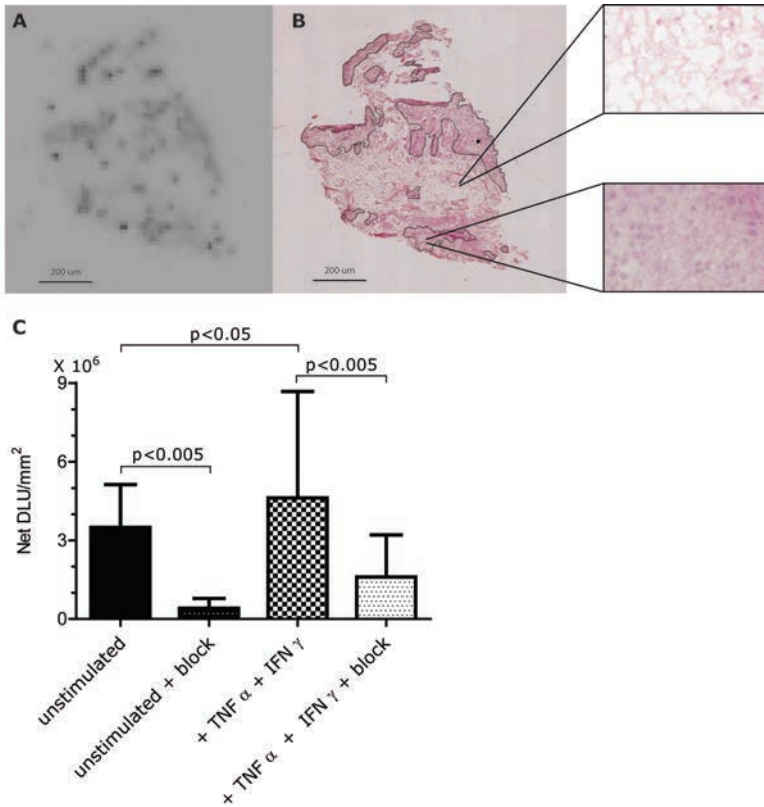
Figure 3 Binding of [¹¹¹In]In-DOTA-JR11 to human synovial tissue. (A) Autoradiography of a section of an OA synovial explant. Dark spots indicate uptake of [¹¹¹In]In-DOTA-JR11. **(B)** H&E staining of IFNγ+TNFα-stimulated synovial tissue of the same sample shown in A with 2 40X magnifications. Segmentation lines indicate relevant areas used for analysis. **(C)** Binding of [¹¹¹In]In-DOTA-JR11 to human synovial tissue is shown as NET DLU/mm^2 + SD. Samples of synovium derived from 3 different OA patients undergoing total knee resection were incubated with (two right bars) and without IFNγ/TNFα (two left bars). To determine specific binding a 1000-times excess of unlabeled DOTA-TATE was added to some samples (solid black bars).

CD64 positive cells, indicating pro-inflammatory macrophages, were present from day 1 onward. The sections were ranked to distinguish low-positivity and high-positivity. The number of CD64-positive macrophages were elevated at day 1 and 3, and slowly diminished during the following weeks. There were statistically differences seen between the ranks at the different time points (p<0.0001). No statistically significant differences were seen in the pattern of CD64$^+$ macrophages presence over time between the sham-operated and DMM knees (Fig. 5).
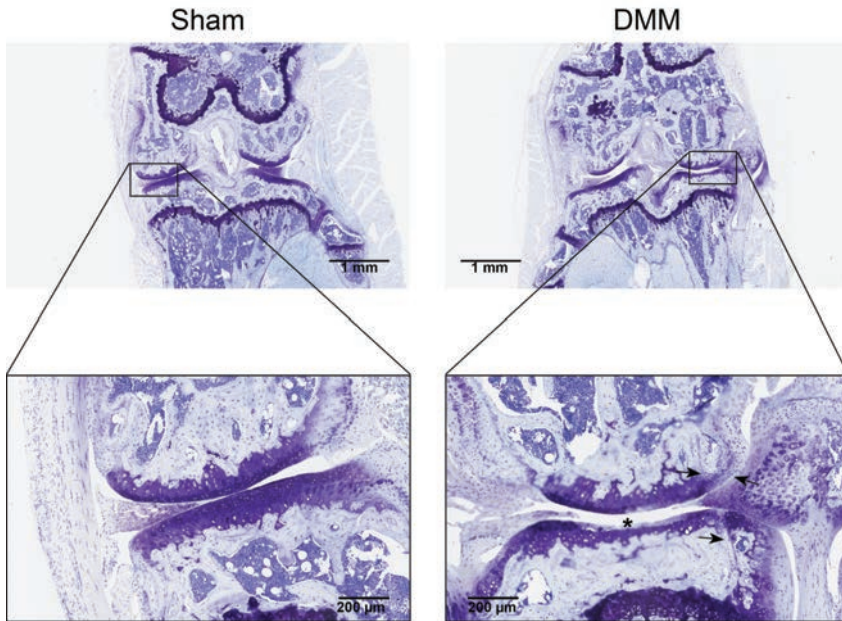
Figure 4 Cartilage damage and osteophyte formation after induction of experimental osteoarthritis (OA) by DMM. Thionin staining of a mouse knee 8 weeks after OA induction by destabilization of the medial meniscus (DMM). The femur condyle and tibia plateau are shown in the enlargements. The sham-operated knee had a summed OARSI score of 0 and the knee with DMM had a summed OARSI score of 10.5 (maximum possible score 72). Cartilage damage (at asterisk) and osteophytes (indicated by the arrows) were seen in all DMM knees.
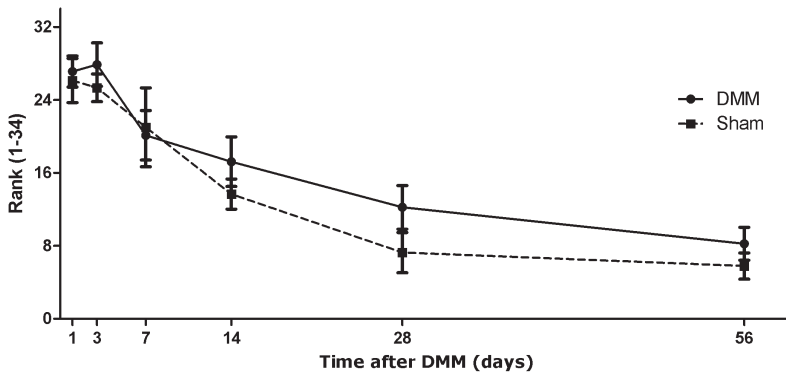
Figure 5 Presence of CD64+ macrophages during development of experimental osteoarthritis after DMM. The continuous line represents the DMM knees. The dotted line represents the sham knees. Each group contains 7-9 knees. Data is presented as mean ± SD, p<0.0001 between different time points.

In figure 6A a representative SPECT/CT image is shown of a DMM knee 3 days after destabilization of the medial meniscus in which accumulation of the radioactive tracer was observed. Percentage injected activity per volume (%IA/cm^3) was calculated over time after DMM. During the first 7 days after DMM surgery, increased amounts of radioactivity were found in the knees, which gradually decreased over time (Fig. 6B). Herein we saw a similar pattern for both the knees in which OA was induced by DMM and for the knees that underwent sham surgery.

To determine the specificity of the radioactive signal a blocking experiment was executed. After the SPECT/CT scans the knees and thymus were removed and placed in a gammacounter. Both SPECT/CT scans and gammacounter data showed that the binding was receptor-specific (Supplementary Digital Material 1: Supplementary Figure 1). Co-injection of excess unlabeled DOTA-Tyr^3-TATE reduced uptake of [^{111}In]In-DTPA-octreotide in the knees and thymus.
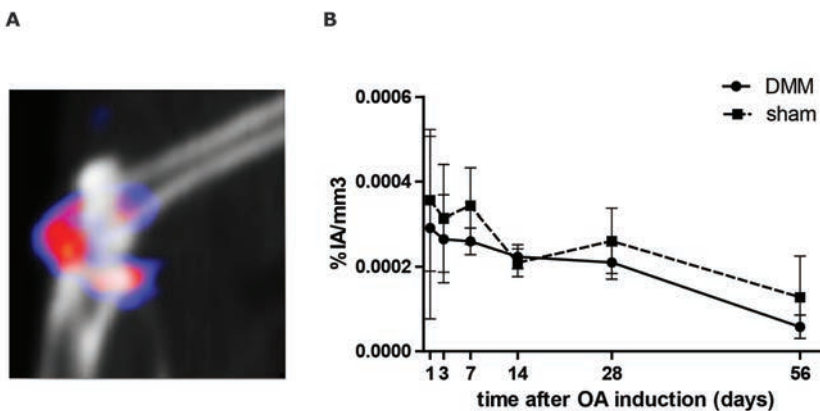
Figure 6 SPECT/CT imaging of *in vivo* uptake of [^{111}In]In-DTPA-octreotide in osteoarthritic (OA) mice knees. A Sagittal view of a knee 3 days after OA induction through destabilization of the medial meniscus (DMM). Scan was made 2 h post injection with [^{111}In]In-DTPA-octreotide. **B** Percentage injected activity ([^{111}In]In-DTPA-octreotide) per volume (knee) (%IA/cm^3) was calculated over time after induction of OA. The continuous line represents the DMM knees. The dotted line represents the sham knees. Each group contains 6 animals. Data is presented as mean ± SD, p= 0.099.

Discussion

Pro-inflammatory macrophages have been identified as crucial mediators in various disease processes. Non-invasive monitoring of their presence during disease progression is therefore very desirable. In this report, we showed that pro-inflammatory macrophages (IFNγ+TNFα stimulated) had elevated SSTR2 expression and showed concomitant increased uptake of SSTR2-targeting radiolabeled peptides, which are suitable as SPECT tracers. Using such a SSTR2 SPECT tracer in a translational setting, we also demonstrated that under pro-inflammatory conditions there was increased binding of the tracer in human OA synovium. Moreover, in an *in vivo* model we showed that macrophage-associated inflammation resulted in concomitant uptake of [^{111}In]In-DTPA-octreotide in mouse knees, indicating that an SSTR2-targeting SPECT tracer can be used to monitor the course of a pro-inflammatory response over time *in vivo*.

Destabilization of the medial meniscus in mice was used as a model for OA with anticipated involvement of pro-inflammatory macrophages. In many other studies this model has been used for studying processes during the onset of OA and in studies evaluating novel intervention strategies for OA (37-39). This animal model has a low variability (31) and represents posttraumatic human injury which leads to joint degeneration (40). During human OA development a macrophage influx was seen (41) and macrophage-associated inflammation was related with structural damage and disease progression.

As shown in this study, it appeared that the influx of macrophages was time dependent and associated with the development path of OA, but the macrophage influx in the knee was not exclusively associated with development of OA. An influx of macrophages was also observed in the sham-operated knee, most likely due to the inflammatory reaction to tissue damage caused by surgical manipulation. It should be noted that the sham knees had no structural cartilage damage or osteophyte formation, features that are associated with OA. Since the SSTR2 tracer specifically targets inflammatory cells, and not damaged cartilage, SSTR2 receptor uptake occured in both DMM and sham-operated knees due to the presence of inflammatory macrophages in both situations. The pattern seen with uptake of SSTR2 targeting tracer

in the knee, and the pattern seen with the presence of pro-inflammatory macrophages (histological aCD64 staining) of the knee, proceeded in the same way; starting with an high influx of macrophages which decreased during the course of time.

For potential clinical relevance we evaluated SSTR2 tracer uptake in synovial tissue samples derived from OA patients. OA synovium showed specific uptake of [^{111}In]In-DOTA-JR11, which could be further enhanced under acutely induced inflammatory conditions (stimulation with IFNγ+TNFα). There was considerable variation in uptake of the SSTR2 tracer between patient samples which was most likely due to the large heterogeneity in disease state between OA patients and whether or not a given patient had a flare of inflammation at time of surgery. It is also known that synovium consists of a heterogeneous cell population including synoviocytes, macrophages and fibroblasts. Although it cannot fully be excluded that SSTR2-binding tracer is taken up by cells other than macrophages, we consider this option highly unlikely to substantially contribute to the measured activity. It is known that the number of macrophages dramatically increases in inflammatory arthritis relative to healthy synovia (41, 42), also seen in this study using histological evaluation. It is therefore most likely that the signal in inflamed knees is caused by the presence of pro-inflammatory macrophages.

In this research high resolution scans are of utmost importance, because the target is very small. That is why we used an indium-111 labeled tracer. When this tracer is going to be used in the clinic we will be using a radioactive isotope compatible with PET. PET has in the clinic a higher resolution, half-life of radioactive isotopes is shorter so patients can leave the hospital sooner and images are less noisy therefor accurate quantification can be performed.

We made use of a mouse model where we introduced OA through destabilization of the medial meniscus. Mice knees are very small and DMM results in a mild inflammation. Altough we had these restrictions we were able to successfully visualize, quantify and monitor the inflammation process by SPECT/CT imaging. Perhaps with the use of a larger animal model and/or a disease model with more macrophage involvement, like rheumatoid arthritis (43, 44), will facilitate further research. Our findings are promising for the use

7

of SSTR2 targeting tracers in studying macrophage involvement in disease processes. Macrophages are crucial in the development and progression of various diseases and that is why accurate imaging of pro-inflammatory macrophages, beside the already established anti-inflammatory macrophage tracers (11, 45), might be an important step forward in understanding disease development. This is also indicated by recent publications on studies in which macrophages are being imaged in atherosclerotic plaques using the folate, mannose and somatostatine type 2 receptor (18, 46, 47).

Conclusion

Our research showed that pro-inflammatory macrophages (IFNγ+TNFα stimulated) had elevated *SSTR2* expression and show concomitant elevated binding of SSTR2-targeting radiolabeled peptides suitable as SPECT tracers. Under pro-inflammatory conditions there was an increase in presence of CD64^{+} cells especially at day 1 and 3 after OA induction. *In vivo* SSTR2 SPECT imaging showed an increase of radioactivity in the knee at day 1-7 after OA induction. So, SSTR2 can be a marker to longitudinally monitor pro-inflammatory macrophages *in vivo*.

Conflicts of interest

None declared

Acknowledgments

References

1. Blom AB, van Lent PL, Holthuysen AE, van der Kraan PM, Roth J, van Rooijen N, et al. Synovial lining macrophages mediate osteophyte formation during experimental osteoarthritis. Osteoarthritis Cartilage. 2004;12(8):627-35.

2. Lopes EBP, Filiberti A, Husain SA, Humphrey MB. Immune Contributions to Osteoarthritis. Curr Osteoporos Rep. 2017;15(6):593-600.

3. Moore KJ, Sheedy FJ, Fisher EA. Macrophages in atherosclerosis: a dynamic balance. Nat Rev Immunol. 2013;13(10):709-21.

4. Colin S, Chinetti-Gbaguidi G, Staels B. Macrophage phenotypes in atherosclerosis. Immunol Rev. 2014;262(1):153-66.

5. Kraakman MJ, Murphy AJ, Jandeleit-Dahm K, Kammoun HL. Macrophage polarization in obesity and type 2 diabetes: weighing down our understanding of macrophage function? Front Immunol. 2014;5:470.

6. Xu H, Barnes GT, Yang Q, Tan G, Yang D, Chou CJ, et al. Chronic inflammation in fat plays a crucial role in the development of obesity-related insulin resistance. J Clin Invest. 2003;112(12):1821-30.

7. Laria A, Lurati A, Marrazza M, Mazzocchi D, Re KA, Scarpellini M. The macrophages in rheumatic diseases. J Inflamm Res. 2016;9:1-11.

8. Zhang Q, Yuan R, Li C, Wei W, Shen W, Cui Y, et al. Macrophage depletion with clodronate-containing liposomes affects the incidence and development of rheumatoid arthritis Einfluss des Makrophagenruckgangs mittels clodronathaltiger Liposomen auf die Inzidenz und Entwicklung einer rheumatoiden Arthritis. Z Rheumatol. 2018.

9. Takahashi Y, Yu Z, Sakai M, Tomita H. Linking Activation of Microglia and Peripheral Monocytic Cells to the Pathophysiology of Psychiatric Disorders. Front Cell Neurosci. 2016;10:144.

10. Frick LR, Williams K, Pittenger C. Microglial dysregulation in psychiatric disease. Clin Dev Immunol. 2013;2013:608654.

11. Puig-Kroger A, Sierra-Filardi E, Dominguez-Soto A, Samaniego R, Corcuera MT, Gomez-Aguado F, et al. Folate receptor beta is expressed by tumor-associated macrophages and constitutes a marker for M2 anti-inflammatory/regulatory macrophages. Cancer Res. 2009;69(24):9395-403.

12. Bala G, Baudhuin H, Remory I, Gillis K, Debie P, Krasniqi A, et al. Evaluation of [(99m)Tc]Radiolabeled Macrophage Mannose Receptor-Specific Nanobodies for Targeting of Atherosclerotic Lesions in Mice. Mol Imaging Biol. 2018;20(2):260-7.

13. Narayan N, Mandhair H, Smyth E, Dakin SG, Kiriakidis S, Wells L, et al. The macrophage marker translocator protein (TSPO) is down-regulated on pro-inflammatory 'M1' human macrophages. PLoS One. 2017;12(10):e0185767.

14. Van De Wiele C, Sathekge M, Maes A. Targeting monocytes and macrophages by means of SPECT and PET. Q J Nucl Med Mol Imaging. 2014;58(3):269-75.

15. Utomo L, van Osch GJ, Bayon Y, Verhaar JA, Bastiaansen-Jenniskens YM. Guiding synovial inflammation by macrophage phenotype modulation: an in vitro study towards a therapy for osteoarthritis. Osteoarthritis Cartilage. 2016;24(9):1629-38.

16. ten Bokum AM, Hofland LJ, van Hagen PM. Somatostatin and somatostatin receptors in the immune system: a review. Eur Cytokine Netw. 2000;11(2):161-76.

17. Dalm VA, van Hagen PM, van Koetsveld PM, Achilefu S, Houtsmuller AB, Pols DH, et al. Expression of somatostatin, cortistatin, and somatostatin receptors in human monocytes, macrophages, and dendritic cells. Am J Physiol Endocrinol Metab. 2003;285(2):E344-53.

18. Tarkin JM, Joshi FR, Evans NR, Chowdhury MM, Figg NL, Shah AV, et al. Detection of Atherosclerotic Inflammation by (68)Ga-DOTATATE PET Compared to [(18)F]FDG PET Imaging. J Am Coll Cardiol. 2017;69(14):1774-91.

19. Rominger A, Saam T, Vogl E, Ubleis C, la Fougere C, Forster S, et al. In vivo imaging of macrophage activity in the coronary arteries using 68Ga-DOTATATE PET/CT: correlation with coronary calcium burden and risk factors. J Nucl Med. 2010;51(2):193-7.

7

20. Li X, Bauer W, Kreissl MC, Weirather J, Bauer E, Israel I, et al. Specific somatostatin receptor II expression in arterial plaque: (68)Ga-DOTATATE autoradiographic, immunohistochemical and flow cytometric studies in apoE-deficient mice. Atherosclerosis. 2013;230(1):33-9.

21. Patel YC. Somatostatin and its receptor family. Front Neuroendocrinol. 1999;20(3):157-98.

22. Gunther T, Tulipano G, Dournaud P, Bousquet C, Csaba Z, Kreienkamp HJ, et al. International Union of Basic and Clinical Pharmacology. CV. Somatostatin Receptors: Structure, Function, Ligands, and New Nomenclature. Pharmacol Rev. 2018;70(4):763-835.

23. Armani C, Catalani E, Balbarini A, Bagnoli P, Cervia D. Expression, pharmacology, and functional role of somatostatin receptor subtypes 1 and 2 in human macrophages. J Leukoc Biol. 2007;81(3):845-55.

24. Benito MJ, Veale DJ, FitzGerald O, van den Berg WB, Bresnihan B. Synovial tissue inflammation in early and late osteoarthritis. Ann Rheum Dis. 2005;64(9):1263-7.

25. Ene R, Sinescu RD, Ene P, Cirstoiu MM, Cirstoiu FC. Synovial inflammation in patients with different stages of knee osteoarthritis. Rom J Morphol Embryol. 2015;56(1):169-73.

26. Kilkenny C, Browne WJ, Cuthill IC, Emerson M, Altman DG. Improving bioscience research reporting: the ARRIVE guidelines for reporting animal research. PLoS Biol. 2010;8(6):e1000412.

27. Ma HL, Blanchet TJ, Peluso D, Hopkins B, Morris EA, Glasson SS. Osteoarthritis severity is sex dependent in a surgical mouse model. Osteoarthritis Cartilage. 2007;15(6):695-700.

28. Utomo L, Bastiaansen-Jenniskens YM, Verhaar JA, van Osch GJ. Cartilage inflammation and degeneration is enhanced by pro-inflammatory (M1) macrophages in vitro, but not inhibited directly by anti-inflammatory (M2) macrophages. Osteoarthritis Cartilage. 2016;24(12):2162-70.

29. de Blois E, Chan HS, de Zanger R, Konijnenberg M, Breeman WA. Application of single-vial ready-for-use formulation of 111In- or 177Lu-labelled somatostatin analogs. Appl Radiat Isot. 2014;85:28-33.

30. Bakker WH, Albert R, Bruns C, Breeman WA, Hofland LJ, Marbach P, et al. [111In-DTPA-D-Phe1]-octreotide, a potential radiopharmaceutical for imaging of somatostatin receptor-positive tumors: synthesis, radiolabeling and in vitro validation. Life Sci. 1991;49(22):1583-91.

31. Glasson SS, Blanchet TJ, Morris EA. The surgical destabilization of the medial meniscus (DMM) model of osteoarthritis in the 129/SvEv mouse. Osteoarthritis Cartilage. 2007;15(9):1061-9.

32. Gautier EL, Shay T, Miller J, Greter M, Jakubzick C, Ivanov S, et al. Gene-expression profiles and transcriptional regulatory pathways that underlie the identity and diversity of mouse tissue macrophages. 2012;13(11):1118-28.

33. Glasson SS, Chambers MG, Van Den Berg WB, Little CB. The OARSI histopathology initiative - recommendations for histological assessments of osteoarthritis in the mouse. Osteoarthritis Cartilage. 2010;18 Suppl 3:S17-23.

34. Branderhorst W, Vastenhouw B, Beekman FJ. Pixel-based subsets for rapid multi-pinhole SPECT reconstruction. Phys Med Biol. 2010;55(7):2023-34.

35. Wu C, van der Have F, Vastenhouw B, Dierckx RA, Paans AM, Beekman FJ. Absolute quantitative total-body small-animal SPECT with focusing pinholes. Eur J Nucl Med Mol Imaging. 2010;37(11):2127-35.

36. Ogawa K, Harata Y, Ichihara T, Kubo A, Hashimoto S. A practical method for position-dependent Compton-scatter correction in single photon emission CT. IEEE Trans Med Imaging. 1991;10(3):408-12.

37. Van Lent PL, Blom A, Holthuysen AE, Jacobs CW, Van De Putte LB, Van Den Berg WB. Monocytes/macrophages rather than PMN are involved in early cartilage degradation in cationic immune complex arthritis in mice. J Leukoc Biol. 1997;61(3):267-78.

38. Choi MC, Choi WH. Mithramycin A Alleviates Osteoarthritic Cartilage Destruction by Inhibiting HIF-2alpha Expression. Int J Mol Sci. 2018;19(5).

39. Song JL, Li L, Fang H, Cai DZ. Intraperitoneal injection of thalidomide alleviates early osteoarthritis development by suppressing vascular endothelial growth factor expression in mice. Mol Med Rep. 2018;18(1):571-9.

40. Holyoak DT, Tian YF, van der Meulen MC, Singh A. Osteoarthritis: Pathology, Mouse Models, and Nanoparticle Injectable Systems for Targeted Treatment. Ann Biomed Eng. 2016;44(6):2062-75.

41. Smith MD. The normal synovium. Open Rheumatol J. 2011;5:100-6.

42. Kennedy A, Fearon U, Veale DJ, Godson C. Macrophages in Synovial Inflammation. Frontiers in Immunology. 2011;2.

43. Kinne RW, Brauer R, Stuhlmuller B, Palombo-Kinne E, Burmester GR. Macrophages in rheumatoid arthritis. Arthritis Res. 2000;2(3):189-202.

44. Udalova IA, Mantovani A, Feldmann M. Macrophage heterogeneity in the context of rheumatoid arthritis. Nat Rev Rheumatol. 2016;12(8):472-85.

45. Put S, Westhovens R, Lahoutte T, Matthys P. Molecular imaging of rheumatoid arthritis: emerging markers, tools, and techniques. Arthritis Res Ther. 2014;16(2):208.

46. Winkel LC, Groen HC, van Thiel BS, Muller C, van der Steen AF, Wentzel JJ, et al. Folate receptor-targeted single-photon emission computed tomography/computed tomography to detect activated macrophages in atherosclerosis: can it distinguish vulnerable from stable atherosclerotic plaques? Mol Imaging. 2014;13.

47. Varasteh Z, Hyafil F, Anizan N, Diallo D, Aid-Launais R, Mohanta S, et al. Targeting mannose receptor expression on macrophages in atherosclerotic plaques of apolipoprotein E-knockout mice using (111)In-tilmanocept. EJNMMI Res. 2017;7(1):40.

7

Supplemental Data
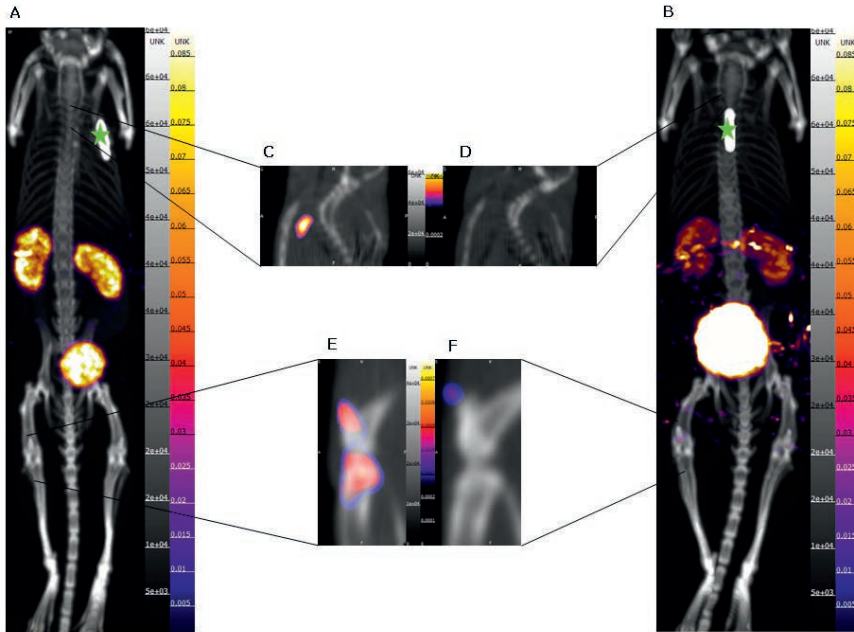
Figure S1 SPECT/CT imaging of *in vivo* blocking of 60 MBq/200pmol [¹¹¹In]In-DTPA-octreotide with (B,D,F) or without (A,C,E) 40 nmol DOTA-Tyr³-TATE in mice 3 days after osteoarthritis (OA) induction. A Whole body maximum intensity projection. Kidneys and bladder are clearly visible **B** Whole body maximum intensity projection. Tracer is rapidly excreted via urinary tract **C** Saggital view of the thorax. Somatostatin subtype 2 cells in the thymus are visible **D** Saggital view of the thorax. Signal of the thymus is blocked **E** Saggital view of the OA knee. Radioactive signal is clearly visible **F** Saggital view of the OA knee. Radioactive signal is blocked. H=Head, F=Feet, A=Anterior, P=Posterior, Green asterisk = mouse identification chip.
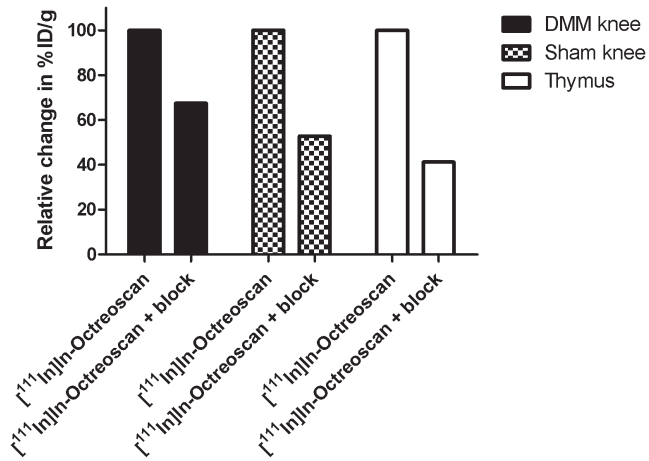
Figure S2 Relative change in %ID/g after in vivo blocking of 60 MBq/200pmol [111In]In-DTPA-octreotide with 40 nmol DOTA-Tyr³-TATE in mice 3 days after osteoarthritis (OA) induction.

7

8

Summary

Discussion

Concluding remarks

Summary, Discussion, Concluding remarks

For this thesis we have performed preclinical studies in different models and at different levels of complexity with the ultimate aim to optimize cellular imaging in regenerative medicine, cancer and osteoarthritis. Single and multi-modal imaging was performed using MRI, SPECT and CT.

In **Chapter 1** a general introduction to molecular imaging is given. We describe the imaging devices used in molecular imaging and cell labelling strategies that can be employed.

Cellular imaging in regenerative medicine

Regenerative medicine focuses on repair, replacement or regeneration of damaged tissue to restore functions. Impaired functions can be caused by congenital defects, by disease, trauma, and ageing. A variety of technologies and approaches such as gene therapy, stem cell therapy and progenitor cell therapy, as well as tissue engineering can be used for function repair (1).

In case of cell therapy it is essential to know if accurate delivery of the cell graft occurs (2). Monitoring the fate of the transplanted cells and measuring their therapeutic effect (e.g. improved cardiac output) is crucial to establish efficacy of cell therapy. Various methods have been studied for cell labelling and imaging. One method that has been considered as highly efficient and translatable is labelling of the cells with iron oxide nanoparticles. Such particles result in a local change in MRI signal and offer the possibility of highly sensitive detection of labelled cells at high spatial resolution within anatomical and/or functional context as imaged by MRI. As described in Chapters 2, 3 and 4 various types of iron oxide particles can be used. In these studies two types of particles were applied; 1) Ferumoxide which are super paramagnetic iron oxide particles (SPIO) having a particle diameter between 80 and 150nm and an iron oxide core (3-5) and 2) the larger micron-sized paramagnetic iron oxide particles (MPIO) composed of polystyrene–divinyl benzene polymer micro spheres containing a magnetite core and tagged with the fluorescent dye Dragon green (480/520 nm). MPIO particles have an average size of 1630 nm and have been shown to be functionally inert (6, 7). The iron oxide core of both SPIO and MPIO has a strong magnetic moment, causing a disturbance of the local magnetic field in

MRI resulting in local signal loss in MR images. The efficacy of these particles for cell labelling and imaging studies was investigated by variations in iron particle labelling protocols, and the influence thereof on incorporation, distribution and retention of iron oxide nanoparticles as described in **Chapter 2**. Cultured human umbilical cord cells (HUVECs) were labelled with iron particles. The average iron load of SPIO increased when incubation time was extended from 4h to 24h. The optimal labelling protocol in this study resulted in 12.0 pg iron/per cell. For MPIO labelling, incubation time was of less importance, since most of the particles were already incorporated in the cell within 4 h, with a 100% labeling efficiency and an intracellular iron load of up to 626 pg iron/cell. MPIO were taken up more efficiently, were better tolerated without causing significant cell death and had a much more pronounced effect on cell appearance in an MR image than SPIO. A drawback of the use of the bigger MPIO particles is that there are fewer particles per cell. When cells divide, not every daughter cell will contain a MPIO particle. This results in the inability to track these cells. Optimal label incorporation required different protocols for SPIO and MPIO. No standard labelling protocol could be used for different cell types growing in vitro. Cell lines differ from each other for example in ease of spontaneous particle uptake. They also can differ in particle uptake rate and in tolerated load of iron particles in the cell. Other studies showed that iron labelled cells can be followed for several weeks in vivo (8, 9). The iron particles inside the cells can be visualized with MRI and the iron particles have an effect on different MRI parameters (eg. R2' (R2*-R2) = relaxivity). So, cell labelling with iron particles offers a promising method for in vivo human and animal model cell tracking by MRI. Different processes can occur when iron labelled cells are injected *in vivo*, like cell death, cell migration and cell division, all influencing signal intensity (10, 11). Mimicking these biologically relevant processes was executed by labelling cells with small (SPIO) and larger (MPIO) iron particles; the performed experiments and the results are described in **Chapter 3**. For the MR measurements phantoms were prepared. As a model system for dividing cells *in vivo*, Brown Norway 175 sarcoma cells were labelled with SPIO and injected subcutaneously in the flank of a rat. The effects of spatial distribution and compartmentalization of paramagnetic iron-oxide particles on relaxivity were analyzed. We demonstrated that relaxometry does not allow labelled cell quantification when multiple physiological processes such as cell division and cell migration coexist. Not only we, but also other groups (12-14), concluded

8

that if there are different physiological processes occurring at the same time (which will for sure happen in vivo) which all influence MRI parameters, it is very difficult to determine the fate of transplanted iron labelled cells *in vivo*. Using paramagnetic iron oxide particles for cell labelling also has other drawbacks. The nanoparticles can have subtle immunological effects (15), affect cellular proliferation (16, 17), and nanoparticles can be toxic to certain cells at high concentrations (18). The relaxivity changes of iron oxides particles are dependent on the environment. The intensity of the iron labelled cells becomes degraded as iron oxide becomes diluted by proliferation (19) or by lysosomal action (20, 21). To distinguish viable labelled cells with iron deposits released from dead or dying cells or macrophages might be provided by MR reporter gene technology. Here a gene encoding for expression of proteins involved in iron metabolism, e.g. ferritin and transferrin receptors is introduced into the cell. (Over) expressing these proteins results in accumulation of iron in the cell leading to altered signals on MRI (22, 23). Most MRI images are derived from proton (^{1}H) spins, but other half-integer spin nuclei can also be used for cell imaging with MRI. New developments have occurred, like fluor-19 imaging, which can be used for quantitative magnetic resonance imaging. Fluor-19 has several properties to be suitable for MRI: It possesses comparable MR sensitivity to proton imaging, Fluor-19 does not naturally occur in the human body, its resonance differs by only 6% from that of ^{1}H, potentially allowing ^{19}F MRI to be conducted on existing ^{1}H imaging hardware, and it is not naturally present in biological tissues so it exhibits no tissue background signal, allowing specific and selective assessment of the administrated ^{19}F-containing compounds in cells *in vivo* (24-26).

For MR imaging of resident cell types, such as for instance in tumor vasculature and tissue engineered vasculature structures, it could be advantageous to label cells *in vivo* instead of, as described previously, *in vitro* with iron particles. Changes in vascularization and vascular dysfunction could reveal disease development, like in cardiovascular and kidney disease and in tumor development and is therefore of interest to image these processes. The aim of our in vitro study described in **Chapter 4** was to find optimal parameters for non-invasive, CD31-targeted (a biomarker constitutively expressed on endothelial cell membranes (14)), microbubble-mediated SPIO-labelling of endothelial cells. When ultrasound was applied, the microbubbles oscillated

due to sequential compression and expansion caused by pressure variations. Cell membrane permeability is increased this way, because the microbubbles cause shear stress on the cell membrane. They create transient, non-lethal holes in the plasma membrane, through which a drug/gene/label is able to diffuse into the cell (27-29). Acoustical pressure, sonication time, and SPIO incubation time play a role in safe and optimal endothelial cell labelling. The next step following the *in vitro* experiments should be *in vivo* experiments for real time targeted microbubble sonoporation. These can, for example, be performed with chicken embryos. Their chorioallantoic membrane (CAM) is a simple, highly vascularized extraembryonic membrane and is used to study angiogenesis and vascular biology (30). The CAM has great accessibility and is easy to handle for both intervention and imaging of the vasculature. SPIO labelling of the cells of the vessel wall can be monitored with a high speed camera. The microbubble behavior can be recorded and the cellular and tissue response might allow a better understanding of microbubble-drug-cell interaction.

Cancer cell imaging for diagnosis and therapy

Targeting of overexpressed receptors on the cell membrane of certain cells is applied in peptide radionuclide receptor therapy (PRRT) and imaging. A radioactive tracer is composed to target the receptor upon injection in the bloodstream, which can be visualised with a PET or SPECT scan. Availability of a tracer to target cells can be compromised for example by presence of enzymes that degrade the tracer. Too fast excretion of the tracer from blood is also problematic, because the time window for the tracer to reach the cell of interest is very short.

In **Chapter 5** we describe our research aiming to increase in vivo stability of an Indium-111 labelled radiopeptide targeting the gastrin-releasing peptide receptor (GRPR). This is a G-protein coupled receptor expressed at high density in a number of cancer types such as prostate cancer, breast cancer, and gastrointestinal cancer, which makes it an attractive target for peptide radionuclide receptor therapy (31, 32). Multiple GRPR radioligands have been synthesized during the past decade, mainly for the purpose of receptor-mediated nuclear imaging and therapy (33, 34). Our GRPR antagonist, Sarabesin-3, labelled with the positron-emitting radionuclide Gallium-68

8

has shown excellent receptor affinity and good *in vivo* stability. Preclinical as well as clinical PET imaging studies using [^{68}Ga]Ga-SB3 have been performed with success (35, 36); lesions in patients were visualized in about 50 % of the cases. For radio-guided tumour detection of malignant lesions, after injection of a radiopharmaceutical a handheld detection probe is used during surgery. Combining this intra-operative method with information from pre-operative imaging will allow accurate surgical guidance, ultimately improving surgical outcome while minimizing surgical invasiveness. We wanted SB-3 to be useful for both pre-operative imaging and intra-operative radio-guided tumour detection and therefore we labelled it with Indium-111. However, after labelling with Indium-111 the molecule shows poor *in vivo* stability (37). Radiopeptide integrity is challenged when injected into the circulation, by omnipresent proteolytic enzymes in the bloodstream. Enzymes also reside in organs, like liver, lungs, kidneys, and gastrointestinal tract, where radiopeptides are also exposed to. A neutral endopeptidase (NEP) inhibitor, such as phosphoramidon, can inhibit the enzymatic degradation of radiopeptides (38, 39). Phosphoramidon (PA) can be injected as a bolus together with a radiopeptide (40). The *in vivo* stability of [^{111}In]In-SB3 +/- PA was analysed in blood samples from mice. Radiotracer co-injected with PA showed twice as much circulating radioactivity consisting of intact radiotracer compared to that in control animals (no co-injection of PA), leading to 100% more intact tracer reaching the tumor at 1h post injection. At all-time points studied, there was significantly higher tumor uptake when PA was co-administered with [^{111}In]In-SB3. The radiotracer uptake in the tumour was receptor-specific as concluded from the significantly decreased uptake when an excess of unlabelled SB3 was co-administered. Injection with 25 MBq/200 pmol [^{111}In]In-SB3 +/- PA resulted in clearly improved tumour visualization with SPECT at all imaging time points when the radiotracer was combined with PA. After analysis of the images to determine the uptake of radioactivity (by drawing region of interest) an increase of 1.7 in signal intensity was shown when mice were injected with [^{111}In]In-SB3 + PA versus control animals. So, in vivo stabilization of [^{111}In]In-SB3 by inhibition of NEP resulted in higher tumour uptake. The radiopeptide uptake in the pancreas also increased when [^{111}In]In-SB3 was co-administered with PA, so the tumour to pancreas ratio remained unaffected. Nevertheless, high uptake in the pancreas should be kept in mind when the radiotracer would be used for radio-guided surgery of tumor lesions close

to the pancreas. The radioactivity washout from the pancreas was relatively fast, while tumour radioactivity uptake declined at a lower rate. So, the optimal time window for the best tumour:pancreas ratio for pre-operative and intra-operative tumour detection would be around 24 h post injection. For translation to the clinic of the PA/SB3 combination, the stability of SB3 +/- PA in humans should first be tested before the concept can be introduced in patients.

The success of PRRT depends on the amount of radioactivity delivered to the tumour in relation to the dose delivered to healthy tissues. To improve or widen the use of PRRT, there is a wide field of research ongoing (41). Other, more powerful, radionuclides (e,g, α-emitters) could be used (42, 43), various kinds of combination therapies can be given (43-45), the administration routes of the radiopeptide can be adjusted (46, 47), or the DNA damage response can be enhanced (48, 49).

One of the tracers widely used for PRRT is DOTA-Tyr^3-octreotate (DOTA-TATE) (50, 51). In the clinic we and many others apply radiolabelled DOTA-TATE to image and treat somatostatin receptor subtype 2 (SSTR2) positive, neuroendocrine tumours. For therapy [^{90}Y]Y-DOTA-Tyr^3-octreotide and [^{177}Lu] Lu-DOTA-Tyr^3-octreotate (51-53) are mostly used and the disease-control rates for these therapies are between 68–94% (54). The blood clearance of these tracers in humans is rapid (<10%ID in blood at 3 h post injection) (55). As there is no 100% response rate there is room to enhance the therapeutic efficacy. A higher dose in the tumor with the current tracer is not an option because concomitant higher radiation doses to other organs are also given. The organs at risk for long-term toxicity are predominantly the kidneys and the bone marrow. The renal radiation dose can however be reduced by co-infusion of a gelatin-based plasma expander (Gelofusine), leaving the bone marrow the main dose-limiting organ for treatment (56, 57). In **Chapter 6** we described how we aimed to further improve the biodistribution of radiolabelled DOTA-TATE by prolonging the tracer circulation time by adding an albumin binding domain to the radiopeptide. This new tracer is called Albutate-1 and is expected to have a longer circulation time in the blood stream according to our concept, possibly resulting in more uptake by the SSTR2 positive cells. We determined the characteristics of [^{111}In]In-albutate-1 and [^{177}Lu]Lu-albutate-1

8

analogue. Both DOTA-TATE and Albutate-1 showed a comparable high binding affinity for SST2 and a similar uptake and internalization rate of the tracers. After radiolabelling [^{111}In]In-Albutate-1 was stable for up to 3 days in labelling solution and at least for 24h in mouse serum. When tested *in vivo,* the circulation time of [^{177}Lu]Lu-Albutate-1 was $T_{1/2}$ = 27.5 h. We determined that for the dose tested a tumor absorbed dose per administered activity of 1455 mGy/MBq. This absorbed dose is 5 times higher than with [^{177}Lu]Lu-DOTA-TATE (unpublished data) and is the result of an extended exposure time to radiation. Normal organs however also encountered a higher absorbed dose, especially bone marrow. We calculated that the spine, which has a cellular fraction of 52%, received a total absorbed dose of 765 mGy/MBq. We conclude that addition of an albumin binding domain to [^{177}Lu]Lu-DOTA-TATE extended the blood circulation time and raised the tumor uptake. However, bone marrow, kidneys and all other organs received a high radiation dose, reducing the therapeutic index. Other groups also searched for the best balance between high tumor dose and limited organ dose using an albumin binding domain or Evans blue as albumin binder. In search for the best biodistribution profiles the structure of the tracer can be modified by varying the binding strength to albumin, and the spacer length. Preferred are a weaker binding strength and a shorter spacer length which both result in a shorter dissociation constant with a sub sequentially shorter circulation time (58-61). According to our results and other studies by other groups, attachment of albumin-binding domains to tracers can improve circulation time and increase tumor uptake. However, if the plasma protein-binding results in long dissociation times, the blood circulation time becomes extended to a level where all other organs also receive a high radiation dose, reducing the therapeutic index dramatically. Future perspectives are to create a tracer with more optimal pharmacokinetics, applying adaptations in albumin binding strength and spacer length.

Macrophage imaging during osteoarthritis development

As described in Chapters 5 and 6 tumor cells can be visualised using peptide radionuclide receptor imaging, but other cell populations that over-express receptors can be visualised the same way. Inflammatory cells, like macrophages, are of high interest, because they play a prominent role in the pathogenesis and progression of many different diseases and therefore form an interesting therapeutic target (62, 63).

Macrophages constitute an important cellular component of inflammatory diseases. Upon activation macrophages can differentiate, oversimplified stated, into pro- or anti- inflammatory macrophages (64). Macrophages can change their functional phenotype during their existence; these specific functional and phenotypic properties are affected by the micro-environment (65). Their varied roles can exacerbate and/or resolve diseases. The phagocytic nature, abundance and disease homing properties of macrophages can be targeted for imaging and therapeutic purposes. The ability to image specific phenotypes (pro- and anti-inflammatory macrophages) could help to predict disease progression or assess the stage of disease and considerably contribute to current disease treatment regimens (66).

Osteoarthritis (OA) has traditionally been thought to be a purely biomechanical disease, but in recent years there has been a shift in understanding how OA originates. Now it is seen as an inflammatory disease with macrophage involvement, however it is still unclear to what extent inflammation is an initiator versus an outcome of the joint destructive process. The contributions of different phenotypes of macrophages to OA pathogenesis are currently not well understood (67). It would be favourable to non-invasively trace the presence of different phenotypes of macrophages *in vivo* during OA development. A way to achieve this is by SPECT imaging. In **Chapter 7** we investigated the value of the somatostatin receptor subtype 2 as a novel imaging marker for pro-inflammatory macrophages also using the DMM osteoarthritic mouse model. First we evaluated gene expression levels of SST_2 in unstimulated as well as in IFNγ+TNFα stimulated human macrophages by qPCR. The expression of SST_2 mRNA significantly increased by a factor of 3.6 relative to that in unstimulated macrophages. A similar effect was also observed synovial tissue of OA patients. From patients with OA who got a knee resection synovial tissue was removed and stimulated *in vitro* with IFNγ+TNFα, resulting in a 10-fold increased expression level of SST_2 *mRNA* relative to that in unstimulated tissue. Moreover, stimulation of primary monocyte-derived macrophages with IFNγ+TNFα *in vitro* resulted in a significant increase of [^{111}In] In-DOTA-TATE uptake. To establish the relevance of SST2 tracer as a marker for pro-inflammatory macrophages in vivo, presence of macrophages and uptake of SST2 tracer was studied in a mouse DMM model for OA over time.

8

DMM and sham knees were histologically stained for CD64. The number of CD64 positive cells, indicating pro-inflammatory macrophages, was elevated at day 1 and 3, and slowly diminished during the following weeks. With SPECT, increased amounts of radioactivity were found in the knees, during the first 7 days after DMM surgery followed by a gradual decrease over time. Herein we saw a similar pattern for both the knees in which OA was induced by DMM and for the knees that underwent sham surgery. As shown in this study, the influx of macrophages was time dependent and associated with the development path of OA. Influx of macrophages was also observed in the sham-operated knee, most likely due to the inflammatory reaction to tissue damage caused by surgical manipulation. It should be noted that the sham knees had no structural cartilage damage or osteophyte formation. Synovium consists of a heterogeneous cell population including synoviocytes, macrophages and fibroblasts. Although it cannot fully be excluded that SST_2 tracer is taken up by cells other than macrophages, we consider this option highly unlikely to substantially contribute to the measured activity.

As said before, macrophages play a role in many different diseases, like also in inflammation of an atherosclerotic plaque. In the clinic different pilot studies have been performed with an SST_2 tracer to image atherosclerotic inflammation (68-70). These studies found that ^{68}Ga-DOTA-TATE PET enables measurement of generalized atherosclerotic disease activity and offers detailed information about local plaque functional phenotype. Imaging with ^{68}Ga-DOTA-TATE has therefore the potential to improve cardiovascular disease risk prediction. Despite we used an animal model resulting in only mild inflammation, we were already able to successfully visualize, quantify and monitor the inflammation process by SPECT/CT imaging. These findings are promising for the use of SST_2 targeting tracers in studying macrophage involvement in several disease processes. Macrophages are crucial in the development and progression of various diseases, so accurate imaging of pro-inflammatory macrophages, beside anti-inflammatory macrophages, might be an important step forward in understanding disease development.
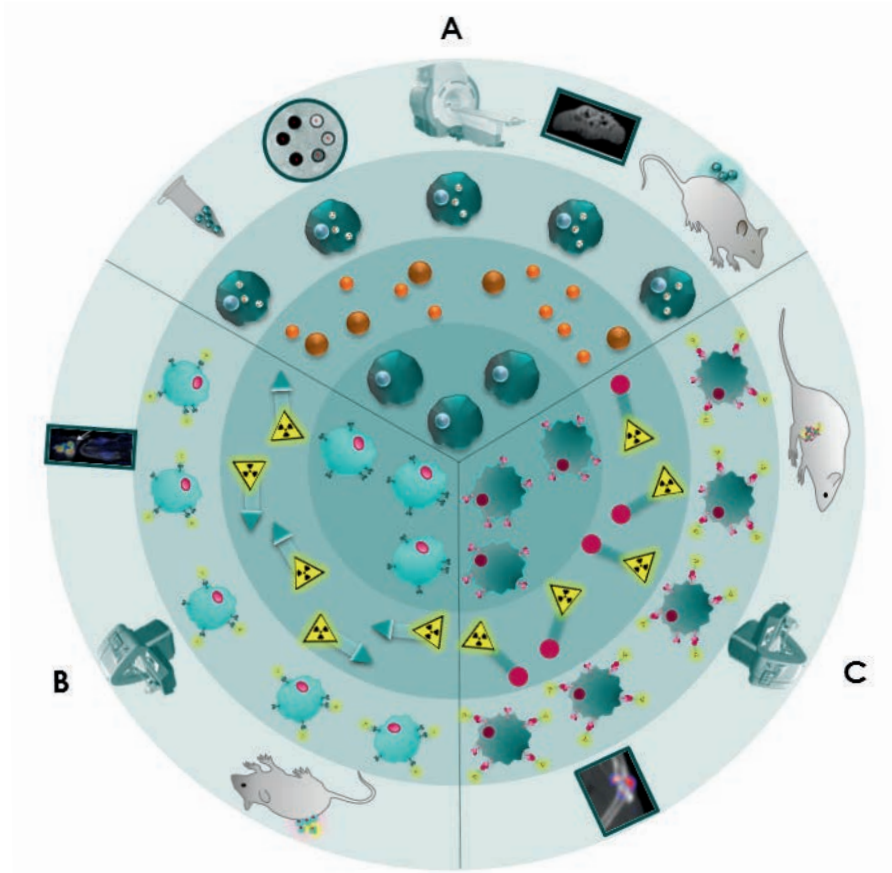
Figure 1 Cellular imaging in **A** regenerative medicine using iron labelled cells for MRI; **B** cancer cell imaging for PET or SPECT or therapy using radiolabelled cells; **C** macrophage imaging during osteoarthritis development using radiolabelled cells for PET or SPECT. Inner ring represents the cell used in research. Second ring shows the label. Third ring displays the labelled cells. Outer ring exhibits the model used with an example of an image obtained with the imaging modality applied.

8

Concluding remarks

In this thesis we showed different methods to label cells for cellular imaging to determine their role in diagnosis and therapy of various diseases (Fig. 1):

- *In vitro* cell labelling with iron nanoparticles appeared well feasible. We executed this method via non-specific targeting of the cells using a transfection agent or via specific targeting with the use of targeted ultrasound bubbles. Our labelling procedures did not harm the cells, but

in vivo tracking of superparamagnetic iron labelled cells showed some drawbacks especially when cell death, cell migration, cell division and extracellular SPIO accumulation occur simultaneously.

- Besides labelling of cells with iron nanoparticles, cells can also be labelled with a radioactive peptide tracer targeting e.g. a receptor. In this thesis work, we aimed for and achieved a longer circulation time of a radiopeptide by increasing *in vivo* stability (SB3) or by adding an albumin binding domain to the peptide molecule (Albutate-1). With either concepts one must realise that undesired tracer uptake in healthy organs may increase as well. Therefore this should always also be adequately determined.

- For inflammatory cell imaging we repurposed the currently widely available radiotracer for neuroendocrine tumor imaging ([^{111}In]In-DOTA-TATE, targeting the somatostatin receptor subtype 2) to distinguish between different inflammatory cell subtypes. This marker was elevated on an inflammatory cell subtypes as determined *in vitro* and in *in vivo*. Radioactive signal representative of tracer uptake could be measured in vivo in an inflammatory disease model, making this tracer useful for inflammatory cell imaging.

- The challenge for cellular imaging lies in the development/application of the ideal technique. No available imaging technique can currently address all research questions. Therefore, depending on the question(s) addressed, the most suitable technique or combination of techniques, i.e. using multiple modalities, will have to be selected. This will also include the most suitable label for a specific question.

References

1.   Stacy MR, Sinusas AJ. Emerging Imaging Modalities in Regenerative Medicine. Current Pathobiology Reports. 2015;3(1):27-36.

2.   Willadsen M, Chaise M, Yarovoy I, Zhang AQ, Parashurama N. Engineering molecular imaging strategies for regenerative medicine. Bioeng Transl Med. 2018;3(3):232-55.

3.   Arbab AS, Yocum GT, Kalish H, Jordan EK, Anderson SA, Khakoo AY, et al. Efficient magnetic cell labeling with protamine sulfate complexed to ferumoxides for cellular MRI. Blood. 2004;104(4):1217-23.

4.   Neri M, Maderna C, Cavazzin C, Deidda-Vigoriti V, Politi LS, Scotti G, et al. Efficient in vitro labeling of human neural precursor cells with superparamagnetic iron oxide particles: Relevance for in vivo cell tracking. Stem Cells. 2008;26(2):505-16.

5.   Zhang Z, van den Bos EJ, Wielopolski PA, de Jong-Popijus M, Bernsen MR, Duncker DJ, et al. In vitro imaging of single living human umbilical vein endothelial cells with a clinical 3.0-T MRI scanner. Magn Reson Mater Phy. 2005;18(4):175-85.

6.   Rodriguez O, Fricke S, Chien C, Dettin L, Vanmeter J, Shapiro E, et al. Contrast-Enhanced In Vivo Imaging of Breast and Prostate Cancer Cells by MRI. 2006;5(1):113-9.

7.   Shapiro EM, Skrtic S, Sharer K, Hill JM, Dunbar CE, Koretsky AP. MRI detection of single particles for cellular imaging. 2004;101(30):10901-6.

8.   De Vries IJM, Lesterhuis WJ, Barentsz JO, Verdijk P, Van Krieken JH, Boerman OC, et al. Magnetic resonance tracking of dendritic cells in melanoma patients for monitoring of cellular therapy. Nature Biotechnology. 2005;23(11):1407-13.

9.   Himes N, Min J-Y, Lee R, Brown C, Shea J, Huang X, et al. In vivo MRI of embryonic stem cells in a mouse model of myocardial infarction. 2004;52(5):1214-9.

10. Terrovitis J, Stuber M, Youssef A, Preece S, Leppo M, Kizana E, et al. Magnetic Resonance Imaging Overestimates Ferumoxide-Labeled Stem Cell Survival After Transplantation in the Heart. 2008;117(12):1555-62.

11. Pawelczyk E, Arbab AS, Chaudhry A, Balakumaran A, Robey PG, Frank JA. In Vitro Model of Bromodeoxyuridine or Iron Oxide Nanoparticle Uptake by Activated Macrophages from Labeled Stem Cells: Implications for Cellular Therapy. 2008;26(5):1366-75.

12. Walczak P, Kedziorek DA, Gilad AA, Barnett BP, Bulte JWM. Applicability and limitations of MR tracking of neural stem cells with asymmetric cell division and rapid turnover: The case of the Shiverer dysmyelinated mouse brain. 2007;58(2):261-9.

13. Winter EM, Hogers B, Van Der Graaf LM, Gittenberger-De Groot AC, Poelmann RE, Van Der Weerd L. Cell tracking using iron oxide fails to distinguish dead from living transplanted cells in the infarcted heart. 2010;63(3):817-21.

14. Küstermann E, Roell W, Breitbach M, Wecker S, Wiedermann D, Buehrle C, et al. Stem cell implantation in ischemic mouse heart: a high-resolution magnetic resonance imaging investigation. 2005;18(6):362-70.

15. Easo SL, Mohanan PV. In vitro hematological and in vivo immunotoxicity assessment of dextran stabilized iron oxide nanoparticles. 2015;134:122-30.

16. Wang Y-XJ, Zhu, Leung, Lee, Zhao, Wang, et al. Enhanced cellular uptake of aminosilane-coated superparamagnetic iron oxide nanoparticles in mammalian cell lines. 2012:953.

17. Huang D-M, Hsiao J-K, Chen Y-C, Chien L-Y, Yao M, Chen Y-K, et al. The promotion of human mesenchymal stem cell proliferation by superparamagnetic iron oxide nanoparticles. 2009;30(22):3645-51.

18. Singh N, Jenkins GJS, Asadi R, Doak SH. Potential toxicity of superparamagnetic iron oxide nanoparticles (SPION). Nano Reviews. 2010;1(1):5358.

19. Danhier P, Magat J, Levêque P, De Preter G, Porporato PE, Bouzin C, et al. In vivo visualization and ex vivo quantification of murine breast cancer cells in the mouse brain using MRI cell tracking and electron paramagnetic resonance. 2015;28(3):367-75.

8

20. Roose D, Leroux F, De Vocht N, Guglielmetti C, Pintelon I, Adriaensen D, et al. Multimodal imaging of micron-sized iron oxide particles following in vitro and in vivo uptake by stem cells: down to the nanometer scale. 2014;9(6):400-8.

21. Shapiro EM, Skrtic S, Koretsky AP. Sizing it up: Cellular MRI using micron-sized iron oxide particles. 2005;53(2):329-38.

22. Gilad AA, Winnard PT, Van Zijl PCM, Bulte JWM. Developing MR reporter genes: promises and pitfalls. 2007;20(3):275-90.

23. Genove G, DeMarco U, Xu H, Goins WF, Ahrens ET. A new transgene reporter for in vivo magnetic resonance imaging. Nat Med. 2005;11(4):450-4.

24. Chapelin F, Capitini CM, Ahrens ET. Fluorine-19 MRI for detection and quantification of immune cell therapy for cancer. Journal for ImmunoTherapy of Cancer. 2018;6(1).

25. Srinivas M, Heerschap A, Ahrens ET, Figdor CG, Vries IJMD. 19F MRI for quantitative in vivo cell tracking. 2010;28(7):363-70.

26. Fox M, Gaudet J, Foster P. Fluorine-19 MRI Contrast Agents for Cell Tracking and Lung Imaging. 2016;53.

27. Ferrara K, Pollard R, Borden M. Ultrasound Microbubble Contrast Agents: Fundamentals and Application to Gene and Drug Delivery. Annual Review of Biomedical Engineering. 2007;9(1):415-47.

28. Lentacker I, De Cock I, Deckers R, De Smedt SC, Moonen CTW. Understanding ultrasound induced sonoporation: Definitions and underlying mechanisms. Advanced Drug Delivery Reviews. 2014;72:49-64.

29. Kooiman K, Vos HJ, Versluis M, De Jong N. Acoustic behavior of microbubbles and implications for drug delivery. 2014;72:28-48.

30. Nowak-Sliwinska P, Segura T, Iruela-Arispe ML. The chicken chorioallantoic membrane model in biology, medicine and bioengineering. 2014;17(4):779-804.

31. Jensen RT, Battey JF, Spindel ER, Benya RV. International Union of Pharmacology. LXVIII. Mammalian bombesin receptors: nomenclature, distribution, pharmacology, signaling, and functions in normal and disease states. Pharmacol Rev. 2008;60(1):1-42.

32. Reubi JC, Wenger S, Schmuckli-Maurer J, Schaer JC, Gugger M. Bombesin receptor subtypes in human cancers: detection with the universal radioligand (125)I-[D-TYR(6), beta-ALA(11), PHE(13), NLE(14)] bombesin(6-14). Clin Cancer Res. 2002;8(4):1139-1146.

33. Sancho V, Di Florio A, Moody TW, Jensen RT. Bombesin receptor-mediated imaging and cytotoxicity: review and current status. Current drug delivery. 2011;8(1):79-134.

34. Moreno P, Ramos-Álvarez I, Moody TW, Jensen RT. Bombesin related peptides/receptors and their promising therapeutic roles in cancer imaging, targeting and treatment. 2016;20(9):1055-73.

35. Maina T, Bergsma H, Kulkarni HR, Mueller D, Charalambidis D, Krenning EP, et al. Preclinical and first clinical experience with the gastrin-releasing peptide receptor-antagonist [68Ga]SB3 and PET/CT. 2015.

36. Bakker I FA, Busstra MB et al PET imaging of prostate cancer using the GRPr-targeting ligand Sarabesin-3 prior to radical prostatectomy [abstract]. Eur J Nucl Med Mol Imaging. 2016;43:S1-S734.

37. Lymperis E M-NT, Kaloudi A et al. Transient in vivo NEP inhibition enhances the theranostic potential of the new GRPR antagonist [111In/177Lu]SB3 [abstract]. Eur J Nucl Med. 2014;41(s319).

38. Nock BA, Maina T, Krenning EP, De Jong M. "To Serve and Protect": Enzyme Inhibitors as Radiopeptide Escorts Promote Tumor Targeting. 2014;55(1):121-7.

39. Roques BP, Noble F, Daugé V, Fournié-Zaluski MC, Beaumont A. Neutral endopeptidase 24.11: structure, inhibition, and experimental and clinical pharmacology. Pharmacological Reviews. 1993;45(1):87-146.

40. Kaloudi A, Nock BA, Lymperis E, Krenning EP, De Jong M, Maina T. Improving the In Vivo Profile of Minigastrin Radiotracers: A Comparative Study Involving the Neutral Endopeptidase Inhibitor Phosphoramidon. 2016;31(1):20-8.

41. Adant S, Shah GM, Beauregard J-M. Combination treatments to enhance peptide receptor radionu-clide therapy of neuroendocrine tumours. Eur J Nucl Med Mol I. 2019.

42. Chan HS, de Blois E, Morgenstern A, Bruchertseifer F, de Jong M, Breeman W, et al. In Vitro comparison of 213Bi- and 177Lu-radiation for peptide receptor radionuclide therapy. PLoS One. 2017;12(7):e0181473.

43. Bison SM, Konijnenberg MW, Melis M, Pool SE, Bernsen MR, Teunissen JJM, et al. Peptide receptor radionuclide therapy using radiolabeled somatostatin analogs: focus on future developments. Clinical and Translational Imaging. 2014;2(1):55-66.

44. Fueger BJ, Hamilton G, Raderer M, Pangerl T, Traub T, Angelberger P, et al. Effects of chemotherapeutic agents on expression of somatostatin receptors in pancreatic tumor cells. J Nucl Med. 2001;42(12):1856-62.

45. Basu S, Ostwal V. Observation on enhanced avidity on somatostatin receptor targeted 68Ga-DOTATATE PET-CT following therapy with everolimus and capecitabine-temozolamide: is redifferentiation akin phenomenon a reality in neuroendocrine tumors? Nucl Med Commun. 2016;37(6):669-71.

46. Chatalic KL, Kwekkeboom DJ, de Jong M. Radiopeptides for Imaging and Therapy: A Radiant Future. J Nucl Med. 2015;56(12):1809-12.

47. Pool SE, Kam BL, Koning GA, Konijnenberg M, Ten Hagen TL, Breeman WA, et al. [(111)In-DTPA] octreotide tumor uptake in GEPNET liver metastases after intra-arterial administration: an overview of preclinical and clinical observations and implications for tumor radiation dose after peptide radionuclide therapy. Cancer Biother Radiopharm. 2014;29(4):179-87.

48. Nonnekens J, van Kranenburg M, Beerens CE, Suker M, Doukas M, van Eijck CH, et al. Potentiation of Peptide Receptor Radionuclide Therapy by the PARP Inhibitor Olaparib. Theranostics. 2016;6(11):1821-32.

49. Mark. Targeting the DNA Damage Response in Cancer. Molecular Cell. 2015;60(4):547-60.

50. Pencharz D, Gnanasegaran G, Navalkissoor S. Theranostics in neuroendocrine tumours: somatostatin receptor imaging and therapy. Br J Radiol. 2018;91(1091):20180108.

51. Hennrich U, Kopka K. Lutathera®: The First FDA- and EMA-Approved Radiopharmaceutical for Peptide Receptor Radionuclide Therapy. Pharmaceuticals. 2019;12(3):114.

52. Kolasinska Ć, Pęczkowska, Ćwikła, Michałowska, Pałucki, Bodei, et al. A Clinical Efficacy of PRRT in Patients with Advanced, Nonresectable, Paraganglioma-Pheochromocytoma, Related to SDHx Gene Mutation. Journal of Clinical Medicine. 2019;8(7):952.

53. Severi S, Grassi I, Nicolini S, Sansovini M, Bongiovanni A, Paganelli G. Peptide receptor radionuclide therapy in the management of gastrointestinal neuroendocrine tumors: efficacy profile, safety, and quality of life. Onco Targets Ther. 2017;10:551-7.

54. Bodei L, Kwekkeboom DJ, Kidd M, Modlin IM, Krenning EP. Radiolabeled Somatostatin Analogue Therapy Of Gastroenteropancreatic Cancer. 2016;46(3):225-38.

55. Esser JP, Krenning EP, Teunissen JJM, Kooij PPM, Van Gameren ALH, Bakker WH, et al. Comparison of [177Lu-DOTA0,Tyr3]octreotate and [177Lu-DOTA0,Tyr3]octreotide: which peptide is preferable for PRRT? 2006;33(11):1346-51.

56. Rolleman EJ, Melis M, Valkema R, Boerman OC, Krenning EP, De Jong M. Kidney protection during peptide receptor radionuclide therapy with somatostatin analogues. Eur J Nucl Med Mol I. 2010;37(5):1018-31.

57. Melis M, Bijster M, De Visser M, Konijnenberg MW, De Swart J, Rolleman EJ, et al. Dose-response effect of Gelofusine on renal uptake and retention of radiolabelled octreotate in rats with CA20948 tumours. 2009;36(12):1968-76.

58. Siwowska K, Haller S, Bortoli F, Benesova M, Groehn V, Bernhardt P, et al. Preclinical Comparison of Albumin-Binding Radiofolates: Impact of Linker Entities on the in Vitro and in Vivo Properties. Mol Pharm. 2017;14(2):523-32.

59. Vegt E, de Jong M, Wetzels JF, Masereeuw R, Melis M, Oyen WJ, et al. Renal toxicity of radiolabeled peptides and antibody fragments: mechanisms, impact on radionuclide therapy, and strategies for prevention. J Nucl Med. 2010;51(7):1049-58.

8

60. Benesova M, Umbricht CA, Schibli R, Muller C. Albumin-Binding PSMA Ligands: Optimization of the Tissue Distribution Profile. Mol Pharm. 2018;15(3):934-46.

61. Umbricht CA, Benesova M, Schibli R, Muller C. Preclinical Development of Novel PSMA-Targeting Radioligands: Modulation of Albumin-Binding Properties To Improve Prostate Cancer Therapy. Mol Pharm. 2018;15(6):2297-306.

62. Taghizadeh E, Taheri F, Renani PG, Reiner Z, Navashenaq JG, Sahebkar A. Macrophage: A Key Therapeutic Target in Atherosclerosis? Curr Pharm Des. 2019;25(29):3165-74.

63. Gordon S. The Macrophage as Therapeutic Target: Springer; 2003.

64. Mosser DM, Edwards JP. Exploring the full spectrum of macrophage activation. Nat Rev Immunol. 2008;8(12):958-69.

65. Stout RD, Jiang C, Matta B, Tietzel I, Watkins SK, Suttles J. Macrophages Sequentially Change Their Functional Phenotype in Response to Changes in Microenvironmental Influences. The Journal of Immunology. 2005;175(1):342-9.

66. Patel SK, Janjic JM. Macrophage targeted theranostics as personalized nanomedicine strategies for inflammatory diseases. Theranostics. 2015;5(2):150-72.

67. Orlowsky EW, Kraus VB. The role of innate immunity in osteoarthritis: when our first line of defense goes on the offensive. J Rheumatol. 2015;42(3):363-71.

68. Tarkin JM, Joshi FR, Evans NR, Chowdhury MM, Figg NL, Shah AV, et al. Detection of Atherosclerotic Inflammation by 68 Ga-DOTATATE PET Compared to [18 F]FDG PET Imaging. Journal of the American College of Cardiology. 2017;69(14):1774-91.

69. Mojtahedi A, Alavi A, Thamake S, Amerinia R, Ranganathan D, Tworowska I, et al. Assessment of vulnerable atherosclerotic and fibrotic plaques in coronary arteries using (68)Ga-DOTATATE PET/CT. Am J Nucl Med Mol Imaging. 2015;5(1):65-71.

70. Rominger A, Saam T, Vogl E, Ubleis C, La Fougere C, Forster S, et al. In Vivo Imaging of Macrophage Activity in the Coronary Arteries Using 68Ga-DOTATATE PET/CT: Correlation with Coronary Calcium Burden and Risk Factors. 2010;51(2):193-7.

9

Nederlandse samenvatting

Nederlandse samenvatting

Voor dit proefschrift hebben we preklinische studies uitgevoerd in verschillende ziektemodellen met verschillende niveaus van complexiteit. Het uiteindelijk doel was het optimaliseren van beeldvorming van cellen in regeneratieve geneeskunde, kanker en artrose. Beeldvorming werd uitgevoerd met magnetic resonance imaging (MRI), single photon emission computed tomography (SPECT) en computed tomography (CT). In **Hoofdstuk 1** wordt een algemene inleiding gegeven over moleculaire beeldvorming. We beschrijven beeldvormende apparaten die worden gebruikt en strategieën die kunnen worden toegepast voor cellabeling.

Cellulaire beeldvorming in regeneratieve geneeskunde
Regeneratieve geneeskunde richt zich op herstel, vervanging of regeneratie van beschadigt weefsel om functies te herstellen. Verminderde functies kunnen worden veroorzaakt door aangeboren afwijkingen, maar ook door ziekte, trauma en veroudering. Bij gebruik van celtherapie is kennis van de juiste lokalisatie van getransplanteerde cellen essentieel. Het volgen van het lot van getransplanteerde cellen en het meten van hun therapeutisch effecten (bijv. verbeterde hartfunctie) is cruciaal om de werkzaamheid van celtherapie vast te stellen. We hebben verschillende methoden onderzocht voor cellabeling en beeldvorming. Eén methode die als zeer efficiënt wordt beschouwd, en mogelijk in de kliniek te gebruiken is, is het labelen van de cellen met ijzeroxide-partikels. Dergelijke ijzeroxide-partikels resulteren in een lokale verandering van het MRI-signaal en maken zeer gevoelige driedimensionale detectie van gelabelde cellen mogelijk. Zoals beschreven in de hoofdstukken 2, 3 en 4 kunnen verschillende soorten ijzeroxide-partikels worden gebruikt. In ons onderzoek zijn twee soorten partikels toegepast; Ferumoxide, super paramagnetische ijzeroxide-partikels (SPIO) en de grotere paramagnetische ijzeroxide-partikels (MPIO). De ijzeroxidekernen van zowel SPIO als MPIO hebben een sterk magnetisch moment, waardoor het lokale magnetische veld in MRI wordt verstoord, hetgeen resulteert in lokaal signaalverlies in MR-beelden. De doeltreffendheid van deze deeltjes voor cellabel- en beeldvormingsstudies werd onderzocht door variaties in de labelingprotocollen voor ijzeroxide-partikels en de invloed daarvan op opname, distributie en retentie, zoals beschreven in **Hoofdstuk 2**. Gekweekte

menselijke navelstrengcellen (HUVECs) werden gelabeld met ijzerpartikels. De gemiddelde SPIO-opname nam toe wanneer de incubatietijd werd verlengd van 4 uur tot 24 uur. Het optimale labelingprotocol in deze studie resulteerde in 12,0 pg ijzer/per cel. Voor MPIO-labeling was de incubatietijd van minder belang, aangezien de meeste deeltjes al binnen 4 uur in de cel waren opgenomen, met een labelefficiëntie van 100% en een intracellulaire ijzeropname tot 626 pg ijzer/cel. MPIO werden efficiënter opgenomen, werden beter verdragen (geen significante celdood) en hadden een veel sterker effect op het uiterlijk van de cel dan SPIO. Een nadeel van het gebruik van de grotere MPIO-partikels is dat er minder partikels per cel opgenomen worden. Wanneer cellen delen, zal niet elke dochtercel MPIO-partikels bevatten. Dit resulteert in het niet verder kunnen volgen van deze cellen. Optimale cellabeling vereiste verschillende protocollen voor SPIO en MPIO. Er kon geen standaard labelingprotocol worden gebruikt voor verschillende celtypen *in vitro*. Het gemak waarmee ijzeroxidepartikels spontaan werden opgenomen verschilde per cellijn, ook verschilde de snelheid van de opname van ijzeroxidepartikels en de getolereerde hoeveelheid ijzeroxidepartikels in de cel. De ijzeroxidepartikels in de cellen kunnen worden gevisualiseerd met MRI; de ijzeroxide partikels hebben een effect op verschillende MRI-parameters (bijv. R2' (R2 * -R2) = relaxiviteit). Cellabeling met ijzeroxidepartikels biedt dus een veelbelovende methode voor het *in vivo* volgen van cellen in mens en dier door middel van MRI. Verschillende processen kunnen optreden wanneer met ijzer gelabelde cellen *in vivo* worden geïnjecteerd, zoals celdood, celmigratie en celdeling, die allemaal de signaalintensiteit beïnvloeden. Het nabootsen van deze biologisch relevante processen werd uitgevoerd door cellen te labelen met kleine (SPIO) en grotere (MPIO) ijzeroxidepartikels; de uitgevoerde experimenten en de resultaten worden beschreven in **Hoofdstuk 3**. Voor de MR-metingen werden fantomen gemaakt. Als model voor het *in vivo* delen van cellen werden Brown Norway 175 sarcoomcellen gelabeld met SPIO en subcutaan geïnjecteerd in de flank van een rat. De effecten van ruimtelijke distributie en compartimentering van de ijzeroxidepartikels op de relaxiviteit werden geanalyseerd. We hebben aangetoond dat relaxometrie geen kwantificering van gelabelde cellen toelaat wanneer meerdere fysiologische processen, zoals celdeling en celmigratie, tegelijk plaats vinden. De veranderingen in relaxiviteit van ijzeroxidepartikels bleken afhankelijk van de omgeving. De intensiteit van de met ijzer gelabelde cellen nam af naarmate ijzeroxide werd verdund door proliferatie. Voor

9

MR-beeldvorming van bijvoorbeeld tumorvasculatuur en weefsel-gemanipuleerde vaatstructuren, zou het gunstig zijn om cellen *in vivo* te labelen in plaats van, zoals eerder beschreven, *in vitro* met ijzeroxide partikels. Veranderingen in vascularisatie en vasculaire disfunctie zouden ziekteontwikkeling kunnen onthullen en het is daarom van belang om deze processen in beeld te brengen. Ons doel van het *in vitro* onderzoek beschreven in **Hoofdstuk 4** was om optimale parameters te vinden voor niet-invasieve, CD31-gerichte (CD31 is een biomarker op endotheelcelmembranen), door microbellen uitgevoerde SPIO-labeling van endotheelcellen. Bij toepassing van ultrageluid oscilleerden de microbellen door opeenvolgende compressie en uitzetting veroorzaakt door drukvariaties. Op deze manier werd de permeabiliteit van het celmembraan vergroot, omdat de microbellen zogenaamde shear stress (afschuifspanning) op het celmembraan veroorzaken. Ze creëren kortstondige, niet-dodelijke gaten in het plasmamembraan, waardoor een medicijn/gen/label in de cel kan diffunderen. Labelen van endotheelcellen op deze manier is mogelijk, maar akoestische druk, sonicatietijd en SPIO-incubatietijd spelen ook een rol bij het veilig en optimaal labelen van endotheelcellen.

Beeldvorming van kankercellen voor diagnose en therapie

Targeting van tot overexpressie gebrachte receptoren op het celmembraan van bepaalde cellen wordt toegepast bij peptide-radionuclide-receptor-therapie (PRRT) en bij beeldvorming. Een radioactieve tracer is zo samengesteld dat het kan binden aan een receptor op een cel na injectie in de bloedbaan, hetgeen daarna kan worden gevisualiseerd met een PET of SPECT scan. De mogelijkheid van een tracer om aan een receptor te binden kan worden verhinderd, bijvoorbeeld door de aanwezigheid van enzymen die de tracer afbreken. Te snelle uitscheiding van de tracer uit bloed is ook problematisch, omdat dan de tijd waarin de tracer de cel kan bereiken te kort is. In **Hoofdstuk 5** beschrijven we ons onderzoek dat gericht is op het verhogen van de *in vivo* stabiliteit van een met Indium-111 gelabeld radiopeptide gericht tegen de gastrine-releasing peptidereceptor (GRPR). Dit is een receptor die met hoge dichtheid tot expressie wordt gebracht in een aantal kankertypes, zoals prostaatkanker, borstkanker en gastro-intestinale kanker, wat het tot een aantrekkelijk doelwit maakt voor therapie met radiopeptiden. Onze GRPR-antagonist, Sarabesin-3, gelabeld met het positron-emitterende radionuclide

Gallium-68, heeft een uitstekende receptoraffiniteit en goede *in vivo* stabiliteit getoond. Zowel preklinische als klinische PET studies met [^{68}Ga]Ga-SB3 zijn met succes uitgevoerd. Laesies bij patiënten in vergevorderde staat van ziekte werden in ongeveer 50% van de gevallen zichtbaar gemaakt. Voor radiogestuurde tumordetectie van kwaadaardige laesies wordt na injectie van een radiofarmacon tijdens chirurgie een draagbare detectiesonde gebruikt. Door deze intra-operatieve methode te combineren met informatie van preoperatieve beeldvorming, kan nauwkeurige chirurgische begeleiding worden verkregen, waardoor uiteindelijk de chirurgische uitkomst wordt verbeterd en de chirurgische invasiviteit wordt geminimaliseerd. Ons doel was SB-3 geschikt te maken voor zowel preoperatieve beeldvorming als intra-operatieve radio-gestuurde tumordetectie, daarom hebben we het peptide gelabeld met Indium-111. Na het labelen met Indium-111 vertoonde het molecuul helaas een slechte *in vivo* stabiliteit. De integriteit van het radiopeptide wordt bij injectie in de bloedsomloop op de proef gesteld door alom aanwezige proteolytische enzymen. Enzymen bevinden zich ook in organen, zoals lever, longen, nieren en maagdarmkanaal. Een neutrale endopeptidase (NEP) remmer, zoals phosphoramidon (PA), kan de enzymatische afbraak van radiopeptiden remmen. De *in vivo* stabiliteit van [^{111}In] In-SB3 +/- PA werd geanalyseerd in bloedmonsters van muizen. De radiotracer die gelijktijdig met PA werd geïnjecteerd, bleef 100% meer intact dan in controle dieren (geen co-injectie van PA). Dit leidde vervolgens tot 100% meer intacte tracer die de tumor bereikte 1 uur na injectie. Op alle onderzochte tijdspunten zagen we een significant hogere tumoropname wanneer PA gelijktijdig werd toegediend met [^{111}In]In-SB3. De opname van radiotracer in de tumor was receptor-specifiek, zoals werd geconcludeerd uit de significant verminderde opname wanneer een overmaat aan niet-gelabeld SB3 gelijktijdig werd toegediend. Injectie met 25 MBq/200 pmol [^{111}In]In-SB3 +/- PA resulteerde in duidelijk verbeterde tumorvisualisatie op alle tijdstippen na injectie wanneer de radiotracer werd gecombineerd met PA. De opname van het radiopeptide in de alvleesklier nam ook toe, zodat de verhouding tussen tumor en alvleesklier onaangetast bleef. Toch moet een hoge opname in de alvleesklier in gedachten worden gehouden wanneer de radiotracer zou worden gebruikt voor radiogestuurde chirurgie van tumorlaesies in de buurt van de alvleesklier. Het uitwassen van radioactiviteit uit de alvleesklier was echter relatief snel, terwijl de tumorradioactiviteit in een lager tempo afnam.

9

Het optimale tijdvenster voor de beste verhouding tumor: pancreas voor preoperatieve en intra-operatieve tumordetectie zou waarschijnlijk ongeveer 24 uur na injectie zijn.

Het succes van PRRT hangt af van de hoeveelheid radioactiviteit die aan de tumor wordt afgegeven in verhouding tot de dosis die aan relevante gezonde weefsels wordt afgegeven. Om het gebruik van PRRT te verbeteren of breder in te kunnen zetten, is nog veel onderzoek nodig. Eén van de tracers die veel voor PRRT wordt gebruikt is DOTA-Tyr³-octreotaat (DOTA-TATE). In de kliniek passen wij, en vele anderen, radioactief gelabelde DOTA-TATE toe om neuro-endocriene somatostatine receptor-subtype 2 (SSTR2)-positieve tumoren in beeld te brengen en te behandelen. De tumorrespons voor deze therapie ligt tussen 68 en 94%. De bloedklaring van deze tracer, bij de mens, is snel (<10% geïnjecteerde dosis in het bloed na 3 uur). Aangezien er geen 100% volledige tumorrespons is, is er ruimte om de therapeutische werkzaamheid te verbeteren met bijvoorbeeld hogere doses van het radiofarmacon, maar dit wordt beperkt door gelijktijdige hogere stralingsdoses op andere organen. De organen die op lange termijn risico lopen op toxiciteit zijn voornamelijk de nieren en het beenmerg. De nierdosis kan echter worden verlaagd door bijv. co-infusie van een op gelatine gebaseerde plasma-expander (Gelofusine). Het beenmerg blijft dan het belangrijkste dosis beperkende orgaan gedurende de behandeling. In **Hoofdstuk 6** beschrijven we hoe we de biologische distributie van radioactief gelabelde DOTA-TATE verder wilden verbeteren door de circulatietijd van de tracer te verlengen door een albumine-bindend domein aan het radiopeptide te koppelen. De resulterende tracer is Albutate-1 en zal volgens ons concept naar verwachting een langere circulatietijd in de bloedbaan hebben, mogelijk resulterend in meer opname door de tumorcellen. We bepaalden de kenmerken van [¹¹¹In]In-DOTA-Tyr³-albutate-1 en [¹⁷⁷Lu]Lu-DOTA-Tyr³-albutate-1. Zowel DOTA-TATE als Albutate-1 vertoonde een vergelijkbare hoge bindingsaffiniteit voor SSTR2 en een vergelijkbare opname- en internalisatie snelheid van de tracers. Na radioactief labelen was [¹¹¹In]In-Albutate-1 tot 3 dagen stabiel in labeling-oplossing en tenminste 24 uur in muizenserum. Bij *in vivo* testen was de circulatietijd van [¹⁷⁷Lu]Lu-Albutate-1 $T_{1/2}$ = 27,5 uur. We berekenden dat de tumor geabsorbeerde dosis per toegediende activiteit 1455 mGy/MBq was, sterk verhoogd t.o.v. de tracer zonder albumine bindend domein. Normale organen

ontvingen echter ook een hogere geabsorbeerde dosis, vooral het beenmerg. We berekenden dat de wervelkolom een totale geabsorbeerde dosis van 765 mGy/MBq ontving, een forse dosis. We concludeerden dat toevoeging van een albumine-bindend domein aan [^{177}Lu]Lu-DOTA-TATE de bloedcirculatietijd sterk verlengde en de tumoropname verhoogde. Beenmerg, nieren en alle andere organen kregen echter ook een hogere stralingsdosis, waardoor de therapeutische index helaas daalde.

Macrofaagbeeldvorming tijdens de ontwikkeling van artrose

Zoals beschreven in hoofdstukken 5 en 6 kunnen tumorcellen worden gevisualiseerd met behulp van peptide-radionuclide receptorbeeldvorming, maar ook andere celpopulaties die receptoren tot overexpressie brengen kunnen op deze manier worden gevisualiseerd. Ontstekingscellen, zoals macrofagen, zijn van groot belang omdat ze een prominente rol spelen in het ontstaan, ontwikkelen en verloop van veel verschillende ziekten, ze vormen daarom een interessant therapeutisch doelwit. Macrofagen vormen een belangrijk cellulair onderdeel van ontstekingsziekten. Bij activering kunnen macrofagen differentiëren, zoals vereenvoudigd wordt aangegeven, in pro- of anti-ontstekingsremmende macrofagen. Macrofagen kunnen tijdens hun bestaan hun functionele fenotype veranderen. Deze specifieke functionele en fenotypische eigenschappen worden beïnvloed door de micro-omgeving en deze uiteenlopende rollen kunnen ziekten verergeren en/of oplossen. Hun fagocytotische aard, overvloedige aanwezigheid en migratie naar plaatsen met disbalans kunnen worden gebruikt voor beeldvorming en therapeutische doeleinden. Het vermogen om specifieke fenotypen af te beelden (pro- en anti-ontstekingsremmende macrofagen) zou kunnen helpen de ziektevoortgang te voorspellen of het ziektestadium te beoordelen en zou aanzienlijk kunnen bijdragen aan de huidige behandelingsregimes van de ziekte. Van artrose (OA) werd traditioneel gedacht dat het een puur biomechanische ziekte is, maar de laatste jaren is er een verschuiving ontstaan in het begrijpen hoe OA ontstaat. Nu wordt het gezien als een ontstekingsziekte waarbij macrofagen betrokken zijn, maar het is nog steeds onduidelijk in hoeverre ontsteking een initiator is versus een resultaat van het gezamenlijke destructieve proces. De bijdragen van verschillende fenotypen van macrofagen aan het ontstaan, ontwikkeling en verloop van OA zijn momenteel niet goed bekend. Het zou gunstig zijn om de aanwezigheid van macrofagen *in vivo* tijdens OA ontwikkeling niet-invasief

9

te kunnen traceren. Een manier om dit te bereiken is door SPECT beeldvorming. In **Hoofdstuk 7** hebben we de waarde van de SSTR2 onderzocht als een nieuwe beeldvormingsmarker voor pro-inflammatoire macrofagen, opnieuw met behulp van het DMM artrose muismodel. Eerst evalueerden we de genexpressie niveaus van *SSTR2*, in zowel niet-gestimuleerde als in interferon gamma (IFNγ) en tumor necrose factor alfa (TNFα) gestimuleerde menselijke macrofagen, door middel van een kwantitatieve polymerasekettingreactie. De expressie van *SSTR2* mRNA nam significant toe met een factor 3,6 ten opzichte van die in niet-gestimuleerde macrofagen. Een soortgelijk effect werd ook waargenomen bij synoviaal weefsel van OA patiënten. Bovendien resulteerde stimulatie van primaire monocyten afgeleide macrofagen met IFNγ + TNFα *in vitro* in een significante toename van [¹¹¹In]In-DOTA-TATE opname. Om de relevantie van SSTR2 tracer als een marker voor pro-inflammatoire macrofagen *in vivo* vast te stellen, werd de aanwezigheid van macrofagen en opname van SSTR2 tracer in de tijd bestudeerd in een DMM muismodel voor OA. DMM en sham geopereerde knieën werden histologisch gekleurd voor CD64. Het aantal CD64-positieve cellen, wat wijst op pro-inflammatoire macrofagen, was op dag 1 en 3 verhoogd en nam de daarop volgende weken langzaam af. Voor ons *in vivo* beeldvormend onderzoek zijn scans met hoge resolutie van het grootste belang, omdat het doelwit erg klein is (knie van een muis). Daarom hebben we een met indium-111 gelabelde tracer gebruikt. Indium-111 is een radionuclide dat gebruikt wordt met SPECT, een techniek die in de prekliniek een hogere spatiele resolutie heeft dan preklinische PET. Met SPECT werden verhoogde hoeveelheden radioactiviteit gevonden in de knieën gedurende de eerste 7 dagen na DMM chirurgie, gevolgd door een geleidelijke afname in de tijd. Hierin zagen we een soortgelijk patroon voor zowel de knieën waarin artrose werd veroorzaakt door DMM als voor de knieën die een sham-operatie ondergingen. Zoals in deze studie werd aangetoond, was de instroom van macrofagen tijdsafhankelijk en geassocieerd met de ontwikkeling van artrose. Instroom van macrofagen werd ook waargenomen in de sham-knie, waarschijnlijk als gevolg van de ontstekingsreactie op weefselschade veroorzaakt door chirurgische manipulatie. Opgemerkt moet worden dat de sham knieën geen structurele kraakbeenschade of osteofyt vorming vertoonden.

De uitdaging voor cellulaire beeldvorming ligt in de ontwikkeling / toepassing van de ideale techniek. Geen enkele beschikbare beeldvormende techniek kan op dit moment alle beeldvorming-gerelateerde onderzoeksvragen beantwoorden. Daarom zal, afhankelijk van de vraag, de meest geschikte techniek of combinatie van technieken, d.w.z. met gebruikmaking van meerdere modaliteiten, moeten worden gekozen. Dit includeert ook het meest geschikte label en het beste model voor een specifieke vraag.

9

11

PhD Portfolio

PhD Portfolio

Name	Sandra T. van Tiel
Erasmus MC Department	Radiology & Nuclear Medicine
Research School	Molecular Medicine
Promotor	Prof. dr. ir. M. Hendriks-de Jong
Co-promotor	Dr. M. R. Bernsen

Courses	Year	ECTs
The monocytes: origins, destinations, functions and diagnostic targets	2017	0,2
Excel, basic	2016	0,3
Excel, advanced	2016	0,4
Photoshop and Illustrator CC	2016	0,3
Biomedical English writing course	2015	2
Pubmed	2015	0,6
Graph pad prism	2015	0,3
Endnote	2015	0,2
EMBASE/Ovid	2015	0,3
Research integrity	2015	0,3
Article 9, laboratory animal science	2014	3
Probes and models for imaging diseases and therapy	2013	2,3

Workshop	Year	ECTs
NKRV, Eindhoven	2019	0,3
NKRV, Rotterdam	2019	0,3
NKRV, Delft	2016	0,3
Immuno-imaging and Molecular Therapy	2016	1,5
NKRV, Amsterdam	2015	0,3
Molecular Medicine day	2014	0,3
Departmental research meeting	2013	0,15

Conferences	Year	ECTs
EANM, Barcelona, Spain	2019	1,2
MI Labs user meeting, De Bilt	2019	0,3

EMIM, Glasgow, Great Brittan	2019	1
EANM, Dusseldorf, Germany	2018	1,2
EANM, Vienna, Austria	2017	1,2
MI Labs user meeting, Utrecht	2017	0,3
MI Labs user meeting, Utrecht	2016	0,3
EMIM, Utrecht	2016	1
EANM, Hamburg, Germany	2015	1,2
MI Labs user meeting, Utrecht	2014	0,3
EMIM, Torino, Italy	2013	1
Teaching and other activities	**Year**	**ECTs**
Molecular Imaging for clinical physicist	2019	0,1
Supervising trainees	2014-2019	10
Reviewing articles for journals	2013-2019	1
Departmental research meetings	2013-2019	1
Departmental journal clubs	2014-2018	1
	Total	35,45

Orals and posters

SPECT imaging of pro-inflammatory macrophages using radiolabeled somatostatin analog (oral), MoMaDc meeting, 2019

Profiles of monocyte and macrophage subsets during the course of osteoarthritis in the destabilization of the medial meniscus mouse model (oral), Molecular Medicine Day, 2019

Analysis of peripheral blood monocyte and synovial macrophage subsets during osteoarthritis progression in the destabilization of the medial meniscus mouse model, poster, OARSI, 2019

^{111}In/^{177}Lu-DOTA-[Tyr^3]-albutate-1, a novel long circulating radiotracer for the somatostatin receptor subtype 2 (oral), EANM, 2018

Challenges of low count in vivo imaging (poster), EANM, 2017

11

Somatostatin receptor type 2 as a marker for pro-inflammatory macrophages: monitoring osteoarthritis (poster), Imaging research on the move, 2017

Somatostatin receptor type 2 as a marker for pro-inflammatory macrophages (poster), EMIM, 2017

Macrophage phenotypes are associated with processes of osteoarthritis in the collagenase induced osteoarthritis (CIOA) and destabilization of the medial meniscus (DMM) mouse models (poster), OARSI, 2017

Somatostatin receptor type 2 as a marker for pro-inflammatory macrophages (oral), MI Labs user meeting, 2017

Imaging joint inflammation with ^{111}In-Octreoscan (poster), EANM, 2016

Imaging joint inflammation with ^{111}In-Octreoscan (poster), EMIM, 2016

Macrophage imaging: can we show both sides of the medal? (oral), Research meeting Orthopaedics Department, 2016

Imaging joint inflammation with ^{111}In-Octreoscan (oral), MI Labs User Meeting, 2015

Macrophage imaging: can we show both sides of the medal? (oral), NKRV, 2015

Imaging somatostatin receptor expression on macrophages in osteoarthritis models (poster), EANM, 2015

Macrophage imaging: Can we show both sides of the medal? (oral), Departmental research meeting, 2013

List of Publications

Sandra van Tiel, Thea Maina, Berthold Nock, Mark Konijnenberg, Erik de Blois, Yann Seimbille, Monique Bernsen, Marion de Jong [^{111}In]In/[^{177}Lu]Lu-DOTA-[Tyr^3]-albutate-1, a novel long-circulating radiotracer targeting the somatostatin receptor subtype 2. *Under revision, Pharmaceuticals*

Sandra T. van Tiel[#], Lizette Utomo[#], Jan de Swart, Erik de Blois, Marion de Jong, Yvonne M. Bastiaansen-Jenniskens, Monique R. Bernsen. Evaluation of a radiolabeled somatostatin analog for SPECT imaging of pro-inflammatory macrophages. *Manuscript accepted by Biomedical research and reviews*

L. Utomo1, N. Fahy1, N. Kops1, **S.T. van Tiel**, J.H. Waarsing, J.A.N. Verhaar, P.J.M.8 Leenen, G.J.V.M. van Osch, Y.M. Bastiaansen-Jenniskens. Macrophage phenotypes and monocyte subsets after destabilization of the medical meniscus in mice. *Manuscript submitted to Journal of Orthopaedic research*

Ilya Skachkov, Ying Luan, **Sandra T. van Tiel**, Antonius F. W. van der Steen, Nico de Jong, Monique R. Bernsen, Klazina Kooiman. SPIO labeling of endothelial cells using ultrasound and targeted microbubbles at low mechanical index. *PLoS One. 2018 Sep 20;13(9):e0204354*

Ingrid L. Bakker, **Sandra van Tiel**, Joost Haeck, Gabriela N. Doeswijk, Erik de Blois, Marcel Segbers, Theodosia Maina, Berthold A. Nock, Marion de Jong, and Simone U. Dalm. In Vivo Stabilized SB3, an Attractive GRPR Antagonist, for Pre- and Intra-Operative Imaging for Prostate Cancer. *Mol Imaging Biol. 2018 Mar 19*

Bernsen MR, Guenoun J, **van Tiel ST**, Krestin GP. Nanoparticles and clinically applicable cell tracking. *Br J Radiol. 2015 Oct; 88(1054):20150375*

Duinhouwer LE, van Rossum BJ, **van Tiel ST**, van der Werf RM, Doeswijk GN, Haeck JC, Rombouts EW, Ter Borg MN, Kotek G, Braakman E, Cornelissen JJ, Bernsen MR. Magnetic Resonance Detection of CD34+ Cells from Umbilical Cord Blood Using a ^{19}F Label. *PLoS One. 2015 Sep 22;10(9): e0138572*

11

Joost Haeck, Karin Bol, Sander Bison, **Sandra van Tiel**, Stuart Koelewijn, Marion de Jong, Jifke Veenland and Monique Bernsen. Optimized time-resolved imaging of contrast kinetics (TRICKS) in dynamic contrast-enhanced MRI after peptide receptor radionuclide therapy in small animal tumor models. *Contrast Media Mol Imaging. 2015 May 21*

Ten Hagen TL, Seynhaeve AL, de Wiel-Ambagtsheer Ga, de Bruijn EA, **van Tiel ST**, Ruegg C, Meyring M, Grell M, Goodman SL, Eggermont AM. The αVβ3/αVβ5 integrin inhibitor cilengitide augments tumor response to melphalan isolated limb perfusion in a sarcoma model. *Int J Cancer. 2013 Jun 1;132(11):2694-704*

Kotek G, **van Tiel ST**, Wielopolski PA, Houston GC, Krestin GP, Bernsen MR. Cell quantification: evolution of compartmentalization and distribution of iron-oxide particles and labeled cells. *Contrast Media Mol Imaging. 2012 Mar-Apr;7(2):195-203*

Alic L, Haeck JC, Bol K, Klein S, **van Tiel ST**, Wielopolski PA, de Jong M, Niessen WJ, Bernsen M, Veenland JF. Facilitating tumor functional assessment by spatially relating 3D tumor histology and in vivo MRI: image registration approach. *PLoS One. 2011; 6(8):e22835*

van Tiel ST, Wielopolski PA, Houston GC, Krestin GP, Bernsen MR. Variations in labeling protocol influence incorporation, distribution and retention of iron oxide nanoparticles into human umbilical vein endothelial cells. *Contrast Media Mol Imaging. 2010 Sep-Oct;5(5):247-57.*

van Buul GM, Farrell E, Kops N, **van Tiel ST**, Bos PK, Weinans H, Krestin GP, van Osch GJ, Bernsen MR. Ferumoxides-protamine sulfate is more effective than ferucarbotran for cell labeling: implications for clinically applicable cell tracking using MRI. *Contrast Media Mol Imaging. 2009 Sep; 4(5):230-6.*

Bernsen MR, Moelker AD, Wielopolski PA, **van Tiel ST**, Krestin GP. Labelling of mammalian cells for visualisation by MRI. *Eur Radiol. 2009 Aug 12.*

Farrell E, Wielopolski P, Pavljasevic P, **van Tiel S**, Jahr H, Verhaar J, Weinans H, Krestin G, O'Brien FJ, van Osch G, Bernsen M. Effects of iron oxide incorporation

for long term cell tracking on MSC differentiation in vitro and in vivo. *Biochem Biophys Res Commun. 2008 May 16;369(4):1076-81*

Seynhaeve AL, Hoving S, Schipper D, Vermeulen CE, de Wiel-Ambagtsheer G, **van Tiel ST**, Eggermont AM, Ten Hagen TL. Tumor necrosis factor alpha mediates homogeneous distribution of liposomes in murine melanoma that contributes to a better tumor response. *Cancer Res. 2007 Oct 1;67(19):9455-62.*

Brunstein F, Rens J, **van Tiel ST**, Eggermont AM, ten Hagen TL. Histamine, a vasoactive agent with vascular disrupting potential, improves tumour response by enhancing local drug delivery. *Br J Cancer. 2006 Dec 18;95(12):1663-9*

Brunstein F, Eggermont AM, de Wiel-Ambagtsheer G, **van Tiel ST**, Rens J, ten Hagen TL. Synergistic antitumor effects of histamine plus melphalan in isolated hepatic perfusion for liver metastases. *Ann Surg Oncol. 2007 Feb;14(2):795-801*

Hoving S, Seynhaeve AL, **van Tiel ST**, aan de Wiel-Ambagtsheer G, de Bruijn EA, Eggermont AM, ten Hagen TL. Early destruction of tumor vasculature in tumor necrosis factor-alpha-based isolated limb perfusion is responsible for tumor response. *Anticancer Drugs. 2006 Sep;17(8):949-59.*

Brunstein F, Santos ID, Ferreira LM, **van Tiel ST**, Eggermont AM, Ten Hagen TL. Histamine combined with melphalan in isolated limb perfusion for the treatment of locally advanced soft tissue sarcomas: preclinical studies in rats. *Acta Cir Bras. 2005 Jul-Aug;20(4):275-9*

Hoving S, Seynhaeve AL, **van Tiel ST**, Eggermont AM, ten Hagen TL. Addition of low-dose tumor necrosis factor-alpha to systemic treatment with STEALTH liposomal doxorubicin (Doxil) improved anti-tumor activity in osteosarcoma-bearing rats. *Anticancer Drugs. 2005 Jul;16(6):667-74.*

Hoving S, Brunstein F, Aan de Wiel-Ambagtsheer G, **van Tiel ST**, de Boeck G, de Bruijn EA, Eggermont AM, Ten Hagen TL. Synergistic antitumor response of interleukin 2 with melphalan in isolated limb perfusion in soft tissue sarcoma-bearing rats. *Cancer Res. 2005 May 15; 65(10):4300-8.*

11

Hoving S, **van Tiel ST**, Eggermont AM, ten Hagen TL. Effect of low-dose tumor necrosis factor-alpha in combination with STEALTH liposomal cisplatin (SPI-077) on soft-tissue- and osteosarcoma-bearing rats. *Anticancer Res. 2005 Mar-Apr;25(2A):743-50.*

van Etten B, Eggermont AM, **van Tiel ST**, Ambagtsheer G, de Wilt JH, ten Hagen TL. Gene therapy in in vivo isolated perfusion models. *Curr Gene Ther. 2005 Apr;5(2):195-202.*

Brunstein F, Hoving S, Seynhaeve AL, **van Tiel ST**, Guetens G, de Bruijn EA, Eggermont AM, ten Hagen TL. Synergistic antitumor activity of histamine plus melphalan in isolated limb perfusion: preclinical studies. *J Natl Cancer Inst. 2004 Nov 3;96(21):1603-10.*

Preda A, Wielopolski PA, Ten Hagen TL, van Vliet M, Veenland JF, Ambagtsheer G, **van Tiel ST**, Vogel MW, Eggermont AM, Krestin GP, van Dijke CF. Dynamic contrast-enhanced MRI using macromolecular contrast media for monitoring the response to isolated limb perfusion in experimental soft-tissue sarcomas. *MAGMA. 2004 Dec;17(3-6):296-302*

van Etten B, Eggermont AM, Ambagtsheer G, **van Tiel ST**, ten Hagen TL. Impaired neutralising antibody formation and high transduction efficacy after isolated hepatic perfusion with adenoviral vectors. *Br J Cancer. 2004 Oct 18;91(8):1610-3.*

Van Etten B, **Van Tiel ST**, Ambagtsheer G, Eggermont AM, Ten Hagen TL. Isolated limb perfusion based anti-p21ras gene therapy in a rat rhabdomyosarcoma. *Anticancer Res. 2004 Jul-Aug;24(4):2295-301.*

ten Hagen TL, Hoving S, Ambagtsheer G, **van Tiel ST**, Eggermont AM. Lack of efficacy of Doxil in TNF-alpha-based isolated limb perfusion in sarcoma-bearing rats. *Br J Cancer. 2004 May 4;90(9):1830-2.*

Brouckaert P, Takahashi N, **van Tiel ST**, Hostens J, Eggermont AM, Seynhaeve AL, Fiers W, ten Hagen TL. Tumor necrosis factor-alpha augmented tumor response in B16BL6 melanoma-bearing mice treated with stealth liposomal doxorubicin (Doxil) correlates with altered Doxil pharmacokinetics. *Int J Cancer. 2004 Apr 10;109(3):442-8.*

van Etten B, de Vries MR, van IJken MG, Lans TE, Guetens G, Ambagtsheer G, **van Tiel ST**, de Boeck G, de Bruijn EA, Eggermont AM, ten Hagen TL. Degree of tumour vascularity correlates with drug accumulation and tumour response upon TNF-alpha-based isolated hepatic perfusion. *Br J Cancer. 2003 Jan 27;88(2):314-9.*

Lans TE, ten Hagen TL, van Horssen R, Wu PC, **van Tiel ST**, Libutti SK, Alexander HR, Eggermont AM. Improved antitumor response to isolated limb perfusion with tumor necrosis factor after up regulation of endothelial monocyte-activating polypeptide II in soft tissue sarcoma. *Ann Surg Oncol. 2002 Oct;9(8):812-9.*

Seynhaeve AL, de Wilt JH, **van Tiel ST**, Eggermont AM, ten Hagen TL. Isolated limb perfusion with actinomycin D and TNF-alpha results in improved tumour response in soft-tissue sarcoma-bearing rats but is accompanied by severe local toxicity. *Br J Cancer. 2002 Apr 8;86(7):1174-9.*

ten Hagen TL, Seynhaeve AL, **van Tiel ST**, Ruiter DJ, Eggermont AM. Pegylated liposomal tumor necrosis factor-alpha results in reduced toxicity and synergistic antitumor activity after systemic administration in combination with liposomal doxorubicin (Doxil) in soft tissue sarcoma-bearing rats. *Int J Cancer. 2002 Jan 1;97(1):115-20.*

de Wilt JH, Bout A, Eggermont AM, **van Tiel ST**, de Vries MW, ten Hagen TL, de Roos WK, Valerio D, van der Kaaden ME. Adenovirus-mediated interleukin 3 beta gene transfer by isolated limb perfusion inhibits growth of limb sarcoma in rats. *Hum Gene Ther. 2001 Mar 20;12(5):489-502.*

11

de Wilt JH, Manusama ER, van Etten B, **van Tiel ST**, Jorna AS, Seynhaeve AL, ten Hagen TL, Eggermont AM. Nitric oxide synthase inhibition results in synergistic anti-tumour activity with melphalan and tumour necrosis factor alpha-based isolated limb perfusions. *Br J Cancer. 2000 Nov;83(9):1176-82.*

Ten Hagen TL, Van Der Veen AH, Nooijen PT, **Van Tiel ST**, Seynhaeve AL, Eggermont AM. Low-dose tumor necrosis factor-alpha augments antitumor activity of stealth liposomal doxorubicin (DOXIL) in soft tissue sarcoma-bearing rats. *Int J Cancer. 2000 Sep 15;87(6):829-37.*

van IJken MG, van Etten B, de Wilt JH, **van Tiel ST**, ten Hagen TL, Eggermont AM. Tumor necrosis factor-alpha augments tumor effects in isolated hepatic perfusion with melphalan in a rat sarcoma model. *J Immunother. 2000 Jul-Aug;23(4):449-55.*

de Wilt JH, ten Hagen TL, de Boeck G, **van Tiel ST**, de Bruijn EA, Eggermont AM. Tumour necrosis factor alpha increases melphalan concentration in tumour tissue after isolated limb perfusion. *Br J Cancer. 2000 Mar;82(5):1000-3.*

van der Veen AH, de Wilt JH, Eggermont AM, **van Tiel ST**, Seynhaeve AL, ten Hagen TL. TNF-alpha augments intratumoural concentrations of doxorubicin in TNF-alpha-based isolated limb perfusion in rat sarcoma models and enhances anti-tumour effects. *Br J Cancer. 2000 Feb;82(4):973-80.*

de Wilt JH, Manusama ER, **van Tiel ST**, van IJken MG, ten Hagen TL, Eggermont AM. Prerequisites for effective isolated limb perfusion using tumour necrosis factor alpha and melphalan in rats. *Br J Cancer. 1999 Apr;80(1-2):161-6.*

12

Curriculum Vitae

Curriculum Vitae

Sandra Theresia van Tiel was born on October 10th 1971 in Rotterdam, The Netherlands. After finishing her secondary education at the Christelijke Scholengemeenschap Henegouwerplein in Rotterdam, she continued with her study Life Sciences at Hoger Laboratorium Onderwijs in Delft. Her internship was at the department of Medical Pharmacology of the University of Leiden. In 1996 she started working as a research technician at the Department of Surgical Oncology of the Erasmus MC under supervision of Dr. Timo ten Hagen and Prof. Dr. Lex Eggermont. In 2005 she started to work at the Department of Radiology under supervision of Dr. Monique Bernsen. Under supervision of Prof. Dr. Marion de Jong, of the Radiology & Nuclear Medicine Department, she started her PhD work in 2013, resulting in her thesis entitled: "Cellular imaging in regenerative medicine, cancer and osteoarthritis". Her studies focused on labelling cells involved in disease, with the aim to non-invasively detect cells for staging of disease and interference in disease development. Currently she is employed at the AMIE Core facility as Application Specialist for nuclear imaging and MRI.

Sandra married Mark van Ramshorst in 2008 and in that same year they got their son Steyn.